Integral Field Spectroscopy Observations of SN 1987A

Karina Edna Herum Kjær

München 2007

Integral Field Spectroscopy Observations of SN 1987A

DISSERTATION

der Fakultät für Physik der Ludwig-Maximilians-Universität München
zur Erlangung des Grades
Doktor der Naturwissenschaften
Dr. rer. nat.

vorgelegt von

Karina Edna Herum Kjær

aus
Ballerup, Dänemark

München, Oktober 2007

Abstract

This thesis is an observational study of the spectacular supernova 1987A in the near infrared (1-2.5 μm) in the Large Magellanic Cloud. The two epochs of data presented are from 17 and 18 years after explosion and we thus observe the supernova shock interacting with the pre-explosion circumstellar ring. The observations were done with an integral field spectrograph (SINFONI) mounted on the Very Large Telescope (VLT). These observations are the first of their kind for SN 1987A and they allowed me to establish the kinematics for the ring and ejecta separately.

With the ring kinematics I was able to find 'nodal points', where the ring intersects the plane of the sky, and from that I deduced that the ring is not only tilted with respect to the plane of the sky, but also has a rotation in the plane of the sky of 9°. This has never been done before for SN 1987A (or any other supernova) and the result confirms what had been suspected from imaging and modelling of the nebula structure around SN 1987A (Sugerman et al. 2005).

From the kinematics I derived an expansion velocity of the shocked gas component radially outward in the ring. I identified a vacant section of the circumstellar ring (in HST images at position angle $\sim 307°$) with a larger expansion velocity of the shocked cooling gas, consistent with the vacant region having a lower density than the rest of the ring.

The kinematics reveal that the ejecta's elongated emission structure is bipolar in its velocity, in that the North part is blue shifted and the South part red shifted. I derived upper and lower bounds for the inclination angle of the ejecta and find it not to be perpendicular to the ring as was commonly expected. This challenges the current believes about the symmetry axis of SN 1987A and it cannot be explained by any of the existing models for SN 1987A. I propose 3 possible scenarios: (1) The observed emission originates from a very thick disk situated in the ring. (2) The explosion caused the SN outflow to be not along the rotation axis of the progenitor. (3) The progenitor rotation axis was not aligned with the axis of the 3 rings.

With these data I have found new observational clues to the enigmatic SN 1987A, that will challenge scientists in years to come. SN 1987A has truly proven, that even after 18 years it is still exciting.

Zusammenfassung

Diese Dissertation beinhaltet eine Studie der spektakulären Supernova 1987A in der Großen Magellanschen Wolke, auf der Grundlage von Beobachtungen im nahen infrarot (1-2.5 μm). Ich präsentiere Daten aus zwei Epochen, 17 und 18 Jahre nach der Supernovaexplosion. Dies bedeutet, dass wir den Supernovaschock mit dem zirkumstellaren Ring wechselwirken sehen. Der Ring entstand schon vor der Explosion. Die Beobachtungen wurden mit einem Flächen-Spektrographen (SINFONI) am Very Large Telescope (VLT) gemacht. Sie sind die ersten ihrer Art von SN 1987A, und aus ihnen konnte ich die Kinematik des Rings und des Supernovamaterials zum ersten Mal getrennt voneinander ableiten.

Mit der Ringkinematik war es mir möglich die Knotenlinie zu finden, an denen der Ring die Himmelsebene schneidet. Daraus folgerte ich, dass der Ring nicht nur gegenüber der Himmelsebene gekippt, sondern auch mit einem Winkel von 9° in der Himmelsebene gedreht ist. Diese Analyse wurde bisher noch nicht auf SN 1987A (oder andere Supernovae) angewendet. Die Ergebnisse bestätigen die Vermutungen aus Bildanalysen und der Modellierung der Nebelstruktur von SN 1987A (Sugerman et al. 2005).

Aus der Kinematik leitete ich die Expansionsgeschwindigkeit der geschockten Gaskomponente ab, die sich radial im Ring nach aussen ausdehnt. Ich identifizierte einen freien Abschnitt im zirkumstellaren Ring (in HST Bildern, Positionswinkel ~307°) mit einer höheren Expansionsgeschwindigkeit des geschockten abkühlenden Gases. Dies stimmt damit überein, dass die freie Region eine niedrigere Materiedichte aufweist, als der Rest des Rings.

Die Kinematik zeigt, dass die gestreckte Emissionsstruktur des Supernovaauswürfes in ihrer Geschwindigkeit bipolar ist. Der nördliche Teil ist blauverschoben, der südliche Teil ist rotverschoben. Ich leitete obere und untere Grenzen für den Inklinationswinkel der Auswürfe ab, und entgegengesetzt der allgemeinen Erwartungen ist dieser nicht rechtwinklig zum Ring. Dies stellt die gängigen Vorstellungen über die Symmetrieachse von SN 1987A in Frage, und es kann auch nicht durch existierende Modelle von SN 1987A erklärt werden. Ich schlage drei mögliche Szenarien vor: (1) Die beobachtete Emission stammt von einer sehr dicken Scheibe, die sich im Ring befindet. (2) Die Explosion verursachte eine Abweichung der Auswurfrichtung von der Rotationsachse des Vorläufers. (3) Die Rotationsachse des Vorläufers stimmt nicht mit der Achse der drei Ringe überein.

Mit diesen Daten habe ich neue Beobachtungshinweise für die rätselhafte SN 1987A gefunden, die Wissenschaftler in den kommenden Jahren herausfordern werden. SN 1987A hat in der Tat bewiesen, dass sie selbst nach 18 Jahren immer noch aufregend ist.

Contents

Chapter 1

Introduction

The unique supernova SN 1987A has been a bo-
nanza for astrophysicists (see Figure 1.1 for a Hub-
ble Space Telescope (HST) picture of SN 1987A
and its triple ring system). It provided several ob-
servational firsts, like the detection of neutrinos from
the core collapse, the observation of the progeni-
tor star on archival photographic plates, the signa-
tures of a non-spherical explosion and mixing in
the ejecta, the direct observation of supernova nu-
cleosynthesis, including accurate masses of nickel
and titanium, observation of the formation of dust
in the supernova, as well as the detection of cir-
cumstellar and interstellar material. Now, after 20
years, it continues to be an extremely exciting ob-
ject as we are able to observe the supernova shock
interacting with the circumstellar ring in real time,
and we are able to resolve the expanding debris for
the first time.

Figure 1.1: SN 1987A with its triple rings
in the visual. North is up and East is to
the left as on all images in this thesis.

With its location in the Large Magellanic Cloud (LMC, a dwarf companion galaxy to our own
Milky Way) SN 1987A is the most spectacular stellar object outside our own galaxy. It is *the*
extra-solar object for which we have the most detailed information, but also *the* object where
we have the largest amount of mysterious unexplained things happening (i.e. the mystery spot,
the asymmetries, missing remnant etc.). This contrast arises because with the large amount of
information we can no longer assume the ideal simple (e.g. spherical) case, and as the detailed
knowledge grows so does the complexity of physics we observe.

I will in this chapter[1] give a background of the observational history, in order to understand
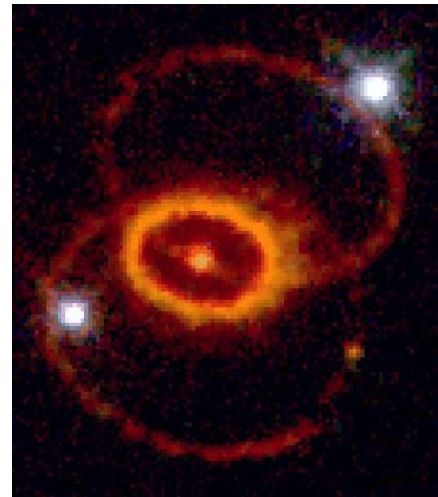the place this work takes as the next step towards an understanding of SN 1987A.

---

[1]Parts of the next section were published in our paper Fransson et al. (2007).

1.1 History of SN 1987A

When the first signs of Supernova 1987A, the first supernova of the year 1987, were noticed early on 24 February 1987, it was clear that this would be an unusual event. It was discovered by naked eye and on a panoramic photographic plate taken with a 10-inch astrograph on Las Campanas in Chile by Oscar Duhalde and Ian Shelton, respectively. Even before this new supernova was observed, SN 1987A placed itself in history as being the first object, besides the Sun, from which neutrinos have been received.

Neutrino Burst

A few hours earlier, still on 23 February, three large underground proton-decay detectors registered the passage of high-energy neutrinos. "Kamiokande II" is a neutrino telescope whose heart is a huge cylindrical tub, 52 feet in diameter and 53 feet high, containing about 3000 metric tons of water; it is located in the Kamioka mine in Japan, 3,300 feet underground. On February 23, around 7:36 am Greenwich time, the Kamiokande II recorded the arrival of 8 neutrinos within an interval of 2 seconds, followed by 3 more neutrinos 9 to 13 seconds later. Simultaneously, the same event was revealed by the IMB detector (located in the Morton-Thiokol salt mine near Faiport, Ohio), which counted 8 neutrinos within about 6 seconds. A third neutrino telescope (the "Baksan" telescope, located in the North Caucasus Mountains of Russia, under Mount Andyrchi) also recorded[2] the arrival of 5 neutrinos within 5 seconds from each other. Unlike the optical detections the localisation of the source was not so easy for the total of 24 neutrinos detected within about 13 seconds. Since SN 1987A exploded in the Large Magellanic Cloud (LMC), the detectors, all located on the northern hemisphere, measured the neutrinos after passage through the Earth. In recognition for this first detection of neutrinos from a celestial object other than the Sun Masatoshi Koshiba was awarded the Nobel Prize of 2002 (shared with Riccardo Giacconi for X-ray astronomy and Raymond Davis Jr. for solar neutrinos).

The most important implication of the neutrinos was that it confirmed the hydrodynamic core collapse, releasing about $3\mathrm{x}10^{53}$ ergs of gravitational energy, mainly in neutrinos of all kinds (due to the process: $e^- + p \rightarrow n + \nu$). This confirmed the predictions by Colgate, Arnett and others from the 1960s. Among many other results the few neutrinos showed that the electron-neutrino mass has to be rather small ($m_{\nu_e} \leq 20$ eV, superseded in the meantime by direct experiments) as no time-delay between different neutrino energies could be measured[3]. Also, the fact that there is no structure in the neutrino burst indicates that they came from the collapse to the neutron star, but no further collapse to a black hole occurred. At the same time these neutrinos

---

[2]The Baksan data has been largely ignored, perhaps because no methodology existed that could consistently account for the relatively large background rate in the Baksan detector. Loredo & Lamb (2002) demonstrate that the Baksan data are fully consistent with the KII and IMB data.

[3]A nonzero neutrino mass will cause particles of different energies to arrive at different times, even if they are emitted simultaneously. This dispersion stretches a neutrino burst out in time, with the higher energy neutrinos arriving before the more slowly moving, lower energy neutrinos. Since the neutrino energies did not decrease monotonically with arrival time only an upper limit of the mass could be derived. See Arnett et al. (1989) for a comprehensive review and Hillebrandt et al. (1987) for a simple clean calculation.

gave an unprecedented accuracy of better than a minute (the reason the accuracy is not better had to do with the time keeping at the neutrino detectors) for the time of explosion, which optical observations cannot provide as the photons emerge from the shock breakout on the surface of the exploding star, which can occur several hours later. The neutrinos were the direct signal from the collapse of the core of the progenitor star (Sanduleak -69º 202) to a neutron star. Although the actual neutrino count was only 24, it was a significant rise from the previously-observed background level. This was the first time neutrinos emitted from a supernova had been observed directly, and the observations were consistent with theoretical supernova models in which 99% of the energy of the collapse is radiated away in neutrinos. The observations are also consistent with the models' estimates of a total neutrino count of 10^{58} with a total energy of 10^{46} joules. It is believed that a small fraction of these neutrinos revived the stalled shock and powered the great explosion of the star. By heating and expanding the star and triggering a new flurry of nuclear reactions in its layered interior, the revived shock was responsible for the supernova's optical display. The effect was delayed by about two hours however: the shock had to traverse the entire star before any light leaked out. The neutrinos from the collapsing core easily out raced the shock. Passing through the rest of the star very close to the speed of light, they were the first signal to leave the supernova.

One highly significant result was obtained from the data regarding gravity. It appeared that the neutrinos and antineutrinos both took the same amount of time to arrive at earth, about 168,000 years. The difference in their arrival times was less than 13 seconds. This was the first empirical evidence that matter, antimatter, and photons all react similarly to gravity, which had been widely predicted by standard theories of gravity but had not been previously shown from direct empirical data.

Progenitor

Soon after the event was recorded, the progenitor star was identified as Sanduleak -69° 202, a blue supergiant (spectral type B3, Arnett et al. 1989) with a relatively modest mass. This was an unexpected identification, because at the time a blue supergiant was not considered a possibility for a supernova event in existing models of high mass stellar evolution. Instead everyone expected that the exploding star would be a red supergiant. For a time astronomers thought that Sk -69° 202 might be just a foreground star, and that a red supergiant lurked behind it. But the two-hour delay between neutrino detection and the optical outburst was consistent with the relatively small radius appropriate to a B star.
Current understanding is that the progenitor was a binary system, the stars of which merged about 20,000 years before the explosion, producing a blue supergiant (Podsiadlowski et al. 1990). Difficulties persist with this interpretation, however.

The Light Curve

The optical light curve of SN 1987A was rather different from other observed core-collapse supernovae, see Figure 1.2. Progenitor stars were normally assumed to be red supergiants with extended envelopes, which would produce long plateau phases in the light curve. This was not the case with SN 1987A, which started out as an extremely blue object only to turn into the
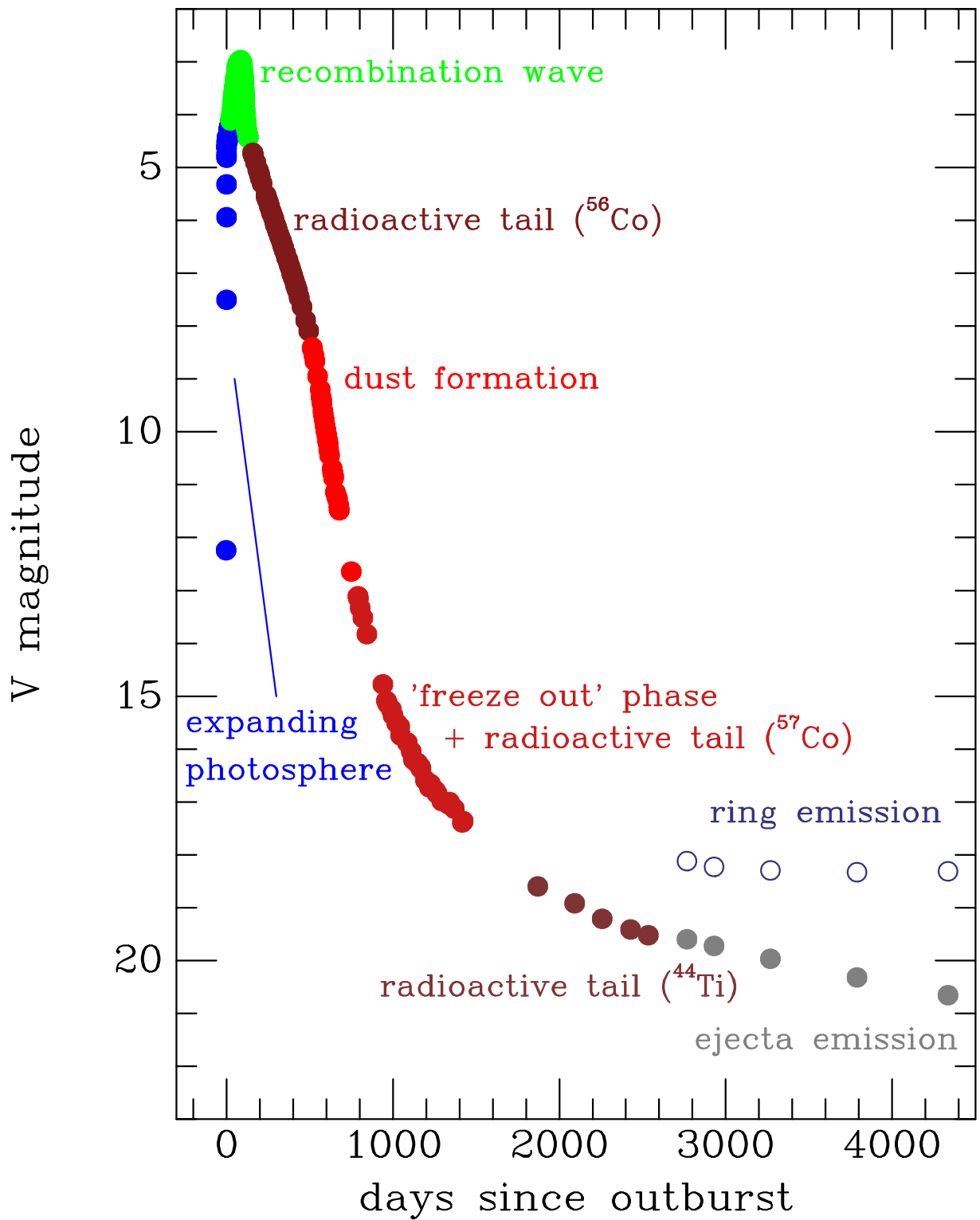
Figure 1.2: Light curve of SN 1987A over the first 12 years. The figure marks some of the most important events in the history of the supernova (from Leibundgut & Suntzeff 2003).

reddest supernova ever observed. The reason for this was that the supernova was discovered so early that the early cooling phase, when the supernova ejecta cool down from the shock passage, could be observed. But SN 1987A did not become as luminous as expected. The compact nature of the blue supergiant meant that the adiabatic cooling was stronger producing a fainter object than usual, as traced by Arnett et al. (1989).

About four weeks after explosion the supernova light curve was powered by the radioactive decay of freshly synthesised ^{56}Ni. Unlike for any supernova before, it was possible to construct a bolometric light curve of SN 1987A, which was extremely useful for the physical interpretation of the event. The absence of a significant plateau phase was understood in the context of the nature of the progenitor star and the extent to which the ejecta of the supernova were mixed. It turned out that helium was mixed into the hydrogen layer and hydrogen further down into the ejecta. This was also apparent from the early appearance of X-rays, originating from the ^{56}Co decay. Further confirmation for the strong mixing of the layers in SN 1987A came from the line shapes of the infrared lines. The old models of spherical explosions had to be revised and the density inhomogeneities in the stellar structure were recognised as responsible for turbulent mixing when the shock moved across such boundaries.

Still just 4 weeks old the supernova came with the next surprise, which was a 'mystery' spot close to the supernova. This spot was independently found by high-spatial resolution observations with speckle cameras at the Anglo-Australian Telescope (AAT, Marcher et al. 1987) and the Cerro Tololo Inter-American Observatory (CTIO, Karovska et al. 1987) 4m telescopes. The nature of this phenomenon remains unclear, but it was a clear indication of a broken symmetry. The asymmetry was also detected in polarisation observations of SN 1987A.

The spectroscopic evolution provided further evidence for asymmetries in the explosion. The Bochum event is a rapid change in the P-Cygni profile of the Hα line observed with the Bochum telescope on La Silla. It is the signature of a radioactive blob rising from the inner ejecta to the surface (beginning March 14th, see Hanuschik & Dachs 1987; Hanuschik 1988, for details). The picture emerging from the observations of the first several weeks was certainly more complex than what had been assumed of supernovae ever before.

Once SN 1987A entered the radioactive decline one could have expected that it would become less exciting. Far from it! International Ultraviolet Explorer (IUE) observations started to observe an increase in flux of several high-excitation lines[4], like NV, NIV], N III], CV, CIII], He II, mirrored by similar behaviour of [O III] and Hα in the optical at about 80 days after explosion. These lines could not possibly come from the fast moving ejecta and were quickly recognised as originating from material outside the supernova ionised by the soft X-rays from the shock breakout. From the high ionisation of these lines a temperature of $\sim 10^6$ K at the shock breakout could be inferred. The circumstellar material had to be from the progenitor star itself due to

---

[4]The nomenclature here is, that NIV is nitrogen ionised 4-1=3 times. Square brackets denotes forbidden transitions, half bracket is semi-forbidden. A forbidden line is emitted by atoms undergoing energy transitions not normally allowed by the selection rules of quantum mechanics. However, there is a non-zero probability of their spontaneous occurrence, should an atom or molecule be raised to an excited state. The transition probability is extremely low, and in normal (i.e. dense environments) atoms are collisionally de-excited before the forbidden line emission occur. In low-density gasses atomic collisions are unlikely, and forbidden line transitions occur and may even account for a significant percentage of the photons emitted.

the high nitrogen to carbon ratio, indicating CNO[5] processing (Fransson & Lundqvist 1989). This was, of course, emission from the inner circumstellar ring around SN 1987A, which was first imaged with the New Technology Telescope (NTT, Wampler & Richichi 1989). Later HST images provided the linear dimensions of the ring. In combination with the rise time for the narrow circumstellar lines, this provided a purely geometric distance to SN 1987A (Panagia et al. 1991). With the Large Magellanic Cloud being the first rung in the distance ladder to determine the Hubble constant, SN 1987A provided a very solid stepping stone.

Radioactivity and Dust

Just at about the same time as the appearance of the UV lines the supernova ejecta were presenting another surprise. Infrared spectroscopy about 100 days after explosion showed CO and SiO molecules at substantial masses (about 10^{-3} $M_\odot$). The presence of the molecules within the ejecta was difficult to explain. The formation of molecules required that they be protected from the UV and X-rays in the harsh environment of the ejecta. This also contrasted with the observations of the characteristic γ-rays at 847 keV and 1.238 MeV from the ^{56}Co decay, observed with KVANT on MIR. The characteristic decay lines could be observed for the first time ever in a supernova confirming the radioactive energy source. The X-rays are from Compton scattering of the γ-ray rays and their emission peaked after about 200 days and slowly declined thereafter as the number of ^{56}Co nuclei decayed away. The presence of molecules was a clear sign that there were regions in SN 1987A which could cool down significantly, while at the same time the radioactive material from the core had to be transported towards the surface to become observable.

Infrared wavelengths gained in importance as more and more radiation was emitted at longer wavelengths. The bolometric light curve very quickly started to become dominated by long-wavelength radiation and the inclusion of this spectral range became more and more important. ESO and CTIO collaborated for several years in providing this vital ingredient to measure the bolometric light curve. The decline of the light curve remained constant at the rate of the decay of ^{56}Co and allowed to measure the mass of ^{56}Ni (0.07 $M_\odot$) produced in the explosion. The Ni $\rightarrow$ Co$\rightarrow$ Fe decay chain could be observed directly in the changing line ratios of the near-infrared Co and Fe lines. The bolometric light curve was also the first indicator that something else was happening about 500 days after explosion. The light curve started to drop below the expected decline rate due to dust formation in the ejecta. At the same time the near-infrared [Fe II] lines dropped dramatically as the ejecta cooled below the temperature to excite these lines, a signature of the infrared catastrophe predicted by modellers (Spyromilio & Graham 1992).

Macroscopic dust grains which partially covered the ejecta and hence blocked some of the light had formed. The radiation was absorbed in the optical spectrum and shifted to the far infrared, where it was detected by the Kuiper airborne observatory (Larson et al. 1987). Line shifts towards shorter wavelengths of the infrared emission lines coming from the ejecta were a signature of the same phenomenon. Again, the explanation was that the distant part of the object is blocked by intervening dust (Lucy et al. 1991).

---

[5]The CNO cycle (for carbon-nitrogen-oxygen) is one of two fusion reactions by which stars convert hydrogen to helium, the other being the proton-proton chain. The CNO cycle is the dominant source of energy in heavier stars.

The light curve had one more unexpected deviation in store. After about 1200 days the decline started to slow down. First interpretations were that the slower decays of ^{57}Co were starting to dominate the light curve, but this would have required unreasonably high isotope ratios, which were inconsistent with the expected nucleosynthetic yields or the known abundances and it was also incompatible with the observed decline of the infrared Co lines compared to the Fe line, which allowed to deduce the amount of ^{57}Co. The explanation here was that the time scale for recombination and cooling in the supernova envelope became comparable to the expansion time scale, i.e. some of the 'stored' energy was finally released. This was termed 'freeze-out' as the ejecta no longer were in thermal equilibrium and detailed time-dependent calculations had to be performed. The light curve did flatten later because of the ^{57}Co (0.001 $M_\odot$) and by now is powered mostly by ^{44}Ti (10^{-4} $M_\odot$) (Fransson & Kozma 2002). The ^{56}Ni, ^{57}Co, and the ^{44}Ti radioactive isotopes all formed during the first seconds of the explosion and the masses of these together contribute some very strong constraints on the explosion models. Besides the determination of the radioactive isotopes also the masses of the most abundant elements formed in the progenitor star and in the explosion could be determined. This included such important elements as carbon, nitrogen, oxygen, manganese and silicon. For the first time one could determine reliable masses of these elements directly.

The Circumstellar Material

As mentioned, it was known from the ionised high-excitation lines that SN 1987A was surrounded by pre explosion material, expelled by the star during its evolution. Narrow-band imaging with the NTT about three years after the explosion revealed a circumstellar structure around SN 1987A, which resembled the triangular hat, which Napoleon would have worn. It was baptised 'Napoleon's hat' and the image provided the first opportunity for a 3-dimensional view of SN 1987A. This image together with the detection of extended narrow emission from the He I 1083 nm line and the IUE observations of the circumstellar gas was a first indication that there was more to come with this supernova. HST revealed first the inner ring and then later confirmed the outer rings (Fig. 1.1). The NTT was used to measure the density and other properties of the outer rings (Wampler et al. 1990). The HST images also showed the fading supernova ejecta in the middle. The ring on the other hand had been fading extremely slowly and hence after about ten years it started to outshine the ejecta. The circular ring is inclined by about 43º with the northern part closer to us. It is essentially stationary with an expansion velocity of about 10 kms^{-1} (Gröningsson et al. 2006).

The existence of the ring presents an unsolved puzzle of SN 1987A. It obviously is the remnant of the stellar mass loss history of the progenitor star. However, how did it become concentrated into a ring and is not distributed spherically? With the two outer rings there appears to be an hour-glass shaped structure enveloping the supernova itself, with the inner ring at its waist. Even though it is not clear how to construct such a ring, it is likely that the progenitor system of SN 1987A had to be a binary (e.g., Morris & Podsiadlowski 2007). What happened to the companion is unclear and no trace of it, -other than the rings, has been detected. Some theories surmise that the progenitor of SN 1987A was a merger, a star that had swallowed its companion.

Several light echoes, the integrated light from the peak phase reflected off interstellar sheets between the supernova and us, have been observed over the years around the supernova. They have been monitored with several telescopes and have been used to map the interstellar material in the LMC near the supernova.

The Crash

The first 10 years the supernova radiation was dominated by energy deposited in the interior by the decay of newly synthesised radioisotopes. Many wavelength observations yielded knowledge about dynamics and thermodynamics of the expanding debris. At around age of 9 years the supernova blast wave struck the inner circumstellar ring. Radio, infrared, optical and X-ray radiation changed to be dominated by the impact of the supernova debris with the circumstellar material. This transition marks the birth of a supernova remnant.

The prediction that the stationary ring would be reached by the supernova shock was made early on, but the exact date was debated. The radio flux of SN 1987A, -after an initial short emission of a few weeks, started to increase again after about 1200 days (Manchester et al. 2002). This brightening has continued since then and was the first signal of the interaction of the supernova shock with the circumstellar environment. Similarly, the X-ray flux started to increase, and has continued to increase almost exponentially (Park et al. 2006; Haberl et al. 2006). Finally, after 10 years a spot of optical emission appeared toward the North-East of the ring. And again this was a surprise: rather than having the shock reach a smooth ring more or less simultaneously, the ring appears to be more like spokes on a wheel with inward intrusions. Also, the expansion of the supernova shock may be not uniform and faster in some directions than others. The asymmetries in the explosion could be reflected in this interaction as well. Over the past few years the ring has continued to be lit up in various places and now resembles a pearl necklace (Fig. 1.3). The interaction is now observable at all wavelengths from the X-rays (Chandra and XMM), the optical and infrared (all major southern observatories VLT and Gemini, HST), as well as the far infrared (Spitzer) and radio (Australia Telescope Compact Array, -ATCA), and a rich data set is being assembled. We show in chapter 5 new infrared observations of the gas shocked by the ejecta ring interaction, with spectra from different positions around the ring.

The Ejecta

As already described in section 1.1 extensive early observations proved that the ejecta are aspherical. This is deduced from (i) the 'Bochum event', -basically radioactive blob rising from the inner ejecta to the surface, (ii) the spectropolarimetry, -which implied that the ejecta have a single well defined axis of symmetry, and (iii) the appearance of the mystery spot as secondary source off center from the bulk of the ejecta.
It is also known that the debris has a heterogeneous composition. The early emergence of gamma rays from SN 1987A showed that some of the newly synthesised ^{56}Co (and probably also clumps of oxygen and other elements) were mixed fairly far out into the supernova envelope by instabilities following the explosion (McCray 1993).
The ejecta was also observed in radio as an expanding annulus with a radial outward velocity of v_{rad}=3000 km s^{-1} (Manchester et al. 2002). This emission most likely comes from relativistic
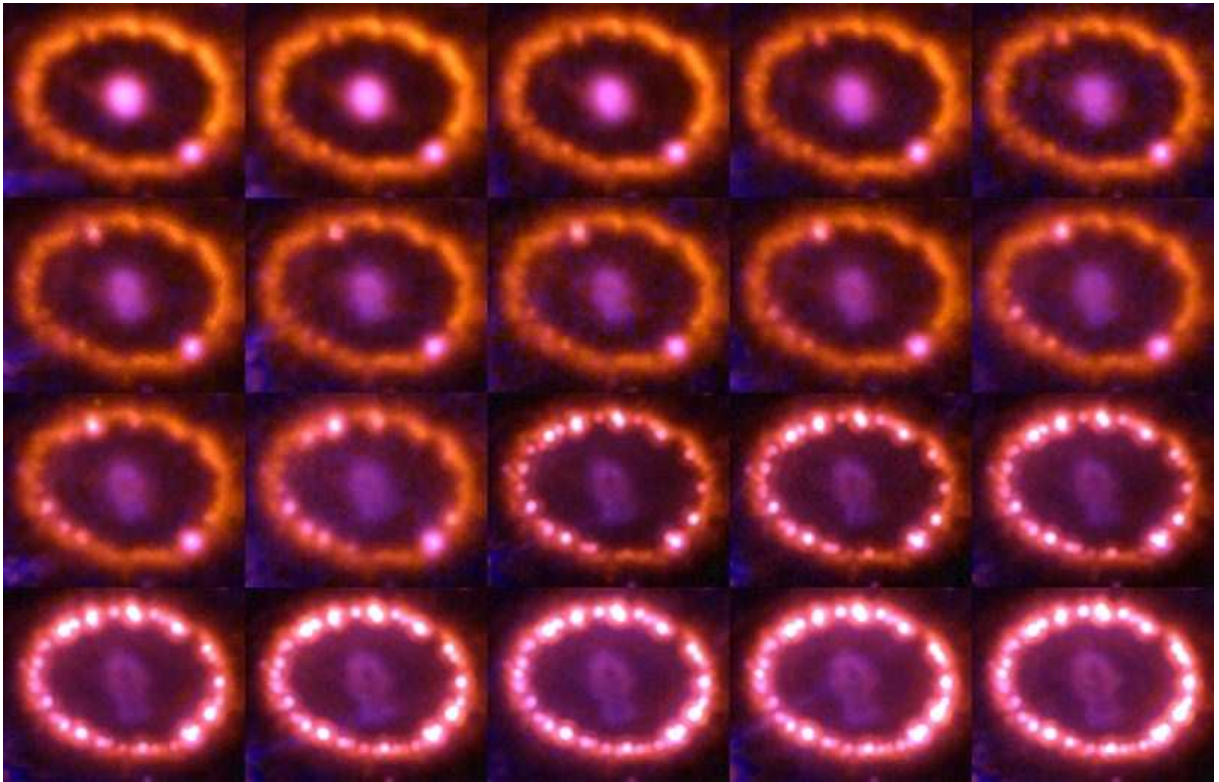
Figure 1.3: Hubble Space Telescope image of the inner ring from 1993 to 2005, showing the appearance of hot spots around the ring. North is up and East is to the left. From the SAINTS Team/Peter Callis/NASA.

electrons accelerated by shocks formed inside the inner ring where the supernova debris struck relatively low density circumstellar material.

1.2 The Supernova at Twenty

Now the supernova emission is dominated by the shock interaction, although we still detect faint emission from the ejecta. This section will provide an overview of the most recent observations of SN 1987A. Parts of this section has previously been published in Kjær et al. (2007a).

At optical/near-IR wavelengths we can now distinguish four emission sites in SN 1987A: (1) the ejecta in the centre with a typical velocity structure of 3000 km s^{-1}, (2) the unshocked fluorescing ring material with 10 km s^{-1}, (3) the shocked material in the ring, visible in the hot spots and with velocities of about 300-500 km s^{-1}, (4) the reverse shock moving back into the supernova ejecta with a velocity of up to 15000 km s^{-1}. Figure 1.4 shows a spectrum around the Hα line observed with the Ultraviolet and Visual Echelle Spectrograph (UVES on the VLT Gröningsson et al. 2006) in 2002. Three different components can clearly be distinguished in the spectrum: the narrow lines, the broader lines, and the very wide component from the reverse shock.

Coronal emission from the shocked circumstellar ring

Figure 1.4 also shows the detection of a coronal line (emission from a highly excited element), and Gröningsson et al. (2006) report on several such detections (e.g. [Fe XI],[Fe XIV]). A comparison of the evolution of the line fluxes for the coronal lines and the X-ray emission reveals an interesting correlation. The line fluxes of the coronal Fe lines increased exactly like the soft X-ray (0.5–2 keV) emission as measured by the Chandra satellite (Park et al. 2005), see Fig. 1.5. This, together with similar shock velocities required to produce the coronal lines, led Gröningsson et al. (2006) to argue that the coronal lines form in the same region as the soft X-rays. The coronal lines therefore offer a complementary view to the X-rays of the shock interaction. In this respect the high resolution spectrum of Chandra (Zhekov et al. 2005) is especially interesting, showing lines from, e.g., Fe XVII. Several of these lines are coming from highly ionised atoms, in particular [Fe X], [Fe XI], [Fe XIV], [Ne V] and [Ar V]. These arise in the collisionally ionised gas behind the shock propagating into the dense protrusions of the ring. Gröningsson et al. (2006) presented a detailed analysis of the coronal lines and derived the temperature required for their formation. The gas must be heated to about $2 \cdot 10^6$ K, corresponding to a shock velocity of ~ 350 km s^{-1}. The fact that also lines of low ionisation ions, like OI-III and Fe II, are seen shows that most of the emission is coming from radiative shocks. However, it cannot be excluded that some of the emission in the coronal lines of FeX–XIV arise from shocks which have not had time to cool yet.
In addition, the X-rays show evidence of shocked gas with a temperature of $\geq 10^8$ K, which has not had time to cool down enough to be seen in the optical (Zhekov et al. 2006).

The radio evolution is tracing the hard X-ray emission, because it is coming from the synchrotron radiation. The radio light curve is increasing, like the hard X-ray curve, reflecting the
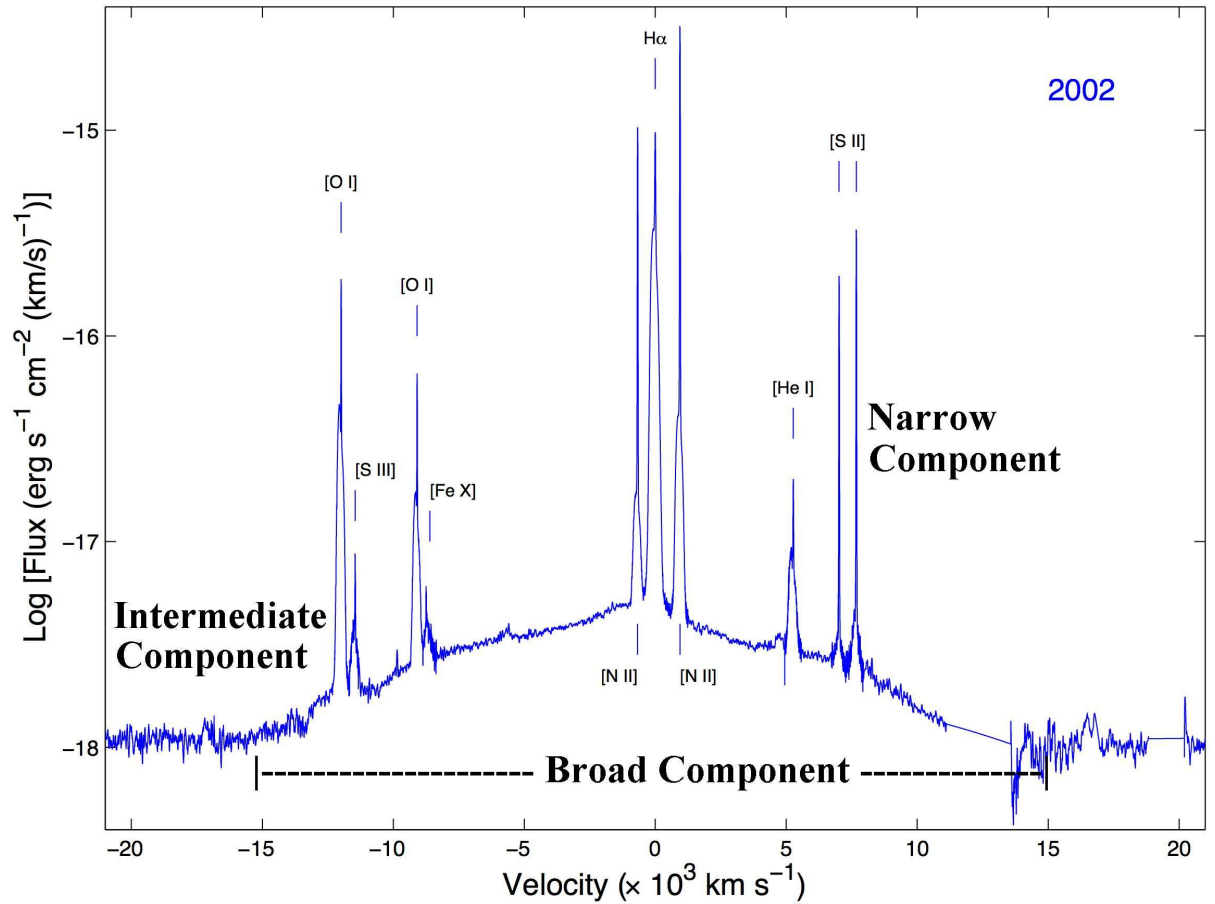
Figure 1.4: The spectral region around Hα for SN 1987A 5704 days after explosion as observed with UVES (Gröningsson et al. 2006). The velocity scale is centred on Hα. Note the very broad component originating in the reverse shock, extending to ∼ 15,000 km s^{-1}. Superimposed on this are the narrow (FWHM ∼ 10 km s^{-1}) and intermediate (FWHM ∼ 300 km s^{-1}) velocity components, coming from the unshocked and shocked ring material, respectively. In addition to the Hα line several other low and intermediate ionisation lines, as well as the coronal [Fe X], are visible.

Figure 1.5: Flux evolution of the coronal lines as measured in optical spectroscopy (left) and the flux increase of the X-ray emission from SN 1987A (Park et al. 2005). The fluxes have been normalised to the ones observed in October 2002 (see Gröningsson et al. 2006, for more details).
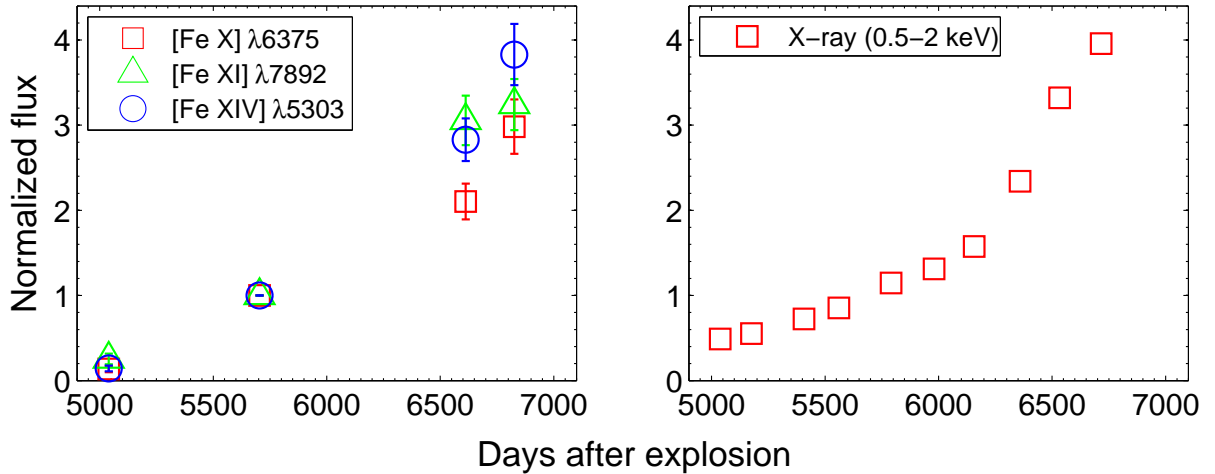
production of non-thermal electrons, and probably also cosmic rays, in the shock.

The soft X-rays are traced by the infrared (IR) emission. The infrared emission show a brightening of the lines from the cooling, shocked gas component (Kjær et al. 2007b), when compared to the older IR spectra. The optical and UV observations of this component corresponds neatly with the IR presented in this thesis.

In the mid infrared hot dust emission has been seen by Spitzer (an infrared space telescope), as well as by VISIR (VLT Imager and Spectrometer for mid Infrared an instrument on the Very Large Telescope (VLT)) and T-ReCS (Thermal Region Camera and Spectrograph) on Gemini observatory (Bouchet et al. 2006).

The reverse shock

The UVES spectra clearly show a broad Hα line extending to $\sim 15,000$ km s^{-1} (Fig. 1.4). This velocity component is called the reverse shock and is discussed in detail by Michael et al. (2002); Smith et al. (2005); Heng et al. (2006).

The expanding ejecta comprising mostly of neutral hydrogen, which has been adiabatically expanding and thus cooling, crosses the reverse shock at $\sim 12000 - 15000$ km s^{-1}. The excitation and subsequent radiative decay of the atoms result in the broad reverse shock emission. The excitation of Hα is uncertain, but at the reverse shock boundary fast atoms from the ejecta are being converted into slow ions at the reverse shock. In addition to impact excitation, atoms may also donate their electrons to ions in the shocked plasma (i.e. charge transfer), thereby producing a population of slow atoms. The broad velocity component is then caused by the ejecta overtaking the reverse shock and being slowed down there. The reverse shock region moves outwards at a low velocity (about 3000 km s^{-1}) because the shock is slowing down the outward movement. The reverse shock emission continues to increase, but it is possible that the neutral hydrogen atoms in the ejecta will be ionised by emission from the forward shock before

12

the reverse shock reaches it and the Hα emission from the reverse shock may stop (Smith et al. 2005; Heng et al. 2006; Heng 2007).

The ejecta and the remnant

The supernova ejecta themselves are now difficult to observe due to their faintness and the increasing brightness of the inner ring. The ejecta emission is now dominated by energy input from the radioactively excited core, i.e. ^{44}Ti (Fransson & Kozma 2002; Bouchet et al. 2004, 2006). The evolution of the shape and size of the ejecta of SN 1987A has been analysed by Jansen & Jakobsen (2001) based on HST images and spectra from day 1278 (3.5 years) to day 4336 ($\sim$ 12 years) since the explosion. They report the shape of the ejecta changing from spherical to elongated, as can be seen in Figure 1.3.

The compact remnant in the centre has so far remained elusive. The neutrinos indicate that such a compact object should exist, but it remains deeply embedded in the ejecta. The very low limits to both the optical (Graves et al. 2005) and X-ray luminosity (Park et al. 2006) may be explained by either gas or dust absorption. In this case, however, the radiation should emerge in some waveband, possibly the far-IR. Other possibilities to explain the apparent absence of a neutron star include a weak magnetic field, slow rotation[6] or that a black hole may have formed, possibly as a result of fall-back of material onto the new-born neutron star.

The Future

SN 1987A was full of surprises and it remains unique amongst the known supernovae. Not only was it the closest supernova for several centuries, it was also a very peculiar one coming from a blue supergiant progenitor, with a circumstellar environment unlike any other supernova known.
It is clear that with the kinematic information we will be able to further investigate the evolution of the supernova shock as it envelopes the circumstellar ring in the coming years.
SN 1987A represents a fascinating laboratory to study how a supernova interacts with its surrounding. The coming years will provide exciting times and SN 1987A will remain the focus of observations with many telescopes. The destruction of the inner ring will take many years and maybe it will hold a clue to its origin. The X-rays may also help illuminating any material outside the ionised ring from a possible red supergiant stage. The circumstellar ring of SN 1987A will be a bright source at all wavelengths for several years. We will continue to watch its evolution towards a supernova remnant.

1.3 Emission structure

After nearly two decades at least five emission mechanisms can be found in SN 1987A. The ejecta continue to glow as a result of the radioactive decay of long-lived nuclei (mostly ^{44}Ti), but they are fading continuously because of the expansion and the reduced opacity. The nearly

---

[6]The energy radiated away in the magnetic dipole model is $\dot{E} \propto B^2 \Omega^4$, where B is the magnitude of the surface magnetic field strength and Ω is the angular frequency.

stationary rings around SN 1987A are still fluorescing from the recombination of matter originally excited by the soft X-ray emission from the shock breakout at explosion of the supernova. The supernova shock reached the inner circumstellar ring about ten years ago and the forward shock is moving through the inner ring and leaves shocked material behind. This material is excited and accelerated. The reverse shock illuminates the fast-moving supernova ejecta as it catches up. And, finally light echoes in nearby interstellar matter can still be observed.

Figure 1.6 shows an illustration that summarises the different emission sites. The equatorial ring (red) is shown as a diffuse gas with inward protrusions, marked here as 'hot fingers' (white) as they are engaged by the forward shock wave (bright yellow). In between the forward shock wave and the reverse shock wave (dark yellow) the hot gas resides (yellow). In the interior the cool ejecta (blue) resides.

The different emission mechanisms are explained in detail in the following.

Ejecta Emission

The ejecta emission is now dominated by energy input from the radioactively excited core, i.e. ^{44}Ti (Fransson & Kozma 2002; Bouchet et al. 2004, 2006). The emission lines originating in or near the ejecta are excited by this emission, and will most probably outline the titanium clumps. It is becoming clear that the supernova ejecta is deviating strongly from a spherical distribution (Wang et al. 2002). We show in chapter 6 new observations of the ejecta, in which the ejecta are spatially and spectrally resolved for the first time revealing their kinematics.

The freely-streaming debris has a unique velocity for a given radial distance from the SN core, exactly analogous to Hubble flow in an expanding universe. At the reverse shock this freely-streaming material is decelerated by the shock, and from this radius and further away from the SN core the velocities are governed by the shock.

Shock Emission

As supernova 1987A's outer envelope expands into its surrounding circumstellar material a double shock structure forms (Chevalier 1982), consisting of a forward shock (the blast wave) that propagates into the circumstellar gas ($\sim 4000 - 5000$ km s^{-1}), and a reverse shock that propagates outwards still but at a slower pace ($\sim 3000 - 4000$ km s^{-1}), allowing the SN debris to overtake it (debris $\sim 12000 - 15000$ km s^{-1}). In between a contact discontinuity separates the shocked circumstellar material and the shocked debris. Pun et al. (2002) gives a very thorough description of a double-shock structure in SNR-SN 1987A, see Figure 1.7, which shows the schematics for just spot 1.

The shock is caused by the impact of the supernova blast wave with a dense inward protrusion of the ring (Michael et al. 2000). When the blast wave overtakes such an obstacle, slower shocks are transmitted into it. Since a range of densities are present in the ring, it is expected that the transmitted shocks have a range of velocities.

The **forward shock** is the forefront of the blast wave propagating with a velocity $\sim$ 4000-5000 km s^{-1}. When it hits an obstacle it will result in **transmitted shocks** in that obstacle, and the shock will be slowed down to $\sim$ 700 km s^{-1} or less depending on density and angle of incidence. It will also cause a **reflected shock** going backwards into the blast wave. This all happens at a position where the blast wave overtakes material in a frontal collision. The

EQUATORIAL RING

HOT FINGERS

FORWARD SHOCK WAVE

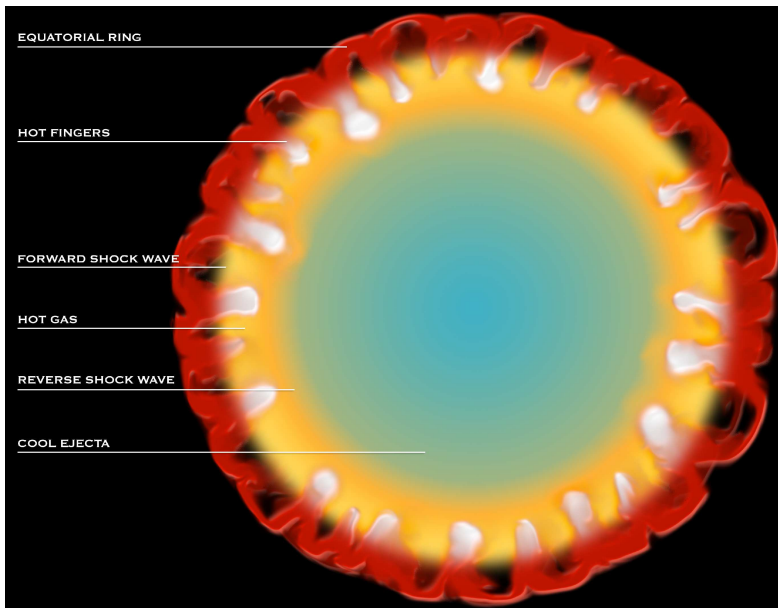HOT GAS

REVERSE SHOCK WAVE

COOL EJECTA

Figure 1.6: Illustration of the emission sites from Chandra PR pages.

spots on the ring of SN 1987A are thought to be long elongated protrusions and thus only a small fraction of the blast wave participates in this head on collision. The rest of the blast wave moves unhindered on. The blast wave that runs along the sides of the long protrusions also causes shocks. These are called **oblique shocks**.

The radio and the X-ray light curves tracked each other very well until about 1999 (Park et al. 2007), when the soft X-rays brightened much faster than the hard X-rays. This happened roughly at the time when the hot spots appeared in the optical, supporting the idea that the optical and the soft X-rays are dominated by the hot spots (together with the UV).

We ever only see the part of the shocked gas, that had time to cool down. Most of the soft X-ray emission comes from relatively fast (v ~ 500-700 km s^{-1}) shocks, while the optical emission comes from gas that has been compressed by relatively slow (v ~ 150-300 km s^{-1}) shocks. Only gas that has had time to cool by radiation will emit significant optical radiation. The difference in velocity can be attributed to different shocks engaging protrusion from different sides, and variations in density causing different transmitted shock velocities. What we observe will be an average velocity.

The larger the shock speed, the longer time it takes for the gas to cool. In the oblique shocks the velocities are much smaller, because the shock is not head on, but rather an instability caused by faster moving material on the surface of slower moving material (Kelvin Helmholz instability[7]). The material heated this way will have a short cooling time because the density is higher and the shock velocity was slower. The physics in this region is dominated by radiative transfer and predominately optical and UV photons are emitted (together with the soft X-rays).

The shocked gas trailing behind the shock front is very hot because the shock velocity was

---

[7]This phenomenon is more commonly seen as the ripples of the sand just below the water on the beach.

large. This means that this region is dominated by collisions and the cooling time is long. It is from this region that the infrared photons are thought to be emitted along side with the hard X-rays and radio. This shock component is called the intermediate component (IC) and shows line widths of ~ 200-300 km s^{-1}.

Since the protrusions are engaged from several sides the velocity we derive from the emission lines Doppler displacement will be a crude average of the different shocks convolved with the geometry along any given line of sight.

The **reverse shock** is clearly seen in the Lyα and Hα emission lines emitted by hydrogen atoms that cross the reverse shock. This emission is not produced by recombination but by neutral hydrogen atoms in the supernova debris, that are excited by collision with electrons and protons in the shocked gas. The observed flux of broad Lyα is a direct measure of the flux of hydrogen atoms crossing the reverse shock. The reverse shock is propagating outwards with a velocity of about 80% that of the forward shock wave (Heng et al. 2007).

The Stationary Ring

A few months after the explosion narrow optical and ultraviolet emission lines were detected from the system. The emission revealed many details for the system: First of all that the emission originated from an almost stationary gas (the emission lines were narrow). The elements in the gas showed large ionisation, and it must have been ionised by soft X-rays from the explosion. The gas deposited by the progenitor showed large amount of nitrogen, which put constrains on the evolutionary path of the progenitor. The light-curve rise time put the gas at a distance of a light year from the supernova, and last the fading of the narrow emission lines put the density of the gas at $3 \times 10^3 - 3 \times 10^4$ cm^{-3} (Lundqvist & Fransson 1996).

Today we still can see the narrow lines from the stationary ring, they are expected to rise in strength as they are re-ionised by the emission from the shock interaction.

1.4 This Thesis

Figure 1.7: Schematic representation of the double-shock structure of SN 1987A from Pun et al. (2002).

This thesis is an observational study of the spectacular supernova (SN) 1987A at infrared (IR) wavelengths (2-2.5 μm) in the Large Magellanic Cloud. Chapter 1 (current) aims to give a background on SN 1987A and explain the physics behind the IR emission we observe today. I present two epochs 17 and 18 years after explosion of data both observed with an integral field spectrograph operating in the IR (SINFONI) mounted on the Very Large Telescope (VLT, in Chile). This makes these the first IR observations to be published since Fassia et al. (2002) published spectra from the supernova at the age of 9 years.

The extended nature of the inner ring (and by now the ejecta) limits slit spectroscopy to individual regions of the ring. With an integral field unit, it is now possible to measure the ring and the supernova ejecta without losses, to reconstruct the ring emission in individual lines, and it allows for a clean separation of the ejecta from the ring.

These observations are the first of their kind for SN 1987A and I have with it established the kinematics for the ring and ejecta separately for the first time. The kinematics for the ejecta, presents another exciting event in the history of SN 1987A, in that the velocity distribution challenge the (until now) assumed symmetry axis of the supernova and its triple rings. This result

was not expected and none of the existing models of SN 1987A can account for it. I have with these observations found another puzzle for supernova researchers in years to come.

The first epoch from 2004 was observed as a part of the science verification run on SINFONI, and thus were the first data of this kind of SN 1987A. The second epoch was observed in 2005 after I was awarded time via a normal proposal process (Principal Investigator: K. Kjær, proposal id: 080.D-0588C). I planned the observations based on the Science verification, where I had established which setting of the instrument would be most beneficial for the scientific output. Integral field spectroscopy is also called 3D spectroscopy, since the data format is 3-dimensional (position on sky and wavelength) and best represented as a cube. While this data-format has been used for some years for galaxies, I had to develop new analysing techniques and considerations, because SN 1987A is an emission line object, where the lines originate from different physical processes. Chapter 2 lays out the observational technique behind the instrument, the instrument pipeline which constructs the data format, and the methodology I developed in order to interpret the data. Chapter 3 explains the data reduction and calibration of the two epochs, and Chapter 4 shows the spectra and line identification. In Chapter 5 I analyse the circumstellar ring in ways only possible with 3D spectroscopy. I have with our data been able to separate the ejecta emission of the supernova from the circumstellar ring, and I describe our findings in Chapter 6. I finally discuss and summarise our results in Chapter 7.

Parts of the background sections on SN 1987A have been published in Kjær et al. (2007a) "SN 1987A at the end of its second decade", proceedings to the Cefalu conference 2006 and in the ESO Messenger (Fransson et al. 2007). The parts of Chapter 3, 4, 5, and 6 that is about epoch 2004 has been published in Kjær et al. (2007b). The following chapters present work done by me, unless clearly stated otherwise, even though I often chose to use 'we' as the subject.

Chapter 2

SINFONI: Instrument, Pipeline, and Methodology

The work in this thesis is based on integral field spectroscopy observations. This is an exciting new technique in which spectra and images are obtained simultaneously. In this chapter I describe the instrument I used (SINFONI), the pipeline I used for the data reduction and a glossary for this kind of data. This Chapter also describes the considerations one should have when interpreting integral field spectroscopy data for an emission line object and the methodology I developed for the analysis.

2.1   Instrument

According to the user manual (Kissler-Patig & Szeifert 2005) SINFONI is a near-infrared (1.1-2.45 μm) integral field spectrograph fed by an adaptive optics module. The spectrograph operates with 4 gratings (J, H, K, H+K band) providing a spectral resolution around $\lambda/\Delta\lambda$ 2000, 3000, 4000 in J, H, K, respectively, and 1500 in H+K - each wavelength band fitting fully on the 2048 pixels of the Hawaii 2RG (2k $\times$ 2k) detector in the dispersion direction.

The technique behind the integral field spectroscopy is to split the *Field of View* (FOV) image into parts and obtain spectra from each of those parts simultaneously. At the moment there are two ways this is successfully being done; Either by splitting the image using fibers or by using mirrors.

SINFONI is based on image slicing using mirrors, essentially the FOV image is redirected using mirrors, one of which splits the image in the vertical direction. Figure 2.1 shows the basic concept of image slicing. The image-slicer consists of two sets of plane mirrors, one set of mirrors to slice the image, the other set of mirrors to rearrange the sliced image. The first set of mirrors, consists of a stack of 32 mirrors, which slice the image into 32 slitlets (the slices are often referred to as slitlets). These mirrors are positioned at a small angle with respect to each other, and thus they reflect different parts of the FOV image in slightly different directions. The second set of mirrors rearrange the 32 slitlets (the 32 now separated parts of the image) to form one long image, often referred to as 'a pseudo long-slit' image. The light in this long-slit is then fed into a long-slit spectrograph to disperse the light and obtain the spectra. During the data reduction

the two-dimensional spatial information together with the third, spectral information is used to create a data cube. The spatial resolution in y-direction is directly set by the height of the slitlets.

The pre-slit optics allows to chose the plate scale and thus the width of the slices. The choices are slit widths of 250mas (mas=10^{-3} arcseconds), 100mas and 25mas, leading to field of views on the sky of 8"x8", 3"x3", or 0.8"x0.8" respectively. Each one of the 32 slitlets is imaged onto 64 pixels on the detector. Thus one obtains 32x64 spectra of the imaged region on the sky. Figure 2.2 shows a raw science image from SINFONI. The 32 slitlets are imaged next to each other in the x direction and with a small offset in the dispersion direction (y-direction). The (many) bright lines are skylines, the small bright points are cosmic rays or bad/hot pixels, and the fuzzier blobs are from the circumstellar ring of SN 1987A. In this exposure Star 3 is not in the FOV, since a star, being a continuum source, would appear as a bright vertical line.

SINFONI can be used without adaptive optics (AO) guide stars, in which case the AO module just acts as relay optics and the spatial resolution is dictated by the natural seeing. The full power of the instrument is, of course, achieved when an adaptive optics guide star is available. For best correction, the star should be brighter than R=11 mag. However, the AO can work (and will provide moderate image quality improvement) with stars as faint as R=17 mag in the best seeing conditions. Ideally, the AO guide star should be as close as possible to the scientific target (if not the science target itself), and usually closer than 10". Depending on the atmospheric conditions (atmospheric coherence length) the AO guide star could be chosen as far as 30" for the AO system to still provide a mild improvement of the encircled energy.

The **Strehl ratio** is commonly used to assess the quality of seeing in the presence of atmospheric turbulence and assess the performance of any adaptive optical correction system. The definition of the Strehl ratio is the ratio of the observed peak intensity at the detection plane of a telescope or other imaging system from a point source compared to the theoretical maximum peak intensity of a perfect imaging system working at the diffraction limit[1]. The intensity distribution in the image plane of a point source is generally called the point spread function (PSF). Obviously, characterising the form of the point-spread function by a single number, as

---

[1]A beam of light of a finite size undergoes diffraction and spreads in diameter. This effect limits the minimum diameter d of spot of light to: $d = 1.22\lambda\frac{f}{a}$, where f is the focal length and a is the diameter of the beam of light.
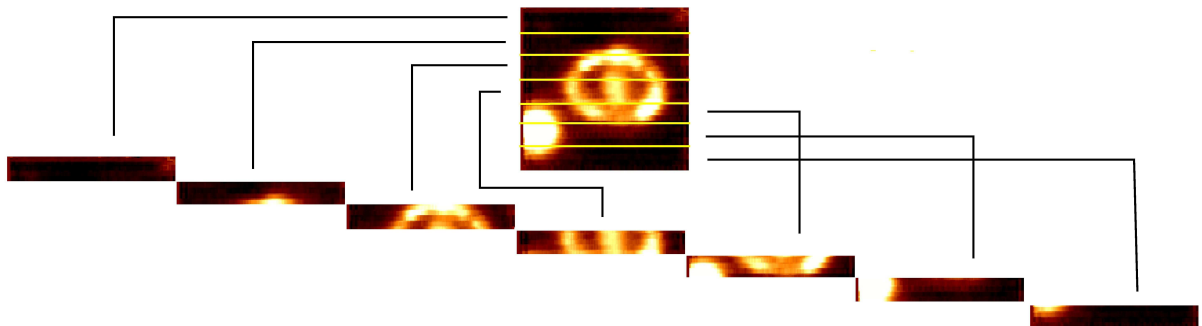

Figure 2.1: The field of view on sky is sliced into 32 slices in SINFONI, here is a simple slicing shown with only 7 slices.

the Strehl Ratio does, will only be meaningful and sensible if the point-spread function is little distorted from its ideal (aberration-free) form. This is valid for well corrected systems that operate close to the diffraction limit. Had we observed a point spread function (PSF) star right after the science observations using the same AO loop as on the target, we would have observed the strehl in the centre of the image plane and been able to deconvolve the overall changes to the brightness profile the AO introduces. Essentially the AO correction changes the PSF profile to have more signal in the core and less in the wings.

Our observations were AO supported using a nearby star (Star 3, 1.65" from the SN) as a reference source for the AO. When Star 3 is in the FOV we should be able to use the shape of the observed PSF of this star to deconvolve the whole image plane. However we are facing three problems: i) the signal from Star 3 is incomplete due to its position close to or at the edge of the FOV, ii) Star 3 has a magnitude of M_B=15, which limits the effectiveness of the AO, and iii) we face a problem with our object being an extended source, which renders such a deconvolvement unreliable (Davies 2007). These three problems combined resulted in us not deconvolving the observations. For future observations we recommend the use of the LASER guide star system to boost the signal of the reference source, and additional observations of PSF stars after each science exposure.

According to the SINFONI user manual (Kissler-Patig & Szeifert 2005) the spectral PSF is different in each plate scale and for different filters. This means that the shape of the emission lines are changed slightly in the observations, and more so for the 25mas plate scale than the 250mas plate scale. This fact has to be taken into consideration when the emission line shapes are examined, because a brighter core of a line might be artificial, as well as strange bumps around the peak of the line. These changes are complicated because they vary with wavelength within one filter. Currently there is no established way to deconvolve this effect.

The infrared night sky is very bright. This air-glow represents the dominant source of background (i.e. foreground) observations at J-, H- and most of the K band. It is mainly radiated by excited levels of the hydroxyl radical OH^-, known as the Meinel bands, which are excited through the reaction:

$$H + O_3 \longrightarrow OH^* + O_2 \tag{2.1}$$

The altitude of the air-glow emission is about 85-100 km, which causes it to affect all terrestrial sites. It is expected to be less at sites nearer the magnetic equator than the magnetic poles. For a thorough discussion on the IR sky see Glass (1999). The sky emission lines are numerous and highly variable. The sky brightness in the emission lines varies on large angular scales and with time, due to passage of gravity waves in the ionosphere. The variations are characterised by spatial periods of tens of km and temporal periods of 5-15 minutes, with amplitudes of typically 10%. A decrease of intensity of order 50% during the night is not unusual.

In our observations we had offset sky observations (presumably blank fields) between the science observations, which we later used to subtract the sky emission. This does not remove the sky lines entirely and the pipeline has an algorithm, which calculate the level of residual skyline emission and subtracts a scaled sky spectrum from the already sky subtracted observations.
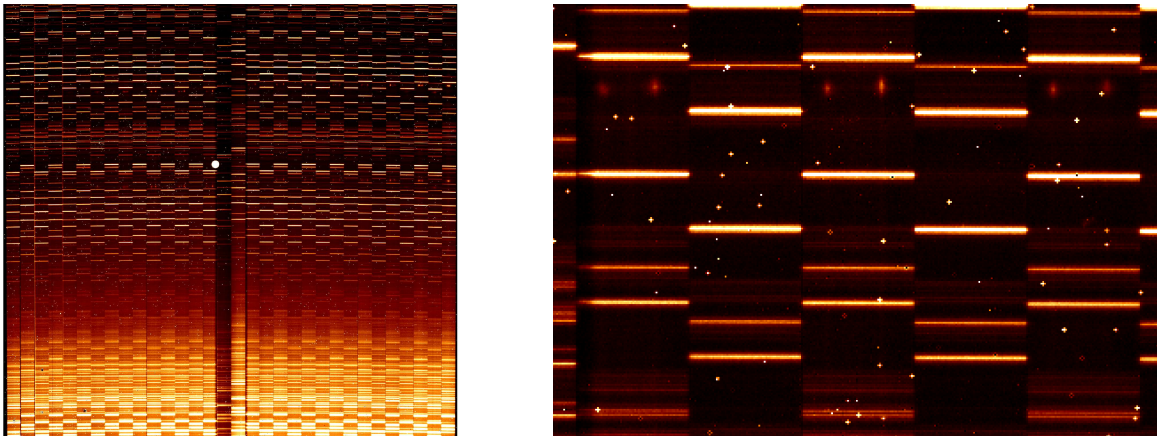
Figure 2.2: Left a raw image from SINFONI, right the zoom of it. The bright lines are skylines. The fainter fuzzier blobs are emission lines from the ring. The little bright spots are either bad pixels or cosmic rays.

2.2 The Pipeline

We use the SINFONI pipeline version 1.2^2 (Schreiber et al. 2004; Modigliani et al. 2007) to reduce and combine the raw data.

The pipeline has recipes for making both intermediate data products and final reduced data. The intermediate data products are files, which are used later in reducing the science frames. Amongst these intermediate files are bad pixel maps, tables with the position of the different slitlets, distortion maps, and wave maps with the wavelength calibration for the observations.

In Figure 2.2 the raw data shows how the slitlets are shifted in the dispersion direction. This helps the pipeline determine when one image slice ends and an other one starts. In the zoom we see that the supernova ring is only detected in every other slitlets. This is because neighbouring slitlets are not originating from image slices next to each other. In fact every second slitlets are neighbouring slitlets in the image plane. If one wants to reduce the data not using the pipeline, the sequence of the slitlets in the raw image needs to be known. In the SINFONI data the upper image slice is imaged in the middle of the detector and its neighbouring slice is imaged skipping the space for one slice towards the edge of the detector. When the imaging of the slices reach the edge of the detector it turns around and image onto every second slice gap until it reached the far end of the detector, where it again turns around and image slices until it reached the position next to the middle. This imaging method reduces the effects bad areas of the detector would have on the observations.

The bright infrared sky is removed in the pipeline. The pipeline subtracts offset sky observations from the science observations, any residual skylines remaining after this are removed by the pipeline, which subtracts a theoretical sky spectrum scaled to fit the measures strength of the residual sky. This step can be suppressed by setting one of the parameters in the data reduction recipes. For the longer exposures it often happens that the sky removal causes P-Cygni like profiles, where the red (or blue) part of the line is more subtracted than the blue (or red) part

---

[2]The pipeline is available at: http://www.eso.org/projects/dfs/dfs-shared/web/sinfoni/sinfo-pipe-recipes.html.

of the skyline. This happens because the sky changes with time, not only in strength but also in its movement. Since all the skylines are narrow, a residual P-Cygni profile remains when the profile for a given line is not matched perfectly. Both the pipelines extra sky removal and this effect sometimes causes negative values in the spectra.

The final data product is a cube (x,y,λ), where the x and y directions are spatial. Because the 32 slitlets each are imaged onto 64 pixels the pixels in the reconstructed cube are rectangular. If the observations are of several exposures and those have been shifted a non integer amount of pixels the observations are dithered and a higher spatial resolution can be achieved. Several exposures in the same band are combined using a mean sigma algorithm, which first establish the distribution of the data points (counts) for each spatial position and each spectral element. Then the point(s) in the tails of the distribution, the outlying 10 % high and low values, is cut away. Finally the mean value is computed. The user can specify a sigma, for which the mean is computed disregarding data points that are more than that sigma away from the majority of the data-points. The size of sigma can be adjusted in the parameter file. We found the default sigma value of 2 to give good results.

2.3   Terminology and Methodology

The 3D data format consists of a cube (spatial x, spatial y, wavelength λ) for each filter/band. The elements in the spatial plane (x,y) are called *spaxels* (as opposed to pixels), since each spaxel is a spectrum. The elements in a cube (x,y) belonging to a single wavelength element is called a *frame*, borrowed from the movie terminology, where a movie is made from many pictures or frames. The spectral resolution sets the distance in wavelength between the frames for a band.

In order to build a normal image in a filter we simply collapse the wavelength dimension by integrating over that axis. In such an integration we add frames, each with a different wavelength together:

$$\text{Image}(x, y) = \sum_{i=1}^{n} (x, y, \lambda_i), \tag{2.2}$$

where n is the length of the wavelength axis. Such an integration is often also referred to as a *map*, especially when the integration range in wavelength only covers one emission line. This way it is possible to map out the spatial distribution of a single emission line.

We can also construct spectra from the cube by integrating over different spatial regions. This way we can imitate a slit of any size or geometry. Spectra constructed from a cube are often called *extractions*, since the spectrum is extracted from the cube. Especially if the extractions are circular the extraction area is called *aperture*, which comes from the optical definition of size of signal included when measuring stars.
A spectrum extracted with a circular aperture is added over the spatial directions:

$$\text{Spectrum}(\lambda) = \sum_{|x_i - x_c| < r} \sum_{|y_i - y_c| < r} (x_i, y_i, \lambda), \tag{2.3}$$

23

where r is the extraction radius of the aperture centred on spaxel (x_c, y_c).

It is important to only compare emission line strengths between extractions of same aperture size, since the flux is very dependent of aperture. When we extract the complete spectrum for the ring and supernova we do not specify the extraction area, since we already have all the signal within our area, which means the flux would not grow with larger area. For all other extractions we scale the flux of the extracted spectrum with the area of the extraction, so we can compare between different extractions.

In the collapsed cubes displaying the FOV of our observations we can measure the full width half maximum (FWHM) of the star(s) in the image. The FWHM is not just the seeing from the atmospheric disturbance and the AO correction, but also a measure of the spatial dispersion in the cube and the spatial resolution. Since the FWHM combines so many distortion effects, we rename it to 'image quality' and use the number as an estimate for reasonable extraction sizes.

We mainly use circular extraction areas because the PSF of a point source in the collapsed cube is close to being circular. Rectangular extraction areas makes here little sense.

At first we adopted the image quality as a radius, reasoning that the area would reflect the maximum spatial area from which the emission originated. This however, only caused additional contamination from surrounding areas. Later we ended up using the image quality as a measure of the diameter, which diminished the contamination, and still seemed a sound praxis. Thus the diameter of the extractions are of the size of the FWHM for a point source.

We could use extractions of one spaxel only, but here it is questionable if the emission is from the given spaxel or from a more luminous neighbouring spaxel.

2.4 Adaptive Voronoi 2D-Binning

There are several tools to help the interpretation of 3D data, most of them are instrument or wavelength specific. There is a significant difference between ground based and space based observations, in that space observations are not affected by the atmosphere created PSF, and thus the binning does not need to enclosure the PSF area on the detector. X-ray observations are implicit 3D data, since each photon carries information about position and energy, and a binning of the photons (each one count in x-rays) is often chosen to be rectangular in shape.

The Adaptive Voronoi 2D-Binning is an IDL algorithm written by Cappellari & Copin (2003), which bins two-dimensional data to a constant signal-to-noise ratio per bin. This routine has been developed for the SAURON (Spectrographic Areal Unit for Research on Optical Nebulae) instrument, which is a panoramic integral-field spectrograph. The programs can easily be used for data not observed with this instrument, and the program performs adaptive spatial binning of Integral-Field Spectroscopy (IFS), X-ray or imaging data. The attractive feature about this technique is the algorithm, which builds a map of bins with equal signal to noise ratio.

In essence the routine is based on three simple requirements of the binning. i) The bins should cover the whole area without overlapping or creating gaps. ii) The shape of the bins should be as compact or round as possible, so that a bin can be associated with a well-defined spatial position. iii) The signal to noise ratio should be as close as possible to each other.

The algorithm starts by the pixel with the highest signal to noise and then the bins are created by accreting pixels to the bins until the requested signal to noise ratio has been reached. In this accretion process the three requirements are kept fulfilled.

When applying the Adaptive Voronoi 2D-Binning to our data we have to consider where this make sense. The most used application of this program is to extract stellar kinematics from galaxies by the SAURON consortium. Their results are displayed as velocity maps, showing the velocity difference at spatial different positions for a galaxy, often revealing the rotation (or lack thereof) in the objects. They use the program on continuum sources and extended objects, which are connected over the whole emission region, and which have a somewhat simple topology.

It make little sense to use the binning on the ring as the emission there is originating from many individual shock sites (spots), which are not (yet) physically connected. Furthermore we would like to bin our data in equally large apertures, which centres are on the ring itself, a requirement this routine cannot securely provide. In the binning we use for the ring, see Chapter 5, we have oversampling in that our bins overlap, but we see this as a necessity in order to catch the spots on the ring, and avoid the case of a spot to be only mapped halfway in one or two bins. Since the flux depends on the aperture size we can only compare flux from equal size apertures.

However, we find the Adaptive Voronoi 2D-binning algorithm useful in mapping the velocity distribution of the ejecta, see Chapter 6. The ejecta emission at spatially different positions share physical properties, in that they once were causally connected.

We adjusted the program to be used on an emission line object, by focussing our attention on one emission line only, and cutting off all the area with the ring and beyond. The signal to noise map was constructed on the emission from one emission line as the signal, and a wavelength range devoid of emission lines as the noise region. The subsequent binning reflects the signal to noise distribution (flux distribution) of this line in the ejecta. This was reasonable as the emission line was connected over the whole emission region. The results of this analysis can be seen in Chapter 6.2.3.

Chapter 3

Data Reduction and Calibration

This chapter describes the data reduction and calibration of two epochs of SINFONI data of SN 1987A and the circumstellar ring interaction. The first epoch is from November 2004 and covers a total of 80 minutes on target in three filters, whereas the second epoch is observed with a higher spatial resolution and a total of 230 minutes on target in three filters, and thus deeper observations.

3.1   Epoch 2004

Our first epoch of SN 1987A observations are from 2004 and consists of Science Verification observations with SINFONI observed by Markus Kissler-Patig on 28 and 29 November 2004 (day 6488/6489, preliminary results were published in Gillessen et al. 2005, to announce first science with SINFONI). Integral-field spectroscopy was obtained in J (1.11-1.35 μm), H (1.49-1.79 μm) and K (1.99-2.38 μm) bands. The observations were AO supported using Star 3 as the reference source. We have not deconvolved the images, since deconvolving extended sources is unreliable (Davies 2007). SN 1987A was observed with two different spatial resolution settings. The primary data in J, H, and K were obtained with a spatial resolution of 250 mas/spaxel and thus with a field of view of 8"×8". In J we also obtained an observation with a spatial resolution of 100 mas/spaxel and a field of view of 3"×3" (denoted as J100 in the following). All single integrations were 600 seconds long and Table 3.1 displays the total integrations per setting. When several integrations were obtained the individual exposures were offset by sub-spaxel spacings to improve the spatial resolution. The exposures were separated by sky exposures of equal integration time in a target-sky sky-target sequence.

The sizes of the spaxels for the observations are 250 mas × 125 mas (and 100 mas × 50 mas for J100). In the K-band images the final image quality is superior to the J and H band due to better seeing and sampling. This can been seen in Figure 3.1, which shows the images (collapsed cubes) for the different bands. In the final, combined data cube the spaxels are square and have the sizes 125 mas × 125 mas (50 mas × 50 mas for the J100). The ring is fully resolved in all bands. Using the stars in the FOV of the collapsed images we measure an image quality (values listed in Table 3.1). The image quality measurement combines seeing, the AO correction and any smearing/dithering in combining the final cube. The image quality is in particular important in estimating reasonable sizes of spectral extractions (apertures), see Chapter 2.
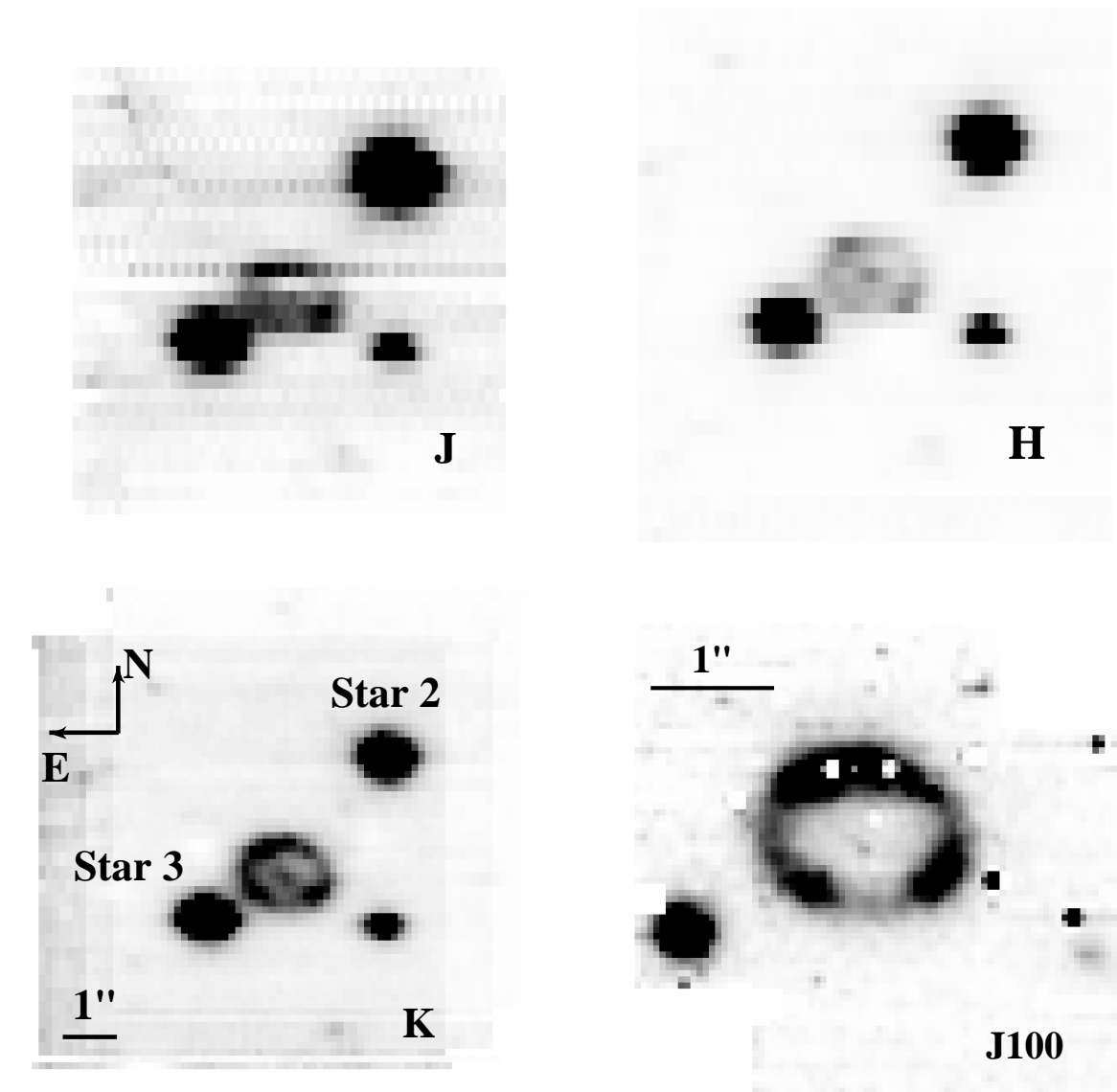
Figure 3.1: The 8"×8" FOV in the J, H and K-band images. Lower right is the higher resolution J-band 3"×3" FOV.

Table 3.1: Summary of observations of epoch 2004. The rows designate the observation date (UT), the time since the explosion of SN 1987A on 23 February 1987A, the spaxel size of the observation, the wavelength range of the spectrograph setting, the spectral resolution, the total exposure time and the image quality as measured from the combined data cube on Star 2 and Star 3. We further list the standard stars used for the flux calibration, and the uncertainty in the flux as determined from a comparison of Star 2 from the corresponding black body curve, the uncertainty in the wavelength calibration as measured from night sky lines and the corresponding uncertainty in velocity.

	J	H	K	J100
Date	2004/11/28	2004/11/29	2004/11/29	2004/11/28
Day	6488	6489	6489	6488
Spatial Res.	250mas	250mas	250mas	100mas
Wavelength	1.11-1.35 μm	1.487-1.792 μm	1.985-2.375 μm	1.11-1.35 μm
$\lambda/\Delta\lambda$	2000	2000	4500	2000
Exptime	600s	1200s	1800s	1200s
Image quality	0.62"	0.46"	0.48"	0.32"
Std. Star	HD36531	HD29303	HD29303	HD36531
ϵ_{Flux}	1 %	13 %	4 %	4 %
$\delta(\lambda)$	8×10^{-5} μm	7×10^{-5} μm	7.5×10^{-5} μm	8×10^{-5} μm
$\delta(v)$	19 km s^{-1}	12 km s^{-1}	11 km s^{-1}	19 km s^{-1}

The data have been reduced and recombined into data cubes using the SINFONI pipeline (Schreiber et al. 2004; Modigliani et al. 2007). We crosschecked the wavelength solution with the atmospheric OH lines (Rousselot et al. 2000) and the resulting wavelength calibration is accurate to $8\times10^{-5}\mu$m, $7\times10^{-5}\mu$m and $7.5\times10^{-5}\mu$m, in J, H and K, respectively. This corresponds to systematic velocity uncertainties of 19 km s^{-1}, 12 km s^{-1}, and 11 km s^{-1}, as listed in Table 3.1.

Reddening Correction

The interstellar dust in the Large Magellanic Cloud (LMC) and Milky Way (MW) redden the light, which is best expressed via the extinction law from Cardelli et al. (1989):

$$\langle\frac{A(\lambda)}{A(V)}\rangle = 0.574 \cdot x^{1.61} - \frac{0.527}{R_V} \cdot x^{1.61}, \tag{3.1}$$

which is valid for $0.3\mu m^{-1} \leq x \leq 1.1\mu m^{-1}$, where x=1/$\lambda$ (in microns) and the absorption, A, is measured in magnitudes. Using the approximation $A_V \approx R_V\cdot$ E(B-V) and noting that this is an average extinction law we get:

$$\langle A(\lambda)\rangle = A_V \cdot (0.574 - \frac{0.527}{R_V}) \cdot x^{1.61}$$

$$\langle A(\lambda)\rangle = R_V \cdot E(B-V) \cdot (0.574 - \frac{0.527}{R_V}) \cdot x^{1.61}$$

$$\langle A(\lambda)\rangle = E(B-V) \cdot (R_V \cdot 0.574 - 0.527) \cdot x^{1.61}$$

We de-reddened the spectra using the galactic extinction law equation 3.1, assuming $R_V = 3.1$, and E_{B-V}=0.16 (Fitzpatrick & Walborn 1990) for the colour excess towards SN 1987A, based on E_{B-V}=0.10 from the LMC and E_{B-V}=0.06 from the Milky Way (Staveley-Smith et al. 2003). The differences between the LMC and galactic extinction law are negligible at low colour excess in the near-IR. This gives:

$$
\begin{aligned}
\langle A(\lambda) \rangle &= 0.16 \cdot (3.1 \cdot 0.574 - 0.527) \cdot x^{1.61} \\
\langle A(\lambda) \rangle &= \frac{0.200}{\lambda^{1.61}}
\end{aligned}
$$

Flux Calibration

Standard stars were observed directly before or after the supernova and have been used to remove the telluric features (i.e. the absorption and emission from the atmosphere). We used the standard stars to construct a sensitivity curve and derive the flux calibration, based on their measured magnitudes from the 2MASS catalogue (Cohen et al. 2003). In this way the whole data cube had the same flux calibration, and we could derive calibrated spectra for Stars 2 and 3 as well. To test the absolute flux calibration we compared the spectrum of Star 2 (a B2 star NW of the SN, Walborn et al. 1993) with the blackbody curve of a star with R=8.3 $R_\odot$ and T_{eff}=22500 K at the distance of 50 kpc, see Figure 3.2. These values for the star are reasonable when considering a type B2 star (Trundle et al. 2007). The derived flux differences are of the order of 10% and are listed as ϵ_{Flux} in Table 3.1. For the J100 observations we calibrated the flux using Star 3, since Star 2 is not in this smaller FOV. As Star 3 is variable we used the observed values of Star 3 in the J250 to cross correlate the value. The total flux from Star 3 observed in J100 was 4% different from the total flux from Star 3 obtained from J250 using the same aperture in arcseconds. We combined the two J observations into one spectrum weighting the spectra with the exposure time. The flux error estimate for this combined spectrum is of the order of 2%. We do not think that any emission contamination from the ring will influence the result beyond the 10% we find as the accuracy of the flux.

3.2   Epoch 2005

Based on the 2004 epoch we had seen that the emission lines had enough flux to be observed with the 100mas setting, which would spread the faint object over a larger area of the detector. For this second epoch we thus chose to observe with the higher spatial resolution of 100×50mas/pixel for all bands, and thus with a field of view of 3"×3".
The observations were AO supported using Star 3 as the reference source. Table 3.2 displays a summary of the observations. All single integrations were of 600 seconds and Table 3.2 displays the total integrations per band. When several integrations were obtained the individual exposures were offset by sub-spaxel spacings to improve the spatial resolution. The exposures were separated by sky exposures of equal integration time in an object-sky sky-object sequence as the 2004 observations. Since the observations were carried out on 5 separate nights we had to take several parameters into account, when we combine the different nights. As can be seen in Table 3.2 the airmass for each band and the heliocentric velocity are sufficiently close in value within each band.
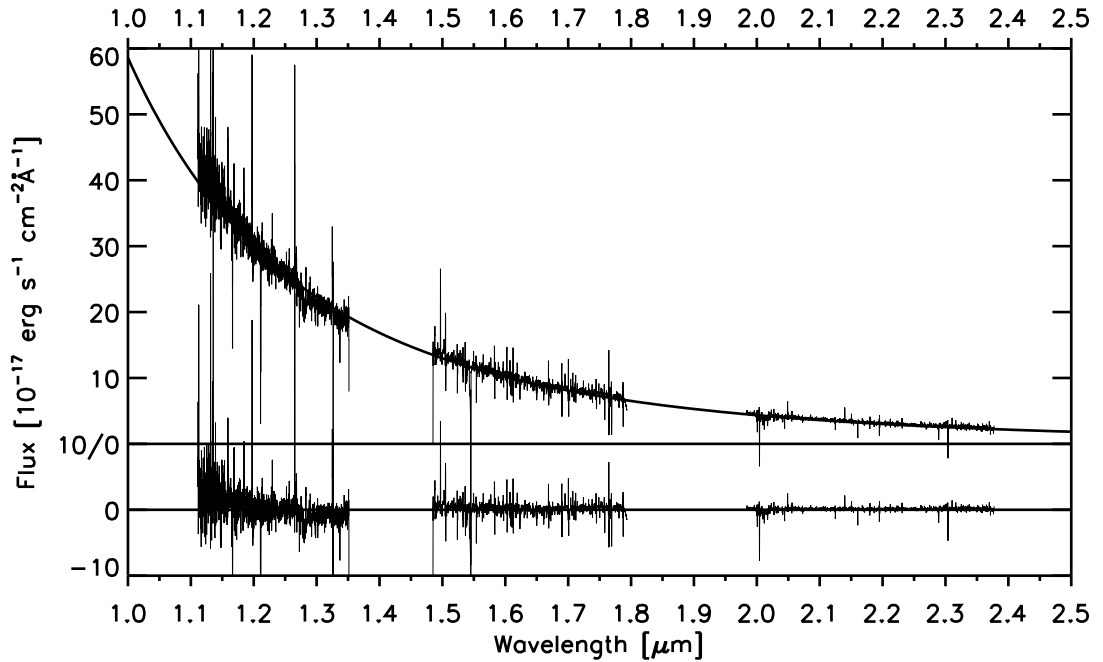
Figure 3.2: Flux calibration check on Star 2. The black body curve is the theoretical curve for Star 2. The observed J, H and K spectrum for Star 2 is plotted on top (aperture of 2"). The bottom panel shows the residuals.

Table 3.2: Summary of the observations of epoch 2005. Each filter was observed on three different nights. The day after explosion (Day), standard star, helio centric velocity (v_{helio}) and total exposure time (Exp) are listed for each separate observation night and filter.

Band	Exp	Date	Std. Star	v_{helio}	Airmass	Day
J	1200	22/10/2005	HD 76233	-1.9 km/s	1.42	6816
J	3000	31/10/2005	CCDMJ03187	-2.1 km/s	1.42	6825
J	600	18/11/2005	HD 46976	-2.1 km/s	1.46	6843
H	1200	22/10/2005	HD 76233	-2.0 km/s	1.41	6816
H	1200	31/10/2005	HD 52447	-2.0 km/s	1.42	6825
H	1800	18/11/2005	HD 46976	-2.0 km/s	1.41	6843
K	1200	30/10/2005	HD 58112	-1.9 km/s	1.54	6824
K	1200	31/10/2005	HD 52447	-1.9 km/s	1.48	6825
K	3000	14/11/2005	HD 94108	-2.0 km/s	1.48	6839

We flux calibrated each night separately using the standard stars and the 2MASS values for their magnitudes or colours. In the flux-calibration the observed standard star spectrum is divided by a template spectrum for that type of star in order to isolate the instrument response and telluric features. For that we use the theoretical temperature values corresponding to the type of star, listed in Table 3.3. For the B type standard stars we superimposed hydrogen absorption features (scaled to the features observed in the standard stars) on the Planck curve for the given temperature and used that as the stellar template. For the G type stars we use the solar spectrum scaled with the observed absorption features in the standard star and brought it to the spectral resolution of the standard star. For the 2004 data set all the standard stars were G types and we used the same approach back then.

After having flux-calibrated and corrected for reddening for each night we combined the data-cubes from individual nights in each band. Since the pipeline washes away all coordinate information relating the sky positions to the image positions, we had to use the images (collapsed cubes) from each night in order to find the shift between the different nights. In doing so we allowed for half pixel shifts in both directions (x and y) causing each pixel to be divided into four pixels. This higher spatial resolution is thus caused by sampling, the resulting spatial resolution is shown in Table 3.4. As can be seen from Figure 3.3 the sampling did not improve the resolution for every band, the observations for the H band were dithered the best, where the J band observations were not shifted in position for the different exposures. We chose an algorithm to combine the nights, where the nights are weighted by their exposure time, so that a longer exposure time would result in a higher weight. When we combined the cubes we used the **sigma_clip** program for **IDL** in order to reduce the noise. This algorithm omits data points 1.5 sigma away from the mean value. For the H band we had to throw out one exposure that was bad. For convenience we computed the resulting data cubes in all bands to have the same pixel scale: 0.025"/px, the spatial resolution listed in Table 3.4 is a measure for at which level these pixels are identical.

The resulting data cubes for the different bands will in the following Chapters be used for the analysis. Table 3.4 lists some important parameters for the reduced and combined data cubes and Figure 3.3 shows the cubes collapsed into images.

As with the 2004 data-set we would like to check the flux-calibration, but the only star in the FOV is Star 3 and it is only partial present. Since flux calculations are sensitive to aperture we are not able to extract the spectrum of Star 3 completely in all bands and compare it with the

Table 3.3: Summary of the standard stars and their values. The magnitudes are from 2MASS and Temp refers to the theoretical values of the surface temperature (in Kelvin) for the type of star denoted in Type.

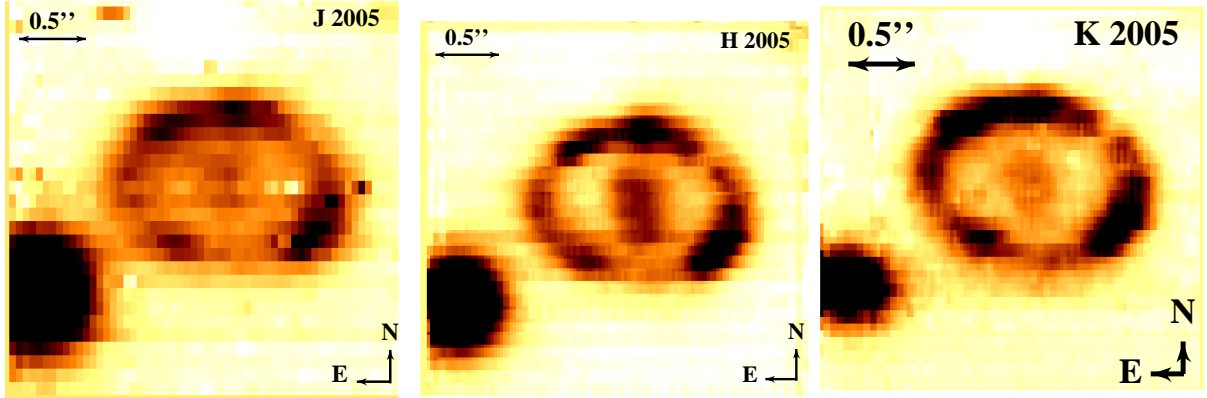| Star	J	H	K	Type	Temp
HD 76233	7.264	7.306		B6V	17140 K
CCDMJ03187	7.12			G2V	5780 K
HD 46976	7.986	8.039		B9V	11710 K
HD 52447		7.103	7.027	G0V	6000 K
HD 58112			8.92	B4V	17200 K
HD 94108			8.29	B4V	17200 K

Figure 3.3: The 3"×3" FOV in the J, H and K-band images.

Table 3.4: Summary of the combined data-cubes. The total exposure times for the combined cubes are listed in the row marked 'Exptime' in seconds. The pixel size is spatial resolution after the nights are combined.

	J	H	K
Exptime	4800s	3600s	5400s
Spatial resolution	50×100 mas/pixel	25×25 mas/pixel	25×50 mas/pixel
$\lambda/\Delta\lambda$	1700	2300	3500
σ_{instr}	176 km/s	130 km/s	86 km/s
Image Quality x	0.275"	0.10"	0.175"
Image Quality y	0.375"	0.175"	0.275"
wavelength range	1.09-1.35	1.473-1.797	1.941-2.462
$\delta(\lambda)$	0.0000125 mμ	0.000021 mμ	0.000024 mμ
$\delta(v)$	3 km/s	4 km/s	3 km/s

theoretical prediction. It is unfortunately not possible to use the 2004 epoch to calibrate against, since the object is changing. The H band emission is dominated by the cool ejecta, whereas the J and the K band are more dominated by the ring. Furthermore, the noise level in the J band observations from 2004 is much higher than for 2005, which would lead to a systematic error. Instead we estimate, that the errors of the flux calibration should be of the order of the errors found for the 2004 data set, since the method was the same. An upper value for ϵ_{flux} in 2004 was 10%, and we will in the following use the same value.

Luckily we can still use star 3 to measure the *image quality* as the FWHM of the star, since only the wings of the PSF of the star is outside the FOV. The values are listed in Table 3.4 separately for x and y. Generally the FWHM is larger in the y-direction than the in the x-direction. This is also seen directly in Figure 3.3 where Star 3 is elongated in the North South direction. In the following Chapters we will use the larger y-value for the image quality, when we extract spectra using a circular aperture.

The calculation of $\lambda/\Delta\lambda$ was, like in the 2004 data set, based on measurements of narrow sky-lines in the whole spectrum. We checked the pipeline wavelength calibration against the known position of the skylines and from that determined an accuracy of the wavelength calibration as the root mean square of the correction value. The systematic error of the wavelength calibration is found to be $1.25 \times 10^{-5}\mu$m, $2.1 \times 10^{-5}\mu$m and $2.4 \times 10^{-5}\mu$m, in J, H and K, respectively. This corresponds to systematic velocity uncertainties of 3 km s^{-1}, 4 km s^{-1}, and 3 km s^{-1}, as listed in Table 3.4. This was done using the task **identify** in IRAF.

The wavelength range has increased in the 2005 data set because the detector was replaced between the two epochs. Previously bad pixels rendered the end of the spectra useless.

Figure 3.4 show a 3 colour image of the J (blue), H (green) and K (red) combined. We here clearly see that the central emission is very green and thus originating in the H band, and that the star is white due to emission from all bands.
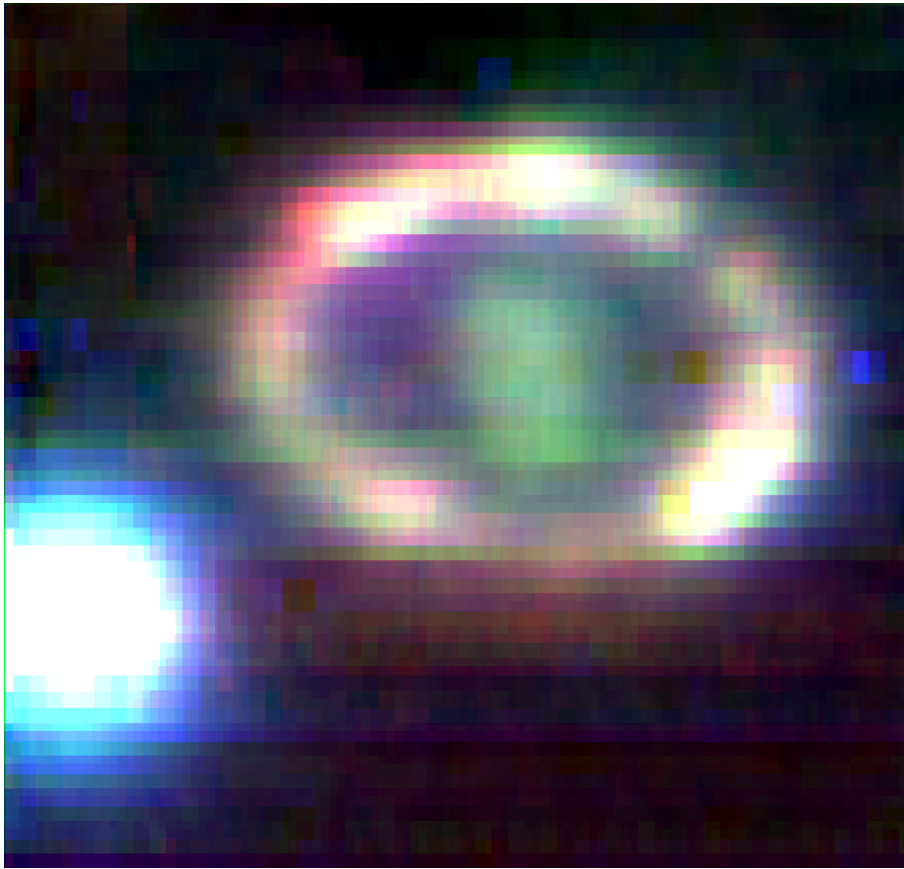
Figure 3.4: A RGB image of the J, H and K band combined. J is blue, H green, and K is red.

Chapter 4

Data Analysis

In this chapter the total spectrum of SN 1987A is shown for both epochs. This is the spectrum that one would get, when there is no spatial information in the data and thus these spectra can be compared with the spectra from other years.

4.1   Epoch 2004

In order to compare with previous data we summed up the circumstellar ring and the ejecta (which corresponds to 281 spaxels co-added for the 250 mas data cubes). We extracted the spectrum in a similar way for the J100 observations and scaled this spectrum to the J spectrum before we combined the spaxels into a single spectrum. We chose to scale the J100, because the aperture for the J band is easily compared with the ones of the H and K bands, which were observed with the same spatial scale. This spectrum should be comparable with earlier spectra of SN 1987A after a slit correction. We will refer to the spectrum extracted this way as the 'integrated spectrum' and it is displayed in Figure 4.1. We also show a sky spectrum offset below the 'integrated spectrum'. This sky spectrum should be seen as a help to estimate where the more noisy regions are located in wavelength. The intensity of the various skylines cannot be directly compared with the integrated spectrum due to differences in aperture.

A very weak continuum flux can be discerned in the spectrum at $(2-3) \times 10^{-17} \mathrm{ergs}^{-1} \mathrm{cm}^{-2} \mathrm{\AA}^{-1}$. The consistency of this continuum in all three bands makes us believe that it is real. The origin of this continuum is not clear, but it could come from large scale emission in the region. If it does indeed emerge from the ring system itself then it could be a weak H/He continuum. Most likely the continuum is a combination of several emission origins, and it is at the moment not possible to distinguish between them.

The detected lines from the spectrum are listed in Tables 4.1, 4.2 and 4.3. The weakest lines we have been able to securely identify are those with a flux above 3×10^{-16} erg s^{-1} cm^{-2}. In the tables λ_{obs} denotes the observed wavelength (in air), λ_{air} is rest wavelength in air for the line transition listed under 'Identification'. The heliocentric velocity of a given line is listed in column v$_{obs}$ and calculated as the velocity shift between the observed wavelength and the rest wavelength for the identification and then corrected for heliocentric velocity found by the task
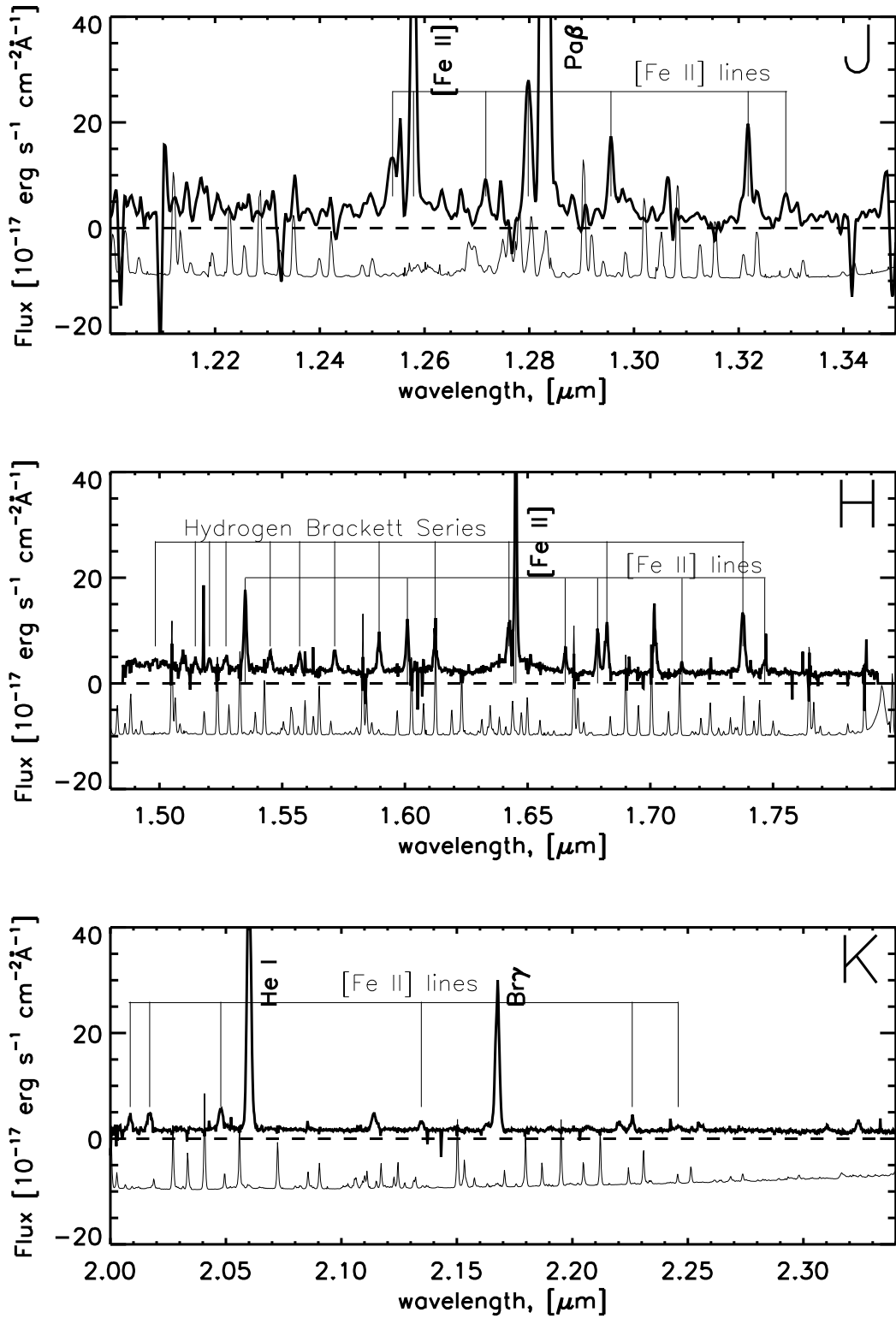
Figure 4.1: The integrated spectrum of the ring and the ejecta in 2004. The sky spectrum is shown offset below the SN ring spectrum. Note that the flux of the sky spectrum has been scaled down to make the spectrum fit in the same figure as the object. The line identifications are given in Table 4.1-4.3.

Table 4.1: Emission lines of the integrated spectrum (ejecta and circumstellar ring combined corresponding to the central 281 spaxels) in the J band 2004. The spectral resolution is 150 km s^{-1} in the J band. Errors for the values listed in the table are given either in the text or in Table 3.1. The flux is measured in 10^{-16}erg s^{-1} cm^{-2}. The source for the line identification (NIST) is discussed in the text.

λ_{obs} (μm)	σ_{obs} (km s^{-1})	σ_{deconv} (km s^{-1})	Flux	Identification	λ_{air} (μm)	v$_{obs}$ (km s^{-1})
1.2539	431	404	14	*[Fe II] a^{6}D$_{3/2}$-a^{4}D$_{1/2}$	1.2521	408
				*He I 1s3s-1s4p(3S-3P)	1.2528	261
Blend? The line transition probability for [Fe II] does not support this large flux. Furthermore large σ_{deconv}.						
1.2579	200	132	69	†[Fe II] a^{6}D$_{9/2}$-a^{4}D$_{7/2}$	1.2567	277
1.2717	236	182	7	†[Fe II] a^{6}D$_{1/2}$-a^{4}D$_{1/2}$	1.2703	315
1.2798	305	266	43	†[Fe II] a^{6}D$_{3/2}$-a^{4}D$_{3/2}$	1.2788	245
				* He I 1s3d-1s5f(3D-3F)	1.2785	310
Blend? The line transition probability for [Fe II] does not support this large flux.						
1.2830	281	238	367	†Paβ	1.2818	277
1.2956	190	117	18	†[Fe II] a^{6}D$_{5/2}$-a^{4}D$_{5/2}$	1.2943	311
1.3065	253	204	12	*NI	1.3052	302
1.3218	166	71	23	†[Fe II] a^{6}D$_{7/2}$-a^{4}D$_{7/2}$	1.3206	277
1.3290	339	304	10	†[Fe II] a^{6}D$_{3/2}$-a^{4}D$_{5/2}$	1.3278	226

The lines marked with † have been observed previously for this object in Meikle et al. (1993). The lines marked with * are new for this object or have a new identification.

Table 4.2: Emission lines in the integrated spectrum (ejecta and circumstellar ring combined corresponding to 281 spaxels) in H 2004. The spectral resolution is 150 km s^{-1} in the H band. Errors for the values listed in the table are given either in the text or in Table 3.1. The flux is measured in 10^{-16}erg s^{-1} cm^{-2}. The source for the line identification (NIST) is discussed in the text.

λ_{obs} (μm)	σ_{obs} (km s^{-1})	σ_{deconv} (km s^{-1})	Flux	Identification	λ_{air} (μm)	v$_{obs}$ (km s^{-1})
1.4983	320	283	2	*HI Br25	1.4967	301
1.5099	278	234	5	† HeI 3s^{1}S-4p^{1}P^0	1.5084	295
1.5146	257	209	3	* HI Br21	1.5133	253
1.5204	276	232	3	* HI Br20	1.5192	232
1.5271	334	298	4	* HI Br19	1.5261	197
1.5349	254	205	19	†[Fe II] a^{4}F$_{9/2}$-a^{4}D$_{5/2}$	1.5335	285
1.5451	272	227	5	* HI Br17	1.5439	237
1.5571	270	224	5	* HI Br16	1.5556	273
1.5714	305	266	7	†HI Br15	1.5701	257
1.5895	283	240	10	†SiI 4s^{1}P^0-4p^{1}P	1.5880	273
				† HI Br14	1.5881	267
The transition probability for Br14 alone fits with the flux. SiI identification tentative.						
1.6010	225	168	11	†[Fe II] a^{4}F$_{7/2}$-a^{4}D$_{3/2}$	1.5995	281
1.6123	279	235	12	† HI Br13	1.6109	257
1.6424	219	160	12	† HI Br12	1.6407	298
1.6444	3393	3390	47	†[Fe II] a^{4}F$_{9/2}$-a^{4}D$_{7/2}$	1.6435	150
Broad component. See text for comments.						
1.6452	171	82	51	†[Fe II] a^{4}F$_{9/2}$-a^{4}D$_{7/2}$	1.6435	296
This component sits on top of the broad component (previous line).						
1.6653	234	180	6	†[Fe II] a^{4}F$_{5/2}$-a^{4}D$_{1/2}$	1.6638	282
1.6785	233	178	12	†[Fe II] a^{4}F$_{7/2}$-a^{4}D$_{5/2}$	1.6769	290
1.6823	268	222	15	† HI Br11	1.6807	286
1.7017	247	196	15	†HeI 3p^{3}P^0-4d^{3}D	1.7002	259
1.7129	263	216	3	†[Fe II] a^{4}F$_{5/2}$-a^{4}D$_{3/2}$	1.7111	307
1.7377	311	272	21	† HI Br10	1.7362	254
1.7466	327	291	6	†[Fe II] a^{4}F$_{3/2}$-a^{4}D$_{1/2}$	1.7449	286

The lines marked with † have been observed previously for this object.

The lines marked with * are new for this object or have a new identification.

Table 4.3: Emission lines in the complete spectrum (ejecta and circumstellar ring combined corresponding to 281 spaxels) in K 2004. The spectral resolution is 67 km s^{-1} in the K band. Errors for the values listed in the table are given either in the text or in Table 3.1. The flux is measured in 10^{-16}erg s^{-1} cm^{-2}. The source for the line identification (NIST) is discussed in the text.

λ_{obs} (μm)	σ_{obs} (km s^{-1})	σ_{deconv} (km s^{-1})	Flux	Identification	λ_{air} (μm)	v_{obs} (km s^{-1})
2.0086	239	229	5	†[Fe II] a^{4}P$_{1/2}$-a^{2}P$_{1/2}$	2.0067	275
2.0170	327	317	8	* [Fe II] a^{2}G$_{9/2}$-a^{2}H$_{9/2}$	2.0151	272
2.0478	293	285	8	†[Fe II] a^{4}P$_{5/2}$-a^{2}P$_{3/2}$	2.0460	259
2.0600	291	283	108	†HeI 2s^{1}S-2p^{1}P^0	2.0581	275
2.1141	369	363	8	*HeI 1s3p-1s4s	2.1121	279
2.1346	267	258	3	†[Fe II] a^{4}P$_{3/2}$-a^{2}P$_{3/2}$	2.1328	258
2.1633	416	411	4	*		
Which could be part of a broad component of Brγ (not seen on the red side of Brγ).						
2.1675	291	283	58	† HI Brγ	2.1655	277
2.1905	575	571	3	*		
2.2066	381	375	2	*NaI 2p^{6}5p $- $ 2p^{6}9s	2.2047	255
2.2066	381	375	2	or † NaI 4s^{2}S $-$ 4p^{2}P^o	2.2070	-58
2.2203	365	359	4	*		
2.2259	243	234	5	* [Fe II] a^{2}G$_{9/2}$-a^{2}H$_{11/2}$	2.2238	290
2.2458	534	530	4	†[Fe II] a^{4}P$_{1/2}$-a^{2}P$_{3/2}$	2.2436	286
Blend? The line transition probability for [Fe II] does not support this large flux. Furthermore large σ_{deconv}.						
2.2553	452	447	3	*		
2.3103	403	397	3	*NiII 3p^{6}3d^8(^{3}F)4s $-$ 3p^{6}3d^8(^{3}F)4s	2.3079	304
2.3238	284	276	5	*OI 2s^{2}2p^3(^{2}D)3s $-$ 2s^{2}2p^3(^{4}S)5f	2.3215	291

The lines marked with † have been observed previously for this object.
The lines marked with * are new for this object or have a new identification.
The lines 2.24-2.32 μm were observed in Meikle et al. (1993) as a blended unidentified feature.

rvcorrect in **IRAF**. σ_{obs} is the observed FWHM of the line and σ_{deconv} refers to the FWHM for the line corrected for the instrument resolution ($\sigma_{deconv} = \sqrt{\sigma_{obs}^2 - \sigma_{instr}^2}$). The integrated flux for the line is measured by fitting a Gaussian to the line shapes (in **IRAF** using **splot**) and listed in the column labelled 'Flux' in the tables. We chose to ignore unresolved narrow lines, which we could identify as residue sky subtraction lines using the OH line catalogue of Rousselot et al. (2000). Since we have a 3D data format we could investigate the spatial extent of each line in the integrated spectrum and check whether the line originated at a particular point in the object or whether it has a coherent appearance across the ring/ejecta. This is a very effective way to check for artefacts, such as hot/bad pixels. All observed values are integrations over the whole ring.

We have used the NIST Atomic Spectra Database Version 3.1.0. (Martin et al. 2003) to identify the lines, checking the following elements and their ions: H, He, C, N, O, Na, Mg, Si, S, Ca, Fe, Co, and Ni. The ions included in the NIST database are up to ionisation XXIV for the case of iron. The other elements are complete to a similar level. The few lines which we have not yet identified did not correspond to any of the mentioned elements using the NIST database version 3.1.0, which is not necessarily complete for these elements and all their ions. The accuracies of the wavelengths in NIST are implied by the number of significant figures.

For the [Fe II] and HI lines we have verified the identification by checking line ratios using the line transition probabilities from Nussbaumer & Storey (1988) and the NIST database, see Appendix A for more on this topic. The broad component in the H-band (Table 4.2) is the [Fe II]1.644 μm line originating in the ejecta. The flux from the intermediate/narrow component sitting on top of the broad component alone agrees well with the fluxes observed from the 1.257 μm and 1.321 μm [Fe II] lines, which come from the same upper level. However, if the broad component is the [Fe II]1.644 μm line then we should expect to see broad components from the lines [Fe II]1.257 μm and 1.321 μm as well. Given the S/N in our J observations they are not discernible. The two lines are located in a noisy region of the J-band especially when compared with the H-band region around the 1.644 μm line. This point can hopefully be resolved with higher signal to noise data.

When the identification transition in Tables 4.1-4.3 is preceded with a dagger (†), this transition has been observed previously and was identified by Meikle et al. (1993) or Fassia et al. (2002). Generally, the ring lines are now brighter than for those observations, as expected if the shocked component dominates the narrow component from the unshocked ring. With the higher spectral resolution of SINFONI we can now resolve some previously blended lines. However, there remain blends for lines with a true separation of less than 150 km s^{-1}. We mark newly identified lines with an asterisk (*) in the tables.

From HST spectroscopic observations (in the optical, Pun et al. 2002) and ground-based high-resolution spectroscopy (Gröningsson et al. 2006, 2007), we know that the ring-ejecta system at the moment contains three different velocity components. There is the narrow component (NC), which displays a nearly Gaussian velocity distribution, with $\sigma \sim 10$ km s^{-1}, arising from the unshocked circumstellar ring. This is caused by fluorescence from the material recombining

after being ionised by the supernova's UV flash at shock breakout (Fransson & Lundqvist 1989; Lundqvist & Fransson 1991). The intermediate component (IC), with $\sigma \sim 200 - 300$ km s^{-1}, originates from the shocked ring material behind the passing shock front. The brightening has been observed in HST imaging (Michael et al. 1998, 2000; Pun et al. 2002) and arises from this material, where the ejecta collides with the inner protrusions of the ring. In our observations the NC and IC cannot be separated and appear as a single marginally resolved component. The SN ejecta component with an expansion velocity of ~ 15000 km s^{-1} comes from the interaction with the reverse shock (Smith et al. 2005; Heng et al. 2006) and is not evident in our data. We also observe a broad component (BC) which will be discussed further in Chapter 6.

Because we do not have the spectral resolution to separate the narrow from the intermediate-velocity component (cf. Tab. 3.1) we expect some of the intermediate lines we observed to be a convolution of the narrow component[1] with the intermediate component. In addition we have integrated spatially over the whole ring and thus the lines are also broadened by the velocity dispersion of the ring, (see the discussion in Chapter 5). With the 3D data format we can emulate slit observations and thus better compare with observations from different instruments and telescopes. Figure 4.2 shows a comparison of [Fe II] emission lines observed with UVES and SINFONI (the UVES data observed half a year later (March 2005) than the SINFONI), where the UVES data has been scaled up by a factor of 100. The SINFONI J100 observations have been convolved to the seeing of the UVES observations (0.5"). We extracted two spectra, one North and one South on the circumstellar ring emulating the 0.8" slit (PA=30°), which was the setup of the SN 1987A observations with UVES. The UVES spectra from the North and South part were convolved with the spectral resolution of SINFONI ($\lambda/\Delta\lambda \sim$2000 in the J-band) and shown in the figure as the dashed (red) curve. Taking into account that the wavelength accuracy in the J-band is $\pm$ 19 km s^{-1} then we have a fair agreement for the peak velocity between the two observations.

4.2 Epoch 2005

The integrated spectrum of October/November 2005 shown in Figure 4.3 has been extracted from the cubes using a circular aperture of 1.15" radius. The ejecta and ring emission are fully enclosed within this radius and thus the strength of the emission lines should be directly comparable with slit corrected spectra from other observations and the spectra from epoch 2004. The detected emission lines have been listed in Table 4.4-4.6.
As for the 2004 epoch we checked the new emission lines detected in the 2005 epoch against their spatial extensions to see if they were coherent across the ring. Since we have a better signal to noise in the 2005 with respect to the 2004 dataset, there is a number of new lines we are able to discern in the 2005 epoch (see the next section).
Like for the 2004 epoch we can discern a very weak continuum flux, now a bit weaker at

---

[1]The narrow component has never been directly observed in the near infrared, because of the limited spectral resolution of the available instruments. We have (P.I: C. Fransson) scheduled observations on a new high resolution spectrograph (CRIRES, Cryogenic High-Resolution IR Echelle Spectrograph) in Nov. 2007. We attempted to get observations last winter (2006) with this instrument in the commissioning phase (P.I. Kjær, proposal ID: 60.A-9085), but without any results due to bad weather conditions.

Table 4.4: Emission lines of the integrated spectrum (ejecta and circumstellar ring combined within a circular aperture of 1.15") in the J band 2005. The spectral resolution is 176 km s^{-1} in the J band. Errors for the values listed in the table are given either in the text or in Table 3.4. The flux is measured in 10^{-16}erg s^{-1} cm^{-2}. The source for the line identification (NIST) is discussed in the text.

λ_{obs}	σ_{obs}	σ_{deconv}	Flux	Identification	λ_{air}	v_{obs}
(μm)	(km s^{-1})	(km s^{-1})			(μm)	(km s^{-1})
1.1637	335	286	10	$*MgII 2p^65g - 2p^67h$ †	1.1620	437
1.1894	390	348	7	*		
1.1980	360	314	10	*		
1.2537	359	313	24	*[Fe II] a^{6}D$_{3/2}$-a^{4}D$_{1/2}$	1.2521	375
				*He I 1s3s-1s4p(3S-3P)	1.2528	208
Blend? The line transition probability for [Fe II] does not support this large flux.						
1.2579	212	119	93	†[Fe II] a^{6}D$_{9/2}$-a^{4}D$_{7/2}$	1.2567	293
1.2716	224	139	7	†[Fe II] a^{6}D$_{1/2}$-a^{4}D$_{1/2}$	1.2703	298
1.2798	328	277	63	†[Fe II] a^{6}D$_{3/2}$-a^{4}D$_{3/2}$	1.2788	239
				* He I 1s3d-1s5f(3D-3F)	1.2785	310
Blend? The line transition probability for [Fe II] does not support this large flux.						
1.2830	304	248	577	†Paβ	1.2818	288
1.2955	255	184	18	†[Fe II] a^{6}D$_{5/2}$-a^{4}D$_{5/2}$	1.2943	282
1.2990	482	449	12	*		
1.3219	216	125	23	†[Fe II] a^{6}D$_{7/2}$-a^{4}D$_{7/2}$	1.3206	286
1.3291	226	141	9	†[Fe II] a^{6}D$_{3/2}$-a^{4}D$_{5/2}$	1.3278	279

The lines marked with † have been observed previously for this object in Meikle et al. (1993).

The lines marked with * are new for this object or have a new identification.

Table 4.5: Emission lines of the integrated spectrum (ejecta and circumstellar ring combined within a circular aperture of 1.15") in the H band 2005. The spectral resolution is 130 km s^{-1} in the H band. Errors for the values listed in the table are given either in the text or in Table 3.4. The flux is measured in 10^{-16}erg s^{-1} cm^{-2}. The source for the line identification (NIST) is discussed in the text.

λ_{obs} (μm)	σ_{obs} (km s^{-1})	σ_{deconv} (km s^{-1})	Flux	Identification	λ_{air} (μm)	v_{obs} (km s^{-1})
1.4951	570	555	1	*		
1.4978	320	293	1	*HI Br25	1.4967	222
1.5012	360	335	1	*		
1.5094	278	246	4	† HeI 3s^{1}S-4p^{1}P^0	1.5084	190
1.5144	436	416	4	* HI Br21	1.5133	217
1.5203	493	476	5	* HI Br20	1.5192	222
1.5271	354	329	3	* HI Br19	1.5261	201
1.5348	293	263	21	†[Fe II] a^{4}F$_{9/2}$-a^{4}D$_{5/2}$	1.5335	248
1.5450	291	261	4	* HI Br17	1.5439	217
1.5570	251	214	3	* HI Br16	1.5556	271
1.5714	306	276	5	†HI Br15	1.5701	244
1.5894	321	293	7	†SiI 4s^{1}P^0-4p^{1}P	1.5880	256
				† HI Br14	1.5881	237

The transition probability for Br14 alone fits with the flux. SiI identification tentative.

λ_{obs} (μm)	σ_{obs} (km s^{-1})	σ_{deconv} (km s^{-1})	Flux	Identification	λ_{air} (μm)	v_{obs} (km s^{-1})
1.6008	244	206	12	†[Fe II] a^{4}F$_{7/2}$-a^{4}D$_{3/2}$	1.5995	248
1.6122	335	309	5	† HI Br13	1.6109	238
1.6422	256	220	10	† HI Br12	1.6407	274
1.6446	3247	3244	46	†[Fe II] a^{4}F$_{9/2}$-a^{4}D$_{7/2}$	1.6435	191

Broad component. See text for comments.

λ_{obs} (μm)	σ_{obs} (km s^{-1})	σ_{deconv} (km s^{-1})	Flux	Identification	λ_{air} (μm)	v_{obs} (km s^{-1})
1.6450	219	176	55	†[Fe II] a^{4}F$_{9/2}$-a^{4}D$_{7/2}$	1.6435	268

This component sits on top of the broad component (previous line).

λ_{obs} (μm)	σ_{obs} (km s^{-1})	σ_{deconv} (km s^{-1})	Flux	Identification	λ_{air} (μm)	v_{obs} (km s^{-1})
1.6653	252	216	6	†[Fe II] a^{4}F$_{5/2}$-a^{4}D$_{1/2}$	1.6638	271
1.6785	250	214	11	†[Fe II] a^{4}F$_{7/2}$-a^{4}D$_{5/2}$	1.6769	277
1.6821	285	254	14	† HI Br11	1.6807	246
1.7017	282	250	15	†HeI 3p^{3}P^0-4d^{3}D	1.7002	270
1.7123	333	306	4	†[Fe II] a^{4}F$_{5/2}$-a^{4}D$_{3/2}$	1.7111	214
1.7374	311	282	17	† HI Br10	1.7362	210
1.7461	275	242	3	†[Fe II] a^{4}F$_{3/2}$-a^{4}D$_{1/2}$	1.7449	205

The lines marked with † have been observed previously for this object.

The lines marked with * are new for this object or have a new identification.

Table 4.6: Emission lines of the integrated spectrum (ejecta and circumstellar ring combined within a circular aperture of 1.15") in the K band 2005. The spectral resolution is 86 km s^{-1} in the K band. Errors for the values listed in the table are given either in the text or in Table 3.4. The flux is measured in 10^{-16}erg s^{-1} cm^{-2}. The source for the line identification (NIST) is discussed in the text.

λ_{obs} (μm)	σ_{obs} (km s^{-1})	σ_{deconv} (km s^{-1})	Flux	Identification	λ_{air} (μm)	v$_{obs}$ (km s^{-1})
1.9647	690	684	6	*		
2.0086	224	207	4	†[Fe II] a^{4}P$_{1/2}$-a^{2}P$_{1/2}$	2.0067	278
2.0171	268	254	7	* [Fe II] a^{2}G$_{9/2}$-a^{2}H$_{9/2}$	2.0151	291
2.0478	293	280	8	†[Fe II] a^{4}P$_{5/2}$-a^{2}P$_{3/2}$	2.0460	268
2.0602	291	278	127	†HeI 2s^{1}S-2p^{1}P^0	2.0581	298
2.1143	341	330	7	*HeI 1s3p-1s4s	2.1121	306
2.1349	267	253	4	†[Fe II] a^{4}P$_{3/2}$-a^{2}P$_{3/2}$	2.1328	300
2.1643	1949	1947	7	*		
2.1676	277	263	54	† HI Brγ	2.1655	290
2.1908	720	714	1	†		
2.2070	408	399	2	*NaI 2$p^6$5p − 2$p^6$9s	2.2047	316
2.2205	690	684	3	†		
2.2260	243	227	4	* [Fe II] a^{2}G$_{9/2}$-a^{2}H$_{11/2}$	2.2238	291
2.2452	508	500	3	†[Fe II] a^{4}P$_{1/2}$-a^{2}P$_{3/2}$	2.2436	209
Blend? The line transition probability for [Fe II] does not support this large flux. Furthermore large σ_{deconv}.						
2.2556	600	593	2	†		
2.3236	323	311	3	*OI 2$s^2$2p^3(^{2}D)3s − 2$s^2$2p^3(^{4}S)5f	2.3215	270

The lines marked with † have been observed previously for this object.

The lines marked with * are new for this object or have a new identification.

The lines 2.24-2.32 μm were observed in Meikle et al. (1993) as a blended unidentified feature.
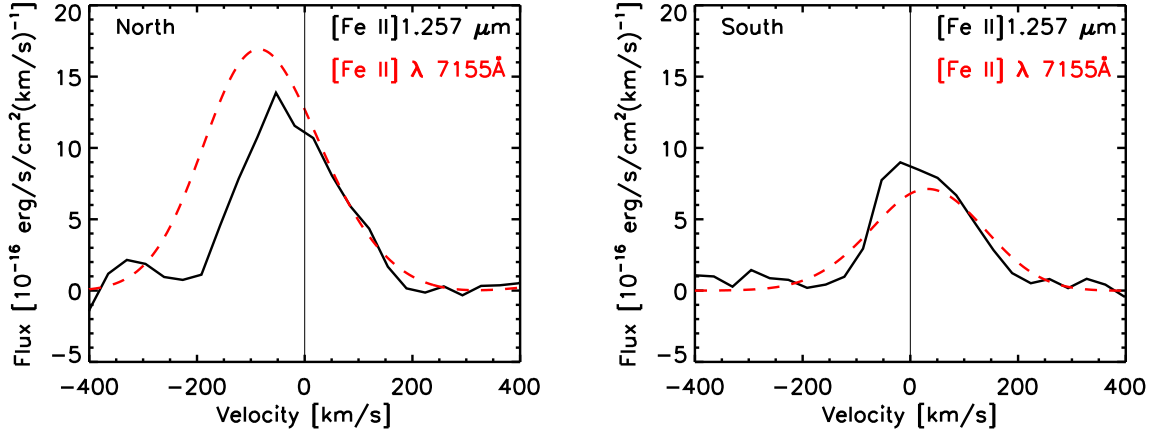
Figure 4.2: North and South extractions from SINFONI J100 of the [Fe II]1.257 μm, where the SINFONI data have been spatially smoothed to the image quality of the UVES observations, and extracted along a position angle (PA=30°) of the UVES observations. The red/dashed curve are North/South extractions from UVES of the [Fe II]7155 Å line reduced to the spectral resolution of SINFONI scaled up a factor 100.

$(1-2) \times 10^{-17} \mathrm{ergs}^{-1}\mathrm{cm}^{-2}\mathrm{\AA}^{-1}$. The continuum flux emission is systematic weaker in the second epoch, where the total exposure time is longer and thus where the signal to noise ratio is larger. This leads us to conclude that at least a part of the emission in 2004 was due to a systematic offset, perhaps coming from the removal of skylines. The remaining continuum in the 2005 epoch could still be real although the origin remains unclear. The continuum emission could come from large scale emission in the region, or perhaps emerge from the ring system itself as the faint glow from a weak H/He continuum. We tested this hypothesis by making an image map of spectral region in the K band (2005) without any emission lines (2.27-2.30 μm), see Figure 4.4. We see clearly in this figure, that there is emission coming from the ring, and vaguely from the interior, at these wavelengths. This supports the argument for the continuum being real and most likely to originate from the shocks.

4.3 Spectral Comparison

From the spectra we see that there are a number of changes between the two epochs. We compare the two epochs in Figure 4.5. There is a lot of very bright skylines in the J band, which caused especially the 2004 epoch to be very noisy. In the newer epoch (2005) the noise reduction has been improved, which can be seen in the top panel of Figure 4.5. We also separate the bright lines better in the 2005 J-band data-set because of a higher wavelength resolution, and/or the sampling resulted in a spectral dithering.

Changes of the emission lines

In the J-band the first three lines (from 2005) in Table 4.3 are new, the first possibly being a MgII line previously observed in Meikle et al. (1993), the other two which could not be identified with
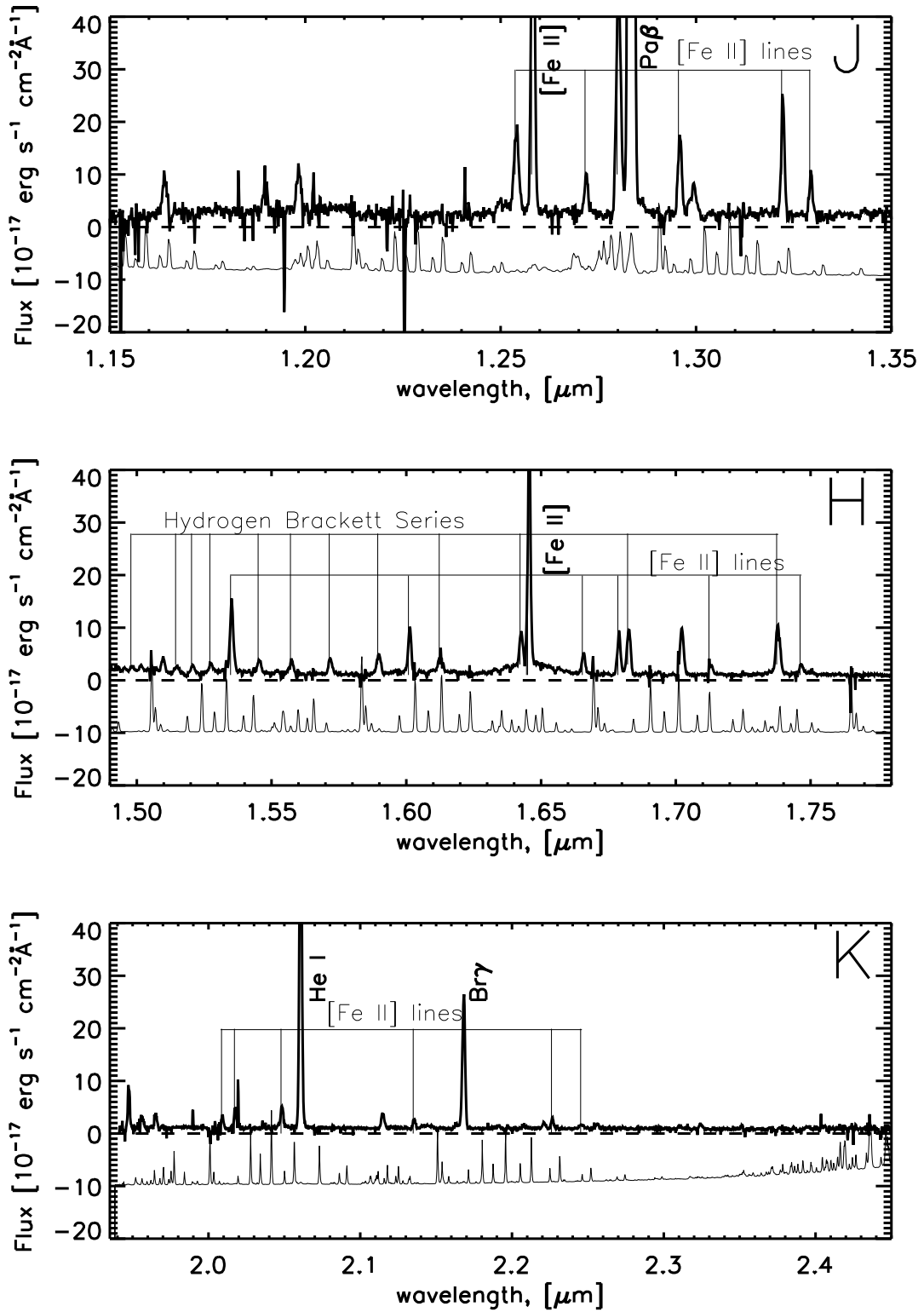
Figure 4.3: The integrated spectrum of the ring and the ejecta in 2005. The sky spectrum is shown offset below the SN ring spectrum. Note that the flux of the sky spectrum has been scaled down to make the spectrum fit in the same figure as the object. The line identifications are given in Table 4.4-4.6.
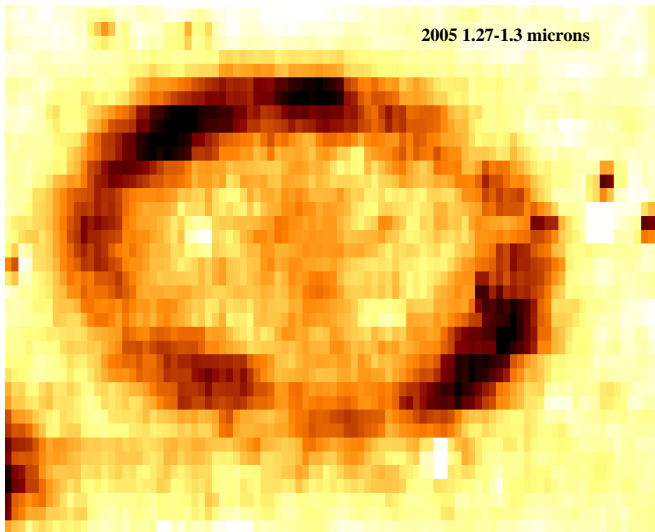
Figure 4.4: An image map of the region 2.27-2.3 μm in the K band (2005)

any of the expected elements. These were not seen in the 2004 epoch since the noise caused us to look at a narrower wavelength range.

Also in the J-band we note that the NI line at 1.3065 μm from 2004 is missing in the 2005 observations and instead we see a new line at 1.2990 μm. The reason that we do not identify this line as the NI line (with λ_0=1.3052 μm) is that the line would have to be blue shifted with 1425 km s^{-1}.

In the H-band we see two new faint lines in the 2005 epoch at 1.4951 μm and 1.5012 μm.

In the K band spectrum we detect in the 2005 epoch also a line at 1.9464 μm (possibly either Fe X or Na I, at red-shifts of 339 km s^{-1}, 321 km s^{-1} respectively). It could be interesting if this line is the Fe X line, because that would provide us with a way to directly compare with the coronal lines observed by Gröningsson et al. (2006) in the UV and thus connect it with the soft X-rays, (see chapter 1 for more details on the coronal lines). However, on closer inspection of the data cube we could see, that the line falls just on the edge of the detector, so it is really only observed in some of the image slices. We have not listed the flux measured for this line since the value would be inaccurate. There is also a new line 1.9647 μm, which we could not be identified using the range of elements we would expect. At 2.143 μm in the K band spectrum there is a line with an unusual shape. In the cube we could assign this emission to a whole line of very bright pixels and thus not originating in the system, therefore we ignore this instrumental artefact. Another emission line which stands out is the very broad line at 2.1643 μm not detected in the 2004 epoch. In the cube it looks like the emission is situated mainly in the ring.

We also have a firm detection of 3 unidentified lines at 2.1907 μm, 2.2205 μm, and 2.2557 μm, which were also observed in 2004 and previous infrared observations (Meikle et al. 1993). The lines share a FWHM larger than the other lines but still smaller than the broad component.

In the 2004 we observed a NiII line at 2.3103 μm, which we did not see in the new epoch. Either what caused the emission has faded in the year in between or the line was not a secure detection in the first place.

49
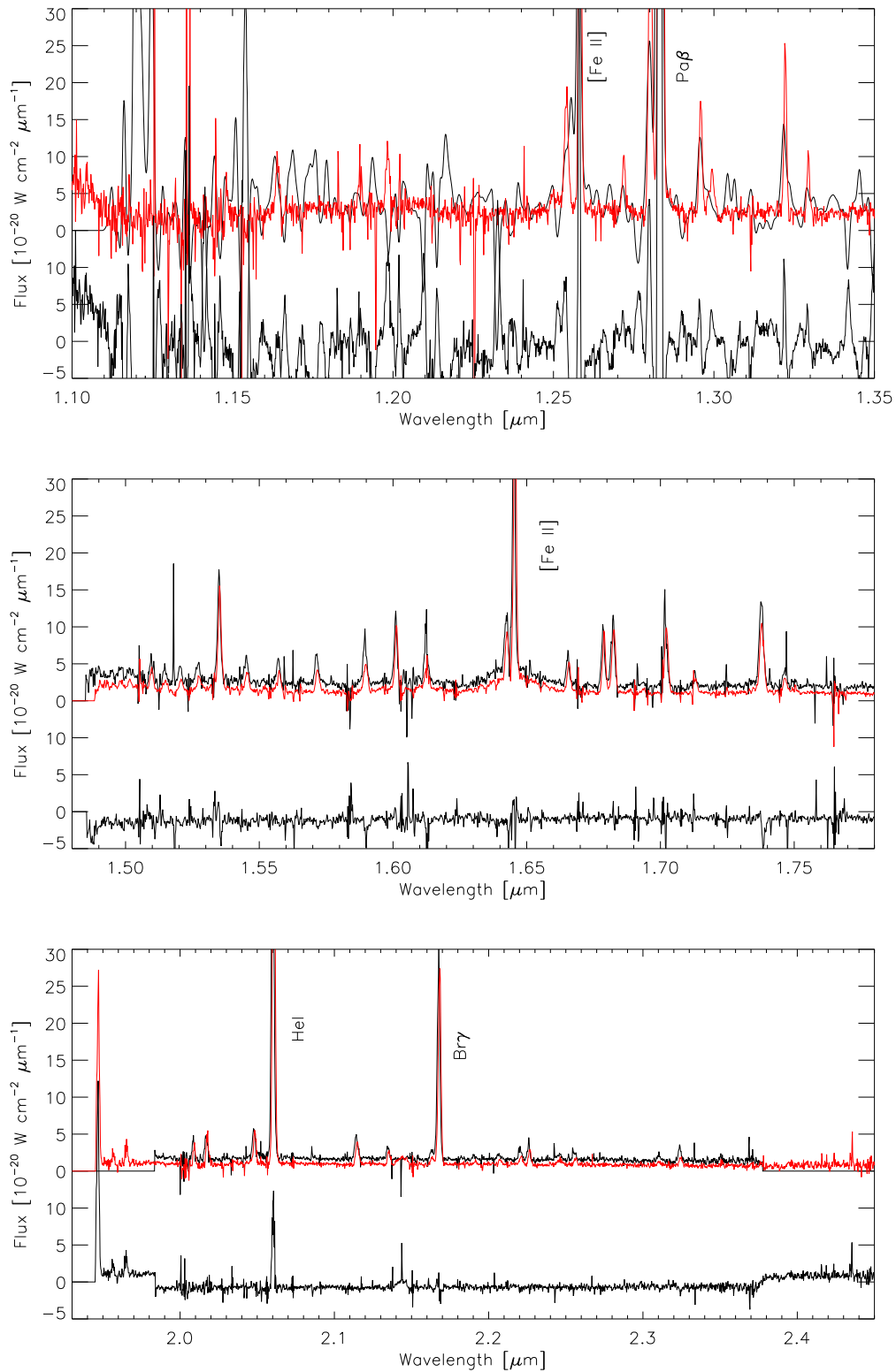
Figure 4.5: The integrated spectrum of the ring and the ejecta. The black curve is the 2004 spectrum and the red line is the 2005 spectrum. The difference between the two years (2005-2004) is shown below.

Two important notes on the velocities measured

First of all the velocities measured are from a Gaussian fit to the line shapes. As noted in chapter 2 the instrument causes a distortion of the line profile, which we cannot correct for. The distortion changes with wavelength as well as with the chosen plate scale. This means that the distortion is not the same for the two epochs. The distortion causes the line profiles to be skewed to either side or having ripples in the peak position, or both. The velocities derived from a Gaussian fit might have been affected by this, which would explain the differences in velocities on a smaller scale.

The data have been reduced using the pipeline for the instrument. We have uncovered a flaw in the interpretation of the wavelength calibration, in that the wavelength solution is made in real numbers, that then has to be translated into integer values in the data-cube. This rounding error has now been identified and the coming versions of the pipeline will have dealt with this problem. We used the OH lines to calibrate the wavelength solution and subsequently corrected it, but this didn't save us from the fact that the pipeline made the rounding error anew when spectra was extracted.
Since it is a rounding error we cannot securely say which of the epochs that is best calibrated. The error is of the order of 1 pixel or less, which corresponds to a systematic offset of 35 km s^{-1} or less. This systematic offset is visible even in the spectra plotted in Figure 4.5, where the emission lines look offset with respect to each other.

The flux differences

We can also in the figure see that the continuum level is lower in the 2005 suggesting that this continuum is just insufficient noise reduction. The wavelength range has been extended in the 2005 epoch, since there was less instrumental defects causing us to cut the spectrum short.
In Table 4.7 we list the flux ratio for chosen emission lines for the two years. Especially in the J band we observe a change in flux for several emission lines. This can either be understood from the significant reduction in noise from year 2004 to year 2005 or be a change in the local extinction properties in the ring, or be caused by changes in the emission due to the shock interaction. The first explanation seems the obvious one since we have more total integration time in the 2005 epoch improving the signal to noise ratio significantly. This is especially seen in the J band, which lies in a notoriously noisy wavelength region. However we cannot exclude the object also causing a change in the flux.
We also observe a change in the Paβ flux. This change could also be caused by the noisy IR sky in the J band, since there is a particular strong OH line at this position in the spectrum. This skyline could have caused an underestimation of the flux as the sky removal could have removed some of the signal from the SN emission line.

Table 4.7: The flux changes between 2004 and 2005 for chosen emission lines in the integrated spectrum.

λ_{air} (μm)	Identification	F_{2005}/F_{2004}	Error
1.2521	[Fe II] $^6D_{3/2}$-$^4D_{1/2}$	1.7	0.2
1.2567	[Fe II] $^6D_{9/2}$-$^4D_{7/2}$	1.3	0.2
1.2703	[Fe II] $^6D_{1/2}$-$^4D_{1/2}$	1.0	0.1
1.2788	[Fe II] $^6D_{3/2}$-$^4D_{3/2}$	1.5	0.2
1.2818	HI Paβ	1.6	0.2
1.2943	[Fe II] $^6D_{5/2}$-$^4D_{5/2}$	1.0	0.1
1.3206	[Fe II] $^6D_{7/2}$-$^4D_{7/2}$	1.0	0.1
1.3278	[Fe II] $^6D_{3/2}$-$^4D_{5/2}$	1.1	0.2
1.5335	[Fe II] $^4F_{9/2}$-$^4D_{5/2}$	1.1	0.2
1.5995	[Fe II] $^4F_{7/2}$-$^4D_{3/2}$	1.1	0.2
1.6435	[Fe II] $^4F_{9/2}$-$^4D_{7/2}$	1.0	0.1
1.6638	[Fe II] $^4F_{5/2}$-$^4D_{1/2}$	1.	0.1
1.6769	[Fe II] $^4F_{7/2}$-$^4D_{5/2}$	0.9	0.1
1.7111	[Fe II] $^4F_{5/2}$-$^4D_{3/2}$	1.3	0.2
1.7449	[Fe II] $^4F_{3/2}$-$^4D_{1/2}$	0.5	0.1
2.0067	[Fe II] $^4P_{1/2}$-$^2P_{1/2}$	0.8	0.1
2.0151	[Fe II] $^2G_{9/2}$-$^2H_{9/2}$	0.9	0.2
2.0460	[Fe II] $^4P_{5/2}$-$^2P_{3/2}$	1.	0.1
2.0581	HeI 2s^{1}S-2p^{1}P^0	1.2	0.2
2.1328	[Fe II] $^4P_{3/2}$-$^2P_{3/2}$	1.3	0.2
2.1655	HI Brγ	0.9	0.1
2.2238	[Fe II] $^2G_{9/2}$-$^2H_{11/2}$	0.8	0.1
2.2436	[Fe II] $^4P_{1/2}$-$^2P_{3/2}$	0.75	0.1

Chapter 5

The Inner Circumstellar Ring

The emission lines from the circumstellar ring are a complex combination of different emission sites. With the shock moving into the ring material an outward acceleration of the shocked material is expected, and hence a difference in the projected radial velocity shift around the ring should be observed. However, Michael et al. (2000) and Pun et al. (2002) showed that there are oblique shocks along the protrusions, and the velocity field is a combination of material accelerated not only radially forward, see Figure 5.1. The infrared lines discussed in this chapter are from the intermediate component with line widths of $\sim$ 200-300 km s^{-1} and they originate from the shocked gas propagating outwards from the supernova centre behind the forward shock front.
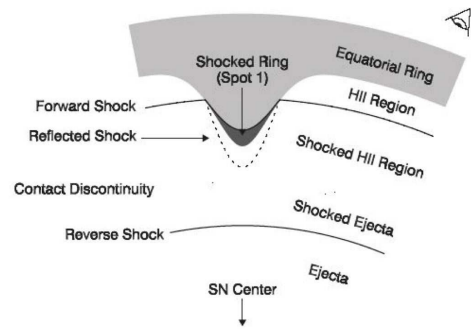
Figure 5.1: Shock model of Spot 1 from Pun et al. (2002).

5.1 Epoch 2004

The SINFONI data cube can be used to explore the velocity structure of the ring. We assigned an azimuthal angle for each position on the ring, defining North as zero degrees, and increasing the angle through East. The resolution in angle is then set by the spatial resolution. For each angle we coadded a spectrum with the angular position as the centre and the radius of the order of the image quality. In this sampling two neighbouring extracted spectra therefore have many spaxels in common and are correlated (cf. Fig. 5.2). The radius of the extraction circle was 3 spaxels for the 250 mas resolution (radius of 0.375") and 5 spaxels for the 100 mas resolution (radius of 0.25"). We have here chosen the radius to be of the order of the image quality listed in Table 3.1, for the different observations. The left panel of Figure 5.2 shows the extracted spectrum (J100-band between 1.25μm-1.29μm) for different positions on the circumstellar ring and the right panel shows the sizes of the extractions and their corresponding position angles.
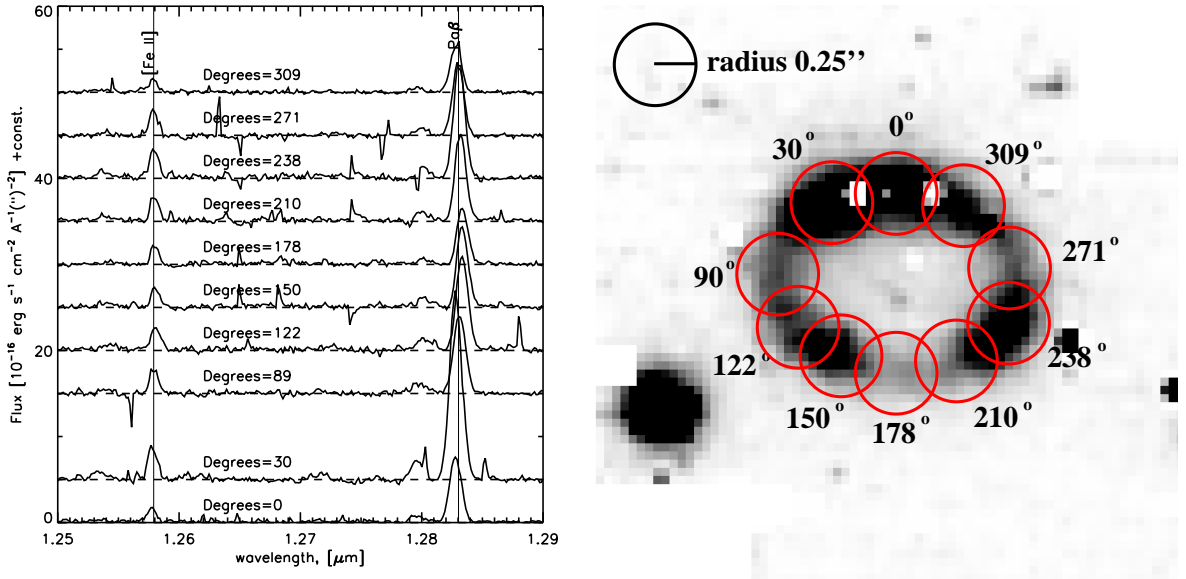
Figure 5.2: Left: Extraction of spectra from the reduced data cube close to the [Fe II] 1.257 μm and Paβ lines in the J100 band. The spectra are plotted with a vertical offset. The vertical lines through the spectra mark the positions of the systemic velocity of 286.5 km s^{-1} for the different lines. Right: The size of the extractions and the corresponding position angles in the J100 band.

It is clear that the position of the peak of [Fe II] 1.257 μm and the peak of Paβ change for the different extractions.

Figure 5.3 shows the radial velocity shift for the Paβ, Brγ, HeI, and [Fe II]1.257μm lines, plotted *vs.* the position angle (PA). We have here chosen the extraction radii for the J100 extractions to be similar to that of K250 (radius=7 spaxels $\sim$ 0.35"). The error bars in velocity are calculated from the uncertainty in the determination of the wavelength and the error bars in angle display the size of the extraction radius for the spectra. The error bars in angle are plotted conservatively to indicate the extent of contamination between adjacent spaxels. Only extractions with a distance of more than twice the integration radius are truly independent of each other. For J, H, and K the radius was 3 spaxels, which corresponds to a separation of 6 spaxels (0.75"), and 14 spaxels for J100 (0.7").

The emission lines in Fig. 5.3 are all dominated by the intermediate component, coming from the shocked ring material. This is clear from the fact that the velocity of the lines differs by a large factor from the expansion velocity of the narrow lines, $\sim$ 10 km s^{-1}. It is evident from this figure that the line centres of the northern part of the ring are blue shifted, while the southern part is red shifted. This is as expected for an expanding circular ring with the Northern part tilted towards us. From HST imaging Panagia et al. (1991) find an inclination angle i=42.$^\circ$8 $\pm$ 2.$^\circ$6 with respect to the plane of the sky (see also Sugerman et al. 2005). The theoretical line of sight velocity, v_r, for a circular ring, uniformly expanding with velocity v_{exp}, and tilted with respect to the plane of the sky with the angle i, is

$$v_r(\psi) = v_{exp} \sin i \cos(\psi + \phi) + v_{SN} . \tag{5.1}$$

54
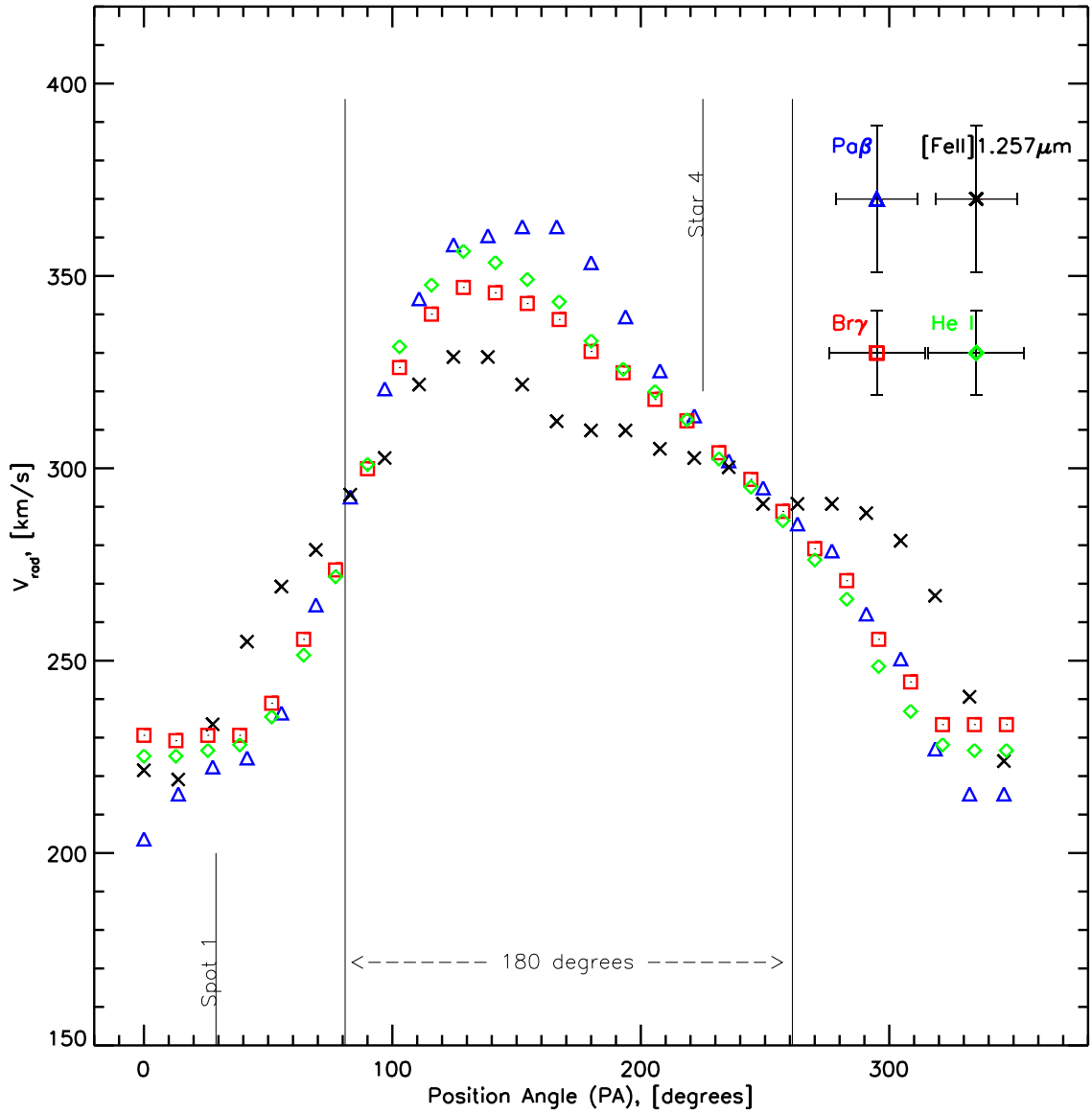
Figure 5.3: Radial velocity shift for different angular positions around the ring for the strongest emission lines. The angle increases from North to East. The location of Spot 1 and Star 4 are indicated. The J100 data has been sampled with 7 px radius in order to have a similar extraction radius as the 250 obs. The error-bars are indicated in the top right corner.

Here ψ is the azimuthal angle of the ring segment, defined with $\psi = 0$ for North. The phase shift, ϕ, is introduced to account for the offset of the major axis of the ring from the East-West direction and can be interpreted as a rotation of the ring out of the plane of the sky. The azimuthal angle, ψ, in the ring is related to the position angle, PA:

$$\tan \psi = \tan (PA) \cdot \sin i \qquad (5.2)$$

The observed velocity shift at a given angle is a complex convolution of the individual shock velocities at this point and the geometry. A simple model of the line profile of an individual spot was given in Pun et al. (2002), see Figure 5.1. The key point of this model is that the shock velocity is likely to vary along the surface of the hot spot depending on the angle between the surface and the impacting blast wave. The highest velocities are therefore expected for a head on collision, while the tangential impacts result in lower shock velocities. Furthermore, the gas velocity, in the reference system of the shock, decreases behind the shock as the gas cools. For the observer at rest, the hot gas velocity behind the shock is $3V_s/4$, while that of the radiatively cooled gas is V_s. The peak velocity at a given angle therefore depends on the shock velocity which dominates the contribution to a given line. It is therefore important to realise that the peak velocity we measure is only a weighted average of the emissivity of a given line. This is then modified by the angle of the gas velocity to the line of sight.

This can clearly be seen in the VLT/UVES observations, which provide line profiles with much higher spectral, but lower spatial resolution (Gröningsson et al. 2006, 2007). The line profile of e.g., the Hydrogen Balmer and He I lines from the northern part of the ring, including Spot 1, has a peak at ~ 200 km s^{-1} in November 2005. This agrees well with that measured at the position of Spot 1 in our observations, $\sim 223 \pm 7$ km s^{-1} (combining Paβ, Brγ and HeI 2.058 μm). The Hα line in the UVES observations, however, extends out to ~ -450 km s^{-1}, seen only as a faint wing. While the UVES observations provide us with a good representation of the emission as function of velocity, the SINFONI observations measures the variation of the average velocity for each line along the ring. This illustrates well the complementarity of the SINFONI and UVES observations.

It is clear from Fig. 5.3 that the measured velocities do not follow the simple cosine as predicted by the Eq. (5.1). A simplistic way to derive the bulk velocity of the material, i.e. the centre of rest for the ring, would be to determine the 'nodal' points ($\psi = 90°$ and $\psi = 270°$), where the expansion velocity is orthogonal to the line of sight. Inspection of Fig. 5.3 immediately shows that the two velocities are not identical at these angles for the various lines. We find that for Paβ, Brγ and HeI $v_r(90°) = (300 \pm 7)$ km s^{-1} and $v_r(270°) = (275 \pm 3)$ km s^{-1}. For a perfect circular ring tilted out of the plane of the sky the radial velocity should vanish at points exactly 180° apart and these points indicate the bulk velocity of the material. We have marked the two points where this happens in Fig. 5.3. The mean bulk velocity is measured at a slightly different angle $\psi + \phi = 81° \pm 9°$ and $\psi + \phi = 261° \pm 8°$ with a bulk velocity of (280 ± 7) km s^{-1}. This means that the offset angle is $\phi = -9° \pm 7°$. This position of the major axis agrees well with that found by Sugerman et al. (2005) (PA= $81.°1 \pm 0.°8$) using imaging of light echoes and modelling the shape of all the matter around the supernova. Based on images of the ring alone this rotation of the major axis has been found previously by (Burrows et al. 1995; Plait et al. 1995; Sugerman et al. 2002). Our determination is not weighted by intensity and rather than

having single points we make a dynamical map of the whole ring. The influence of the different hot spots or the contamination by Star 4, which is directly superposed onto the inner stellar ring, appear negligible. We have marked the location of Spot 1 and Star 4 in the diagram and there are no clear deviations from the overall behaviour at these two points. The derived velocity of the ring of (280 ± 7) km s^{-1} agrees with other results of 286.5 km s^{-1} (Gröningsson et al. 2007; Meaburn et al. 1995; Crotts et al. 1995; Cumming & Meikle 1993).

Another result concerns velocity of the shocked ring material after passage of the shock. As we discussed above, the peak velocity is a function of the geometry of each shocked spot, as well as the direction of the ring plane to the line of sight. We can, however, use the geometric information above to find the de-projected, average shock velocity around the ring. Assuming an inclination angle of $i = 42°.8$, and a systemic velocity of 286.5 km s^{-1} we have calculated the expansion velocity and binned the data-points in Fig. 5.4. We derive from this a mean velocity around 90 km s^{-1}.

We can also investigate the maximum velocities on the Northern and Southern sides and see how they compare with the systemic velocity shift found for the system. The maximum velocity is 362 km s^{-1} at around PA=160° (South) and the minimum velocity measured for the system is 203 km s^{-1} at around PA=0° (North). The natural average value of those two velocities is 282.5 km s^{-1}, which coincidentally is very close to the systemic velocity for the system, (280 ± 7) km s^{-1}. This implies that the velocities are symmetric around the systematic shift of the system. Both of the extremum values were measured for the Paβ line, which can be explained by the smaller extraction sizes that allows the average velocity value to be of smaller regions. The larger extraction sizes average over larger regions and that can wash out extremum points.

Figure 5.5 shows the flux of the [Fe II] λ 1.257 μm, the HeI, and the Brγ lines plotted vs. the azimuthal angle. We see here that the H and He lines, as expected, follow each other, and that the ratio He/H is fairly uniform around the ring. While the narrow (intermediate) [Fe II] line flux follows the HeI flux level between 100° and 200° its flux increase around Spot 1 peaks at a different angle. This difference can be understood from the fact that while the H and He lines arise in an ionised region at $\sim 10,000$ K, the [Fe II] lines arise at ~ 5000 K, behind the ionised zone. The extent of this photoionized zone, and therefore the [Fe II] flux, depends on the shock velocity. In addition, collisional de-excitation is important for the [Fe II] lines, while the H and He lines are less sensitive to the density, being dominated by recombination. The ratio of the [Fe II], H and He lines will therefore depend on both the shock velocity and density, which are both likely to vary along the ring. Because $V_s \approx V_{\text{blast}}(\rho_0/\rho_{\text{blob}})^{1/2}$ the shock velocity into the cloud depends on the cloud density, ρ_{blob}. Finally, if the ratio of the narrow and intermediate components vary between the different lines this may result in different peak velocities.

We expect the flux of H and He to increase around the ring as the hot spots evolve.

The strength of the SINFONI observations is that we can extract the FWHM of the lines at spatially different positions. The FWHM is of the order of $\sim$ 200-250 km s^{-1} all over the ring for the lines discussed, which means they belong to the intermediate velocity component and therefore comes from the shocked cooling gas.
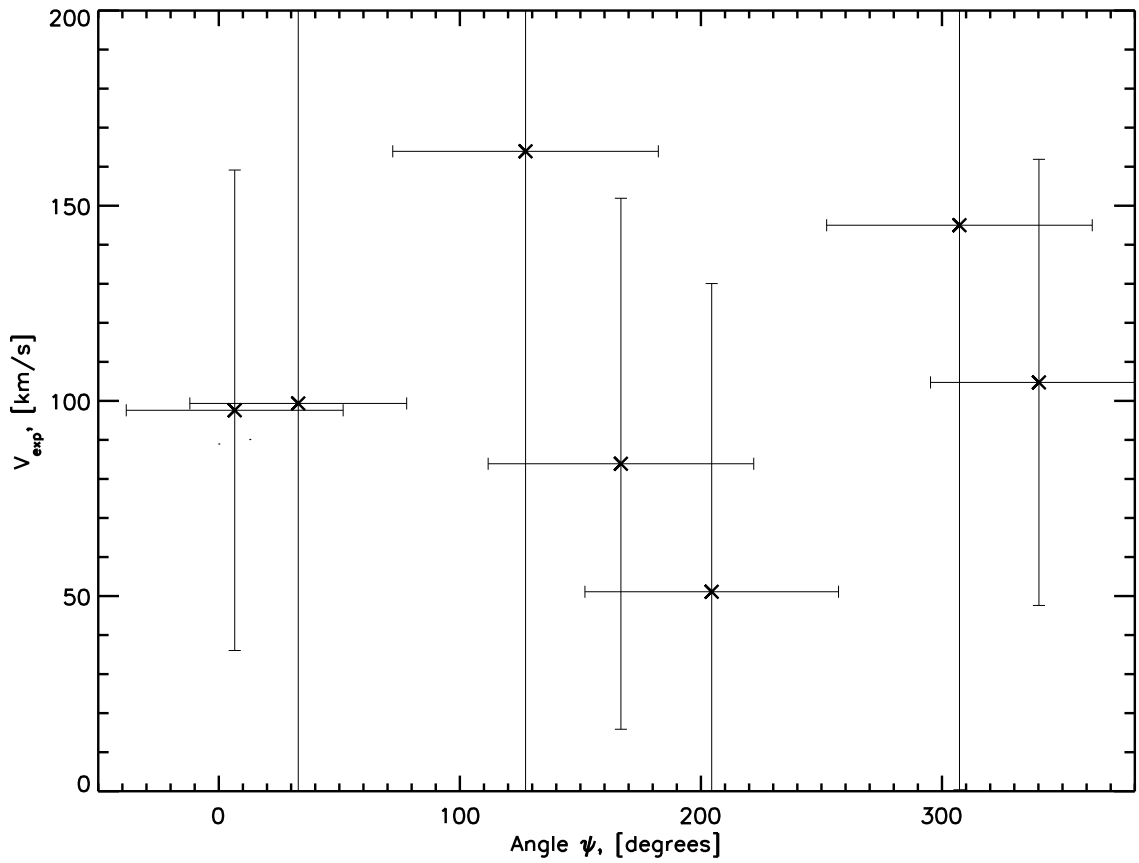
Figure 5.4: De-projected velocity vs. angle for Paβ, Brγ and He I. 0 degrees is North, the angle increases from North to East. In the de-projection we assumed a systemic velocity of 286.5 km s^{-1}, and an inclination angle of $i = 42°.8$.
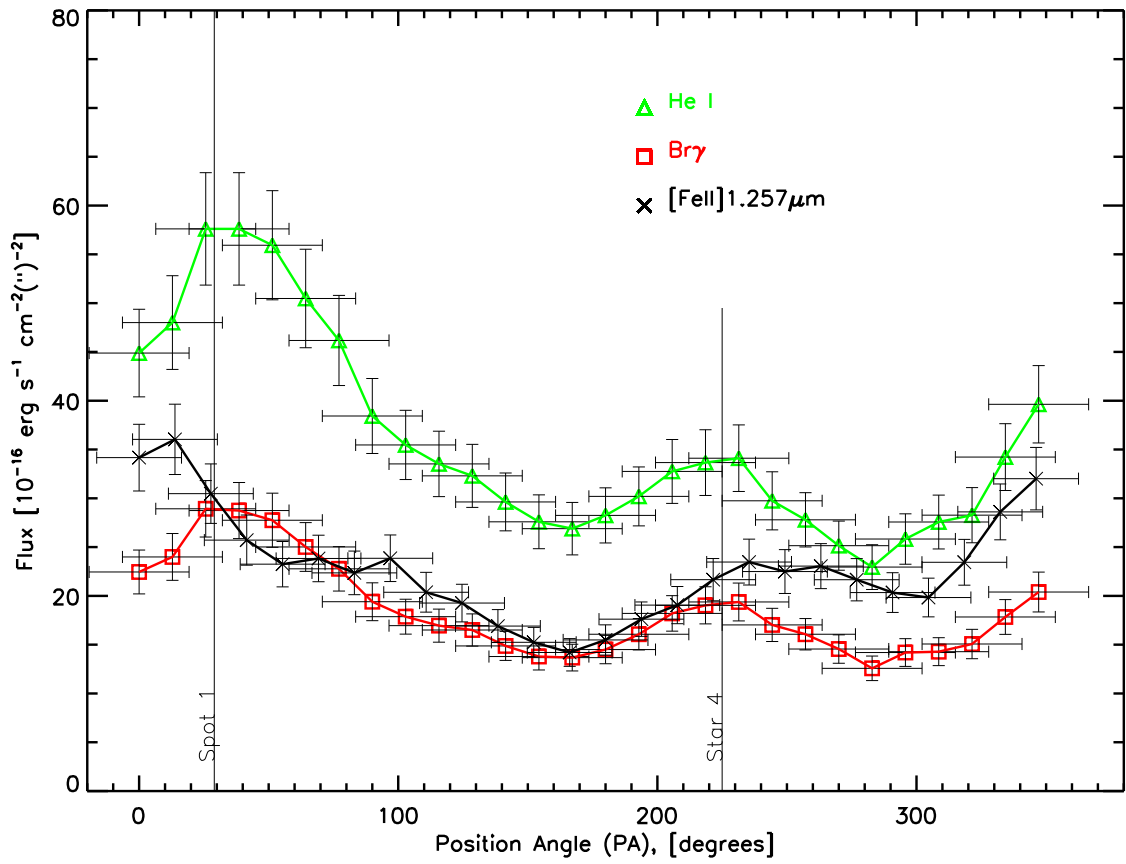
Figure 5.5: Flux variations for different angular positions around the ring. The aperture area is $A=\pi*(0.375'')^2$ for the H and He lines, and $A=\pi*(0.35'')^2$ for the [Fe II] line.

5.2 Epoch 2005

As for the 2004 epoch the error for the angle in the ring extractions is calculated as the radius of the extraction in pixels divided by the total circumference of the ring in pixels. This error then reflects the area of the extraction. Since the majority of the flux in an extraction could come from any of the spaxels in the extraction area, the radius of the extraction can be used as a measure of the error of the position. The extractions are overlapping so neighbouring extractions are most often correlated. Besides the oversampling we also have to keep in mind that the geometry of the system is circular, and extractions can be associated even though they are not neighbouring, because the actual distance between them can be shorter than the distance on the ring. The errors only take the distance on the ring into account and not the actual distance.

We again start the analysis with some geometrical considerations. Figure 5.6 shows the radial velocity vs. the position angle (PA) for the brightest emission lines. We repeated the measurement of the 'nodal' points of the ring ($\psi = 90°$ and $\psi = 270°$). We find that for Paβ, Brγ and HeI $v_r(90°) = (332 \pm 2)$ km s^{-1} and $v_r(270°) = (290 \pm 2)$ km s^{-1}. Which confirms our result from the 2004 epoch that the material at PA=90° is more red-shifted and the material at PA=270° is more blue shifted. We find for this epoch that the mean bulk velocity is measured at $\psi + \phi = 70° \pm 8°$ and $\psi + \phi = 250° \pm 8°$ with a bulk velocity of (295 ± 2) km s^{-1}. This gives an offset angle of $\phi = -20° \pm 8°$.
The fact that the rest-velocity for the system from the 2005 epoch is larger than in the 2004 epoch can be explained by systematic velocity errors, where the 2004 data set is giving an overall lower value for the velocities, and the 2005 epoch giving an overall larger velocity. This could be due to the systematic error in the wavelength calibration mentioned in chapter 4.

When we inspect Figure 5.6, which shows the radial velocity vs. position angle for epoch 2005, we see that the scatter around PA=250° − 280° is much larger than on the Eastern side (PA ∼ 90°). This scatter could have caused us to find a different offset angle, since we locate this point by inspecting the velocity curve and finding positions with similar velocity 180° apart on the ring.
Looking at the radial velocity curve we see that the [Fe II] line does not have the same shape as the He and H lines. In fact, if we find the positions on the [Fe II] curve, which have the same velocity 180 degrees apart, we find this position to be at $82° \pm 18°$ (and 262°), closer to the 2004 value, and with a velocity of 302 ± 3 km s^{-1}. The error on the angle here being rather large, because we only have one point. In all, this means that the velocities for the systematic shift, we find this way, are larger than for the 2004 epoch.

We can also investigate the maximum velocities on the Northern and Southern sides and see how they compare with the systemic velocity shift found for the system. The maximum velocity is 397 km s^{-1} at around PA=180° (South) and the minimum velocity measured for the system is 225 km s^{-1} at around PA=0° (North). The natural average value of those two velocities is 311 km s^{-1}, which is larger than the systemic velocity for the system, (295 ± 2) km s^{-1}. The extremum value in the South was measured for the He I line and the Northern for the Brγ line. This implies that the Southern side has more red-shifted velocities than the Northern side is blue shifted. This can possibly be an effect of the difference in viewing angle at the shock
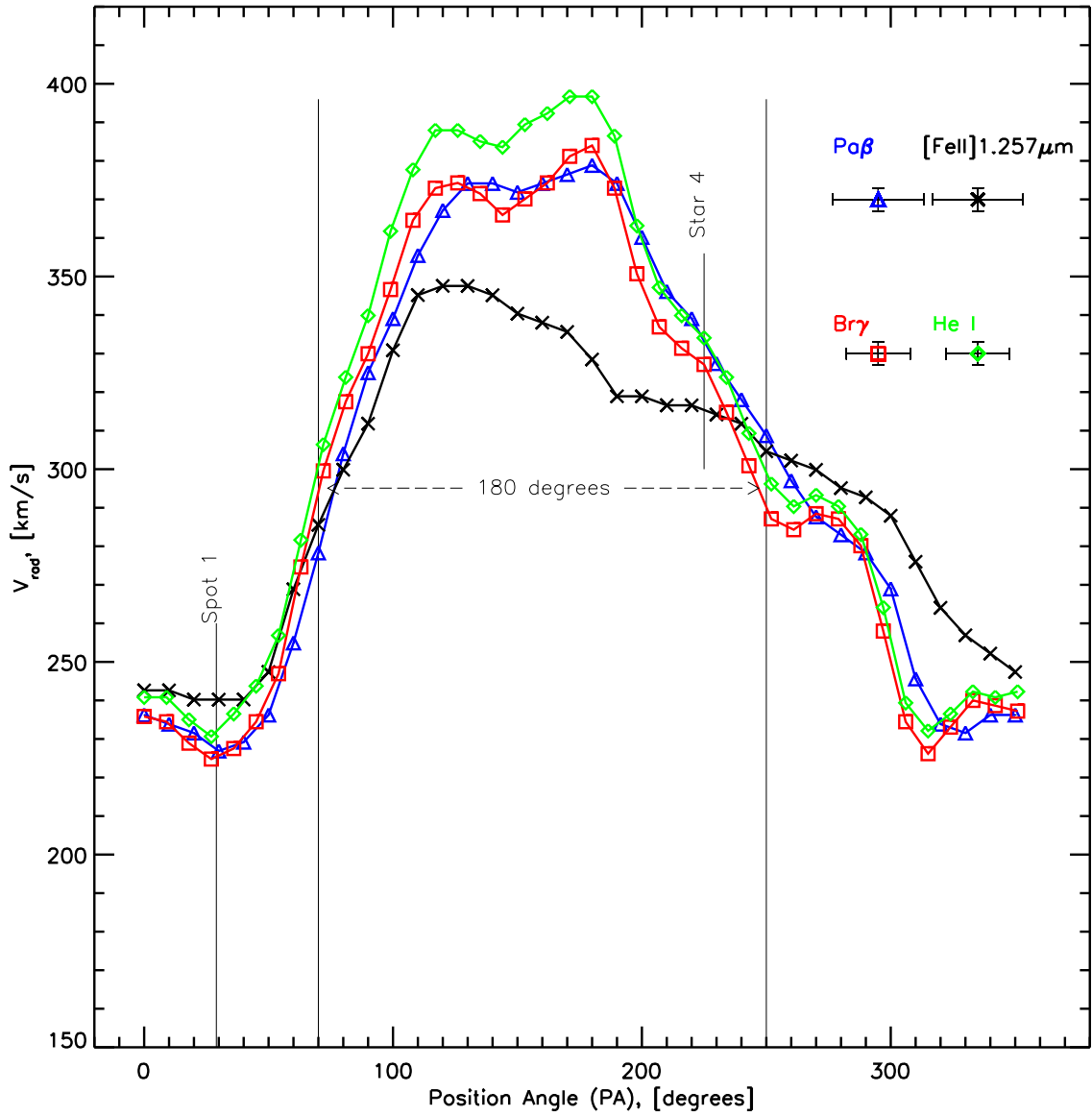
Figure 5.6: Radial velocity shift for different angular positions around the ring for the strongest emission lines (2005 epoch). The angle increases from North to East. The location of Spot 1 and Star 4 are indicated. The aperture radius is r=0.275"/2 for the Brγ and He lines, and r=0.375"/2 for the [Fe II] line and the Paβ. The error-bars are indicated in the top right corner.
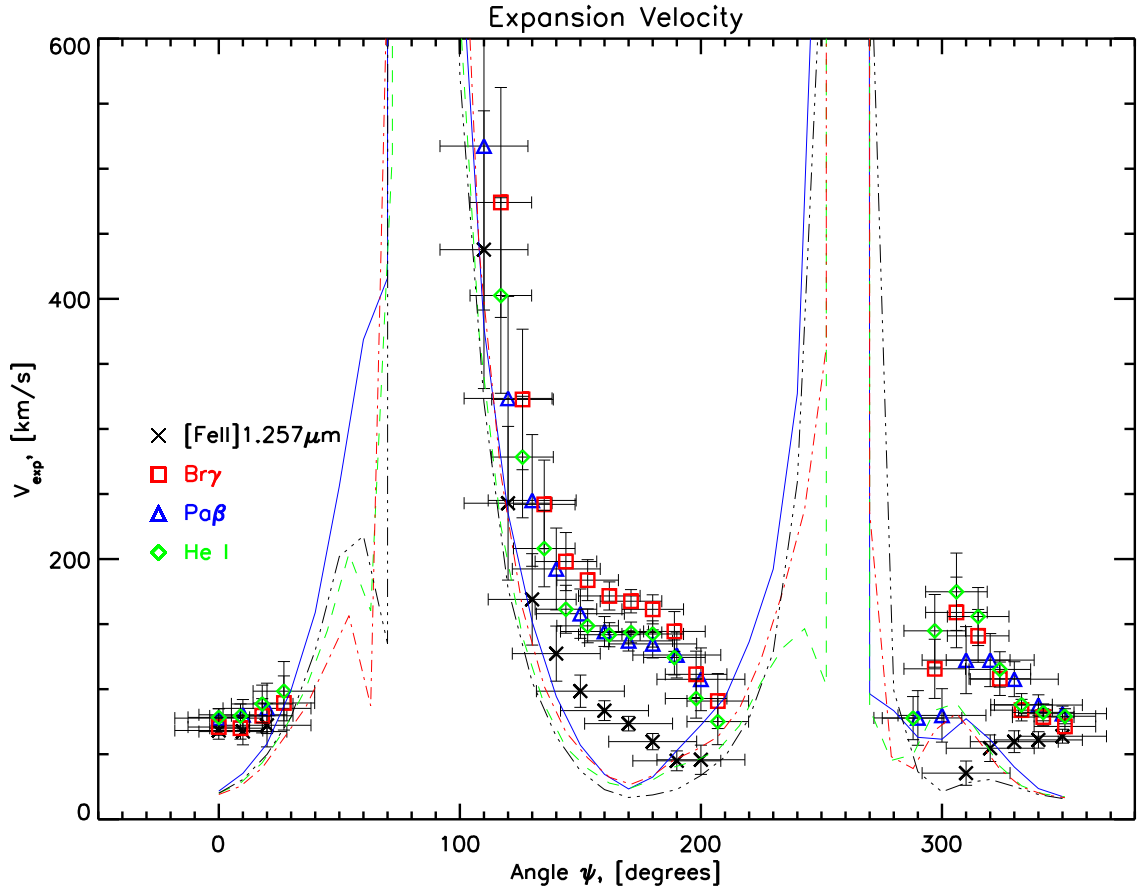
Figure 5.7: De-projected velocity vs. angle for Paβ, Brγ, HeI and [Fe II]. 0 degrees is North, the angle increases from North to East. The curves represent the 3 sigma propagated errors (assuming they are random) for the expansion velocity, so that all points above the curve for the emission line are a 3 times the value of their errors. In the de-projection we assumed a systemic velocity of 286.5 km s^{-1} and an inclination angle of $i = 42°.8$. Our errors here are most likely underestimated in that at least the velocity errors probably are systematic.
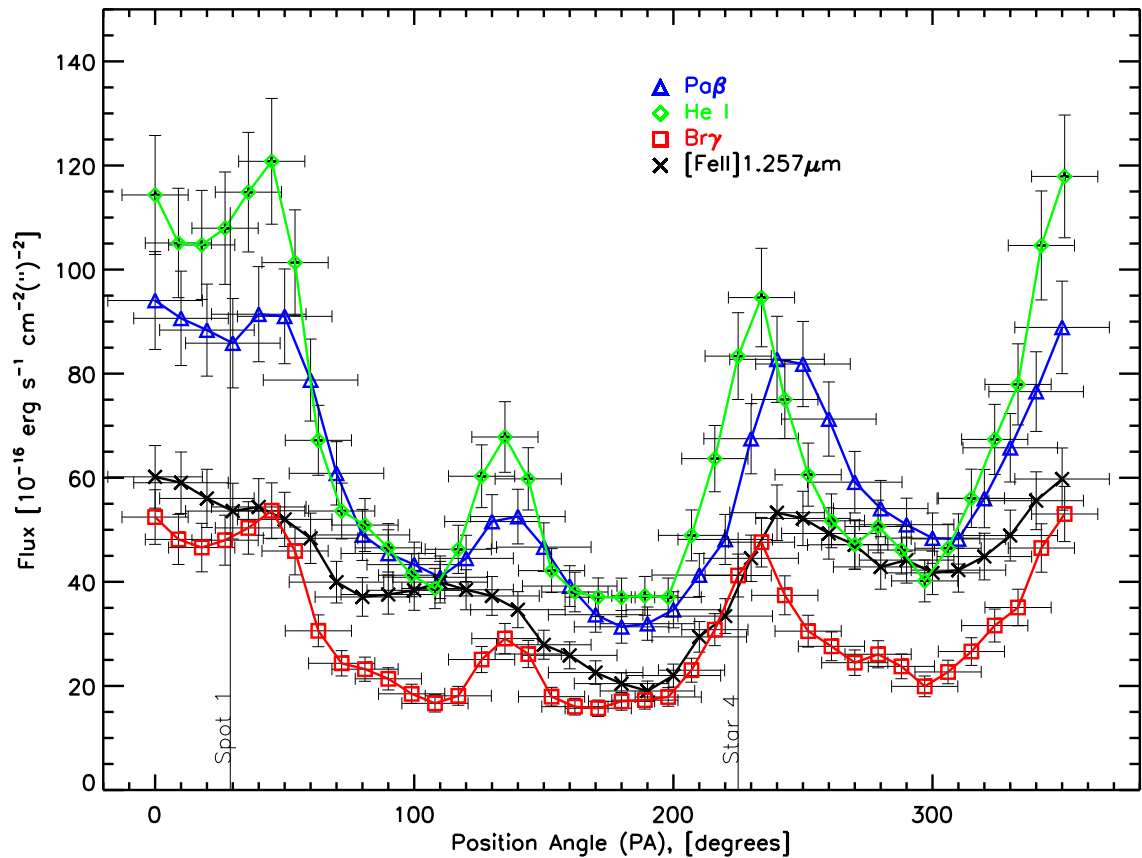
Figure 5.8: Flux variations for different angular positions around the ring for the strongest emission lines. The angle increases from North to East. The location of Spot 1 and Star 4 are indicated. The aperture area is $A=\pi * (0.275''/2)^2$ for the Brγ and He lines, and $A=\pi * (0.375''/2)^2$ for the [Fe II] line and the Paβ. The Paβ flux has been scaled down a factor 4.

sites. The Southern spots are viewed in direction of the shocks, so that the protrusion cannot shield the emission. In the Northern side the protrusions shield some of the emission, since we are viewing the shock *trough* the protrusion that are being hit.

Our higher angular resolution has resulted in us now seeing four bumps on the curve in Figure 5.6, two in the North (0°) and two in the South (180°). These features are not necessarily new, since a larger extraction radius (and worse seeing) would cause us in 2004 to measure velocities averaged over a larger area, and thus possibly smeared out features like this. This sampling effect cannot explain that we for the 2005 epoch see larger velocities at least for the South side.
Since this double bump is apparent both in the North and in the South it must be reflecting a property of the ring and/or the shock.

We also see a larger scatter at 270°, which could be interpreted as a larger velocity, since a larger velocity at a nodal point could be detected as a larger scatter in the observed velocity.
The bumps on the curve would be most pronounced in the South and in the North, because the ring inclination with the plane of the sky enhances the velocities from those parts of the ring. This analysis here cannot show the complete picture of the radial velocities of the spots, since we cannot see the spots in the velocity plot that are too close to the inclination axis of the ring. The radial velocity curves from the two epochs compared will be discussed further in Chapter 5.3.1.

In Figure 5.7 we show the de-projected velocity vs. the angular positions in the ring system, where the velocities are calculated assuming a systemic velocity of 286.5 km s^{-1}. The de-projected velocity could not be calculated for certain regions of the ring (the nodal points), because the functions diverge at those positions yielding unreasonable large or small values. We have in this plot omitted points, where the propagated error was larger than one third of the velocity value itself (thus only plotting 3 sigma detections). For that calculation we propagated the errors assuming they are random and independent, which might not be the case in that we suspect the velocity errors to be systematic. The de-projected velocity (i.e. the expansion velocity in the in plane) is not uniform around the ring. We clearly see a larger expansion velocity at 120°, but this could be due to the calculation in the de-projection. Instead of looking at the values in the boundary of the function space, we look for variations in the curve itself. We clearly see that the expansion velocity at around 307° is larger than for the positions around it. We also see a faint break in the curve around 180°. Variations in the expansion velocity could indicate variations in either the ejecta outflow or in the density of the matter that the shock runs into. We will discuss this in more detail, when we compare the positions found from the velocity with HST images of the ring in section 5.4.

Figure 5.8 shows the flux vs. position angle for the brightest emission lines. The very bright Paβ line has been scaled down by a factor of 4 in order to fit in the same plot. We see four distinct bumps at the positions 43°, 137°, 237°, 355°, which could be related to the hot spots. However, the first and brightest spot 1 (at PA=29°), does not coincide with the peak PA positions. Instead we see that at this position the flux level is generally higher extending over the whole North North Eastern quadrant of the ring. The flux variations around the ring are compared with

epoch 2004 in Chapter 5.3.2.

This gives us in total 6 bumps we can separate around the ring. Four from the flux at 43°, 137°, 237°, 355°, and two from the expansion velocity at 180° and 307°. In the expansion velocity plot (Fig. 5.7) we could not plot the regions PA=60°-130° and PA=230°-280°. If we use the radial velocity plot in Figure 5.6 to recover bumps on the curve, we can add two more bumps to our collection. One at 121° and one at 270°, when we chose to interpret the scatter in radial velocity at 270° as a bump. This gives us a total of 8 bumps. These bumps are listed in Table 5.1 and compared with the HST hot spots in section 5.4.

We would like to emphasise that the outer rings cannot influence the identification of these bumps, because the lines we are deriving the velocities from are intermediate width lines (200-300 km s^{-1}), where the outer lines are only emitting narrow lines. SINFONI cannot resolve these narrow lines, and the line profiles we would observe from them would be of the order of the instrument spectral resolution (75-150 km s^{-1}). Furthermore the outer rings are now so faint that we do not observe them with SINFONI.

5.3   Evolution

For the H and K band we see a large improvement in the resolution from the 2004 epoch to the 2005 epoch with higher spatial resolution and deeper better signal to noise spectra. The error of the J observations are more or less the same between the two years, due to the high spatial resolution observations from 2004.

We have to be careful when we compare the two epochs, since the spatial resolution and thus the extractions were of different sizes. Therefore it is convenient to use aperture free measurements in the comparison. The velocity plots can readily be compared in that the error on the angles reflects the aperture and thus can be taken into account.
We have to be much more careful when we deal with the fluxes measured around the ring, since flux is highly sensitive to aperture. Therefore we have calculated the flux per arseconds^2, scaling out the aperture size and thus the dependence on it. However, this does not prevent contamination from adjacent bins due to the seeing. We saw in Chapter 4 that the background level was different between the two epochs, this will not affect this comparison, because we measure the flux for a line above the continuum level.

5.3.1   Radial Velocity Changes

The left panel of Figure 5.9 shows the velocity curves for the two epochs, where we have shifted the 2004 data up by 20 km s^{-1} in order for the two epochs to be overlapping. In this figure we see that if we accept such a systematic error in velocity between the two epochs, we get that both the velocities in the South and North have increased from the 2004 epoch to the 2005 epoch. The problem here is, that we cannot tell which of the data sets, that are the least influenced by systematic errors (the systematic error in the wavelength calibration is mentioned in chapter 4). The right panel of Figure 5.9 shows the differences between the velocity curves for the two
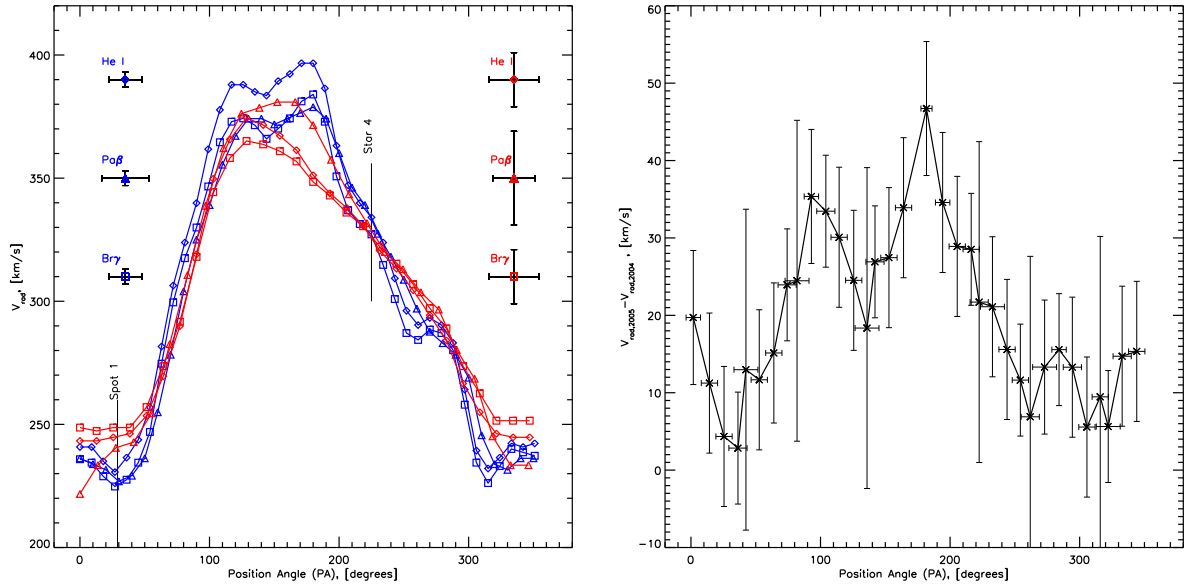
Figure 5.9: Left: The radial velocity shift for the two epochs combined. The red curve is the 2004 epoch and the blue curve is the 2005 epoch. The 2004 epoch has been shifted with +20 km s^{-1}. Error-bars are indicated along the sides. Right: Differences between the radial velocity curves for the two epochs. For more details on the different epochs look in the text or in the captions of Figures 5.3 and 5.6.

epochs, where the curve for one epoch is the average for the Brγ, Paβ and He I lines. Since the sampling interval was different between the two epochs (and the different bands) we have constructed the average radial velocity for individual angle bins (size=10° in PA) for the two epochs and then calculated the difference between them (and propagated the errors accordingly). If the velocity differences (2005-2004) were caused by the systematic error in the wavelength calibration alone, we would expect the points to be offset. However there is only a rather small offset of 2.5 km s^{-1} consistent for all values of PA. This could indicate that either the systematic velocity error is less than we thought, or more random in its influence. If it is random in its influence, then it is not influencing one epoch one way and the other epoch the other way, but rather influencing every extraction in either way, randomly. Assuming that is the case, then we would expect to see a noise pattern, which one could argue we do in the right panel of Figure 5.9, of the order of 10-20 km s^{-1}.

Accepting this as the noise level, then we clearly see a difference between the two epochs in Fig. 5.9, which cannot be attributed only to the difference in spatial resolution or sampling. This difference shows an increase in radial velocity for the ring segment between 65° and 230°, with peaks at 93° ± 6° and 180° ± 5°. The increase in velocity is 35 ±9 km s^{-1} for the 93° peak, and 47 ±9 km s^{-1} for the 180° peak, corresponding to an increase of 12 ± 3 % and 14 ± 3 %, respectively.

One could argue that the peak at 93° could be caused just by the angular binning size and position we chose, because the radial velocity curve is rather steep there. We checked this by adopting a larger binning size of 20°, which still resulted in a peak at this position above the noise level, so we tend to believe that it is real.

There is no physical mechanism to accelerate the already shocked gas component. Rather than interpreting the increase in radial velocity as an acceleration, we think that this could be caused by newly cooled material, that happens to have a larger velocity.

5.3.2 Temporal Flux Variations

One obvious way to compare the emission between the two epochs is to make image maps for different lines and then compare them between the epochs. However, since the H and K band observations in 2004 were with a lower spatial resolution this might not yield more information. Instead we use the extractions and plot the flux vs. angle to see any differences.

Figure 5.10 shows the flux from both epochs for the brightest emission lines, while Figure 5.11 shows the flux ratios for the lines. The sampling interval was different between the two epochs, so the ratios are calculated from the average flux for individual angle bins (size=$20°$ in PA). The angle for one bin is then found as the average of the angles in the bin. The ratios and angles errors are propagated accordingly, assuming random errors. The figure clearly shows several individual spikes at $6° \pm 8°$, $49°$, $129°$, $149°$, $230°$, $247°$, and $346°$. Some of these are found from just one or two of the emission lines, Table 5.1 summarises the derived spikes and which lines we found them from. We think that the $230°$ and $247°$ spikes come from the same spot, since the spikes were marked out by different emission lines. That gives us a total of 6 lines from this investigation.

The shape of the iron line flux curve in Figure 5.10 looks very different from the H and He flux curves. That can be explained by the [Fe II] lines originating from different sites of the shock than the He and H lines, which would cause the [Fe II] and H-He lines to increase in flux at different times in the shock evolution. This can be understood from the fact that while the H and He lines arise in an ionised region at $\sim 10,000$ K the [Fe II] lines arise at ~ 5000 K, behind the ionised zone. The extent of this photoionized zone, and therefore the [Fe II] flux, depends on the shock velocity. In addition, collisional de-excitation is important for the [Fe II] lines, while the H and He lines are less sensitive to the density, being dominated by recombination. The ratio of the [Fe II] and H and He lines will therefore depend on both the shock velocity and density, which are both likely to vary along the ring. Because $V_s \approx V_{\text{blast}}(\rho_0/\rho_{\text{blob}})^{1/2}$ the shock velocity into the cloud depends on the cloud density ρ_{blob}.

We expect the iron emission to be more and more pronounced as the gas behind the shock front has time to cool down. So far the increase in [Fe II] emission is most pronounced for the region of Spot 1 (HST spot found at $29°$), but we expect the [Fe II] emission to increase all over the ring as the gas has time to cool.

Since the spots have to cool before we pick up the emission in IR we should be able to say something about the cooling time for each spot. But we might have a problem in that the spots were not simultaneously hit by the ejecta. The light travel time for the South side is 1.27 light years longer than that for the North side (assuming a ring diameter of $1.2 \cdot 10^{18}$cm Panagia et al. 1991).
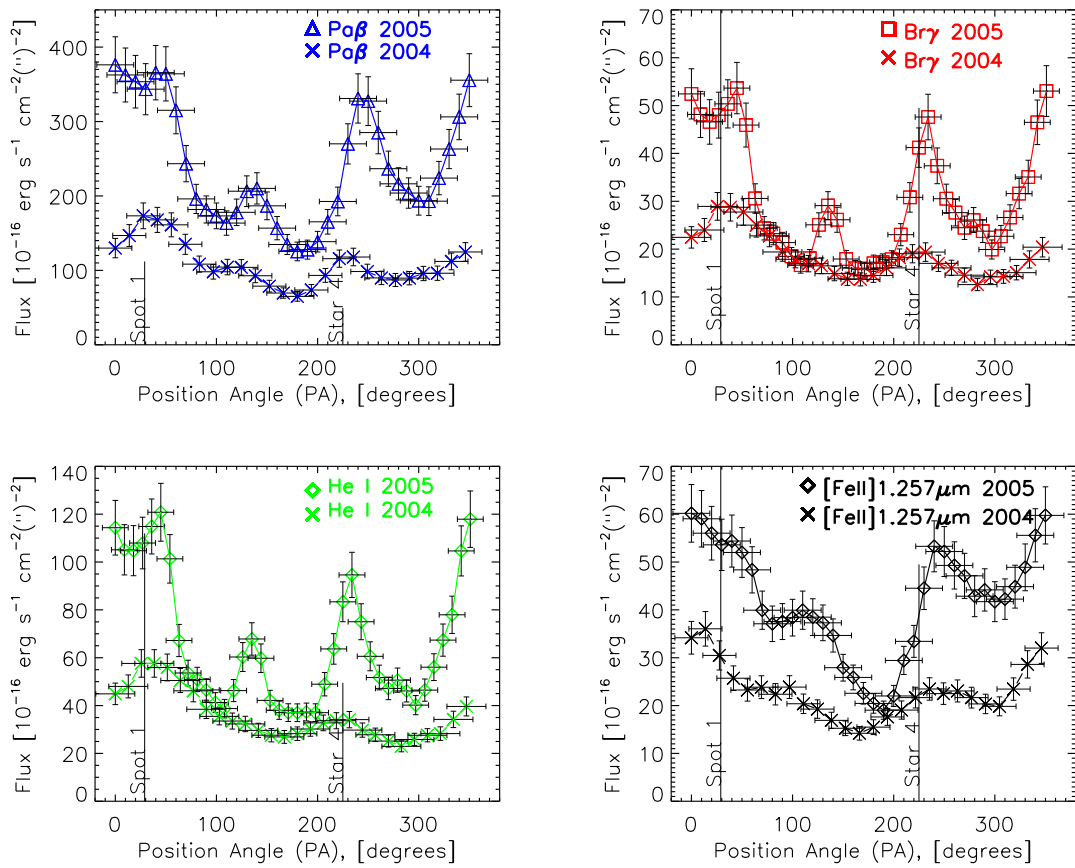
Figure 5.10: Fluxes for different angular positions around the ring for the two epochs. The 2004 epoch (points marked with crosses) is consequently lower in flux than the 2005 epoch. The flux has been scaled with the aperture area for the extraction. The lines shown are: Paβ (top left) Brγ (top right), He I (bottom left), [Fe II] 1.257 μm (bottom right). The location of Spot 1 and Star 4 are indicated. See the text for more details on the two epochs, or look in Figures 5.5 and 5.8. The 2005 epoch has both a higher spatial resolution and better image quality, which is why the peaks are more pronounced for that epoch.
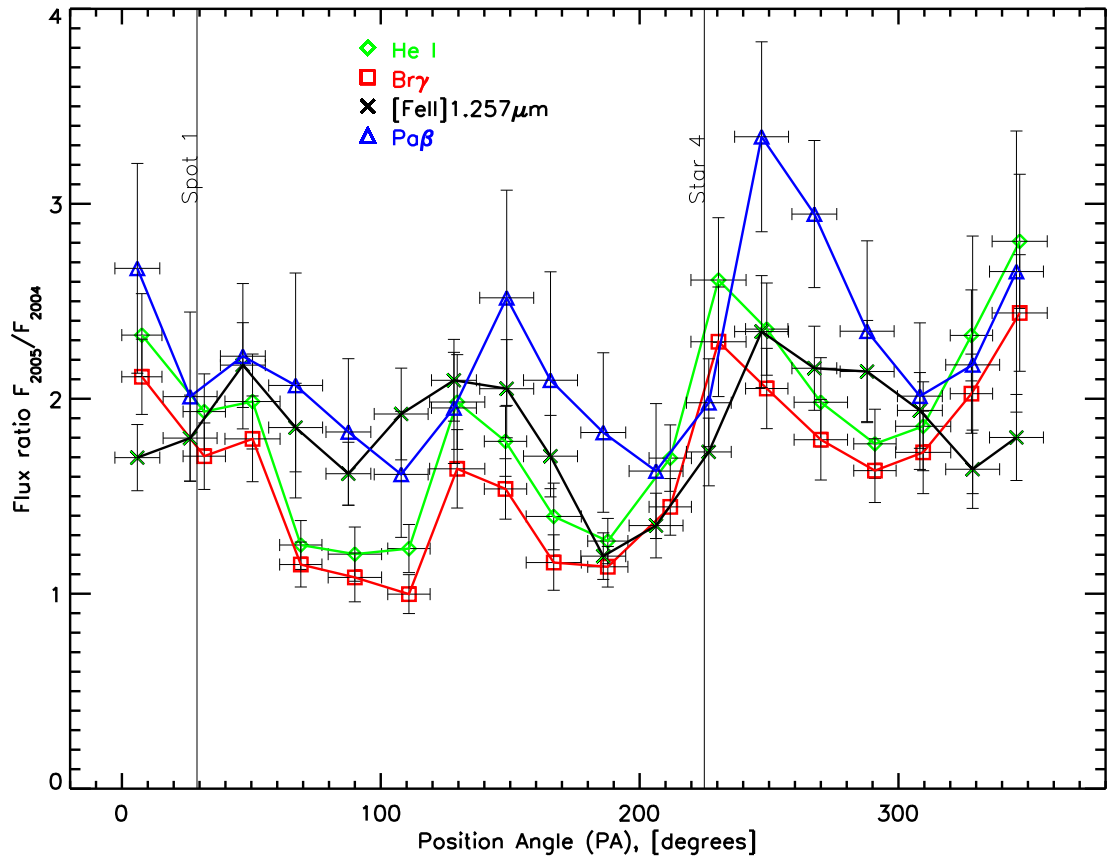
Figure 5.11: Flux ratios between the two epochs for different lines and different position angles (PA). The lines shown are: Paβ (blue/triangle), Brγ (red/square), He I 2.058 μm (green/diamond), [Fe II] 1.257 μm (black/cross). The location of Spot 1 and Star 4 are indicated. See the text for more details.

5.4 Comparison with HST and NACO

Table 5.1 lists the velocity bumps and hot spots found in the previous sections. For all the bumps and spots we list the positions as well as the emission line(s) for which it is detected. For the flux we also list the percentage increase (I) between the two periods and the flux above ring background (FARB, calculated as the peak emission for a spot divided by the minimum flux for the ring in a given emission line). The FARB number from different lines turns out to be of the same order for the individual spots, this is even the case for the spots where the [Fe II] line is included.

For the velocities we list the velocity measured at a bump (either radial velocity or expansion velocity), and for the radial velocity we list the percentage increase (I) per year.

Figure 5.12 shows a HST image (November 2005, from the SAINTS Team/Peter Challis/NASA[1]) with the different spots numbered. The numbering is hot spot: HS 1-029, where the first digit is the sequential number of the appearance of the hot spot and where the following three digit number refers to the position angle of the spot. The sequential numbering has only been completed up to number 14 (Sugerman et al. 2002), where spot 8 and 9 was observed to be only due to reverse shock emission. In the figure we name the remaining spots with letters, starting with A being the first after PA=$0°$. HS B-082 could be emission from Star 6, and HS H-237 could be due to emission from Star 4.

We have in Figure 5.12 marked the positions of radial velocity bumps (green), the expansion velocity bumps (blue), and the increase in radial velocity (red) (from Table 5.1). The bump in the expansion velocity at $307°$ coincides with a place on the ring devoid of emission in the HST images. That makes a lot of sense, since there then is less material to slow down the forward shock, and thus we would expect the expansion velocity of the cooling gas to be larger at this position. This might also be the effect we see at $180°$, where there also is less emission in the HST image, however, slightly more than at the $307°$ position. This could be the reason that the bump at $180°$ stands less out than the bump at $307°$.

Figure 5.13 shows a NACO image (from Danziger et al. October 2006) in the H band, which spatially better resolves the hot spots in the IR. We have in the NACO image marked the spots we found from the flux analysis with blue. The green circles mark the positions of the flux increase we found. The flux increase more or less coincide with weaker spots in the image, where the regular 4 flux spots we found coincides well with the brighter spots in the image. The increase in flux is seen at positions close to hot spots detected in the IR here. The spots we found in the IR coincide with older spots in the optical (old enough to be associated with numbers, except for the spot coinciding with star 4 ($237°$)). Since the emission lines we measure here are originating in the cooling material propagating behind the shock front, the spots will not appear in the IR before the material has cooled down enough to start this emission. This explains why we only see the most evolved spots. There might be a fundamental difference in morphology between the spots that appeared first and the spots that appeared later. We expect that the protrusions to be hit first were longer and thinner (in extend and density) as the gas had thinned out more. The protrusions that was hit later would then be the shorter and more

---

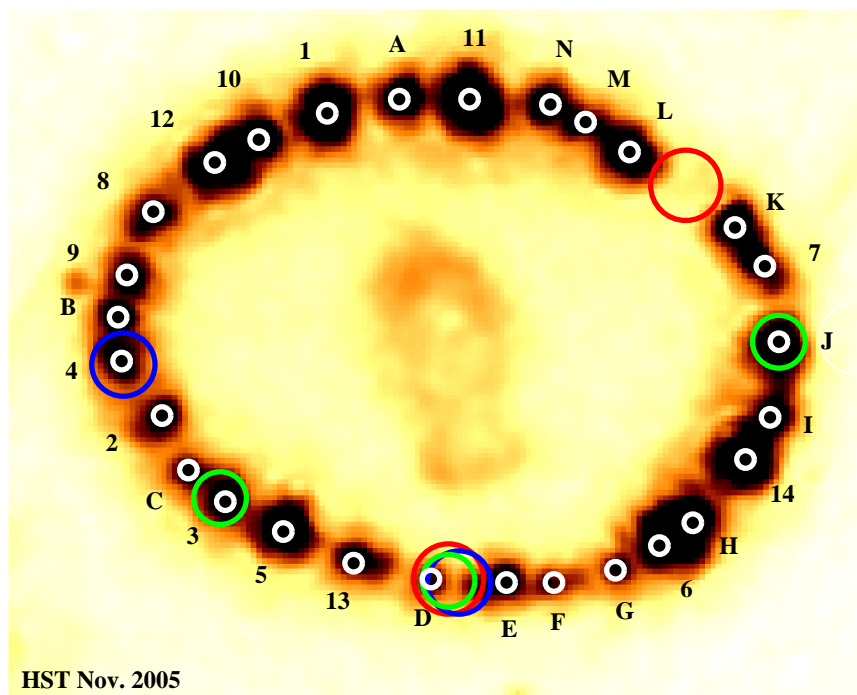[1]From the web page http://www.cfa.harvard.edu/sins/jan2007.html

Figure 5.12: HST (optical) image from November 2005 (courtesy of Peter Challis and the SAINTS team) with the spots numbered according to Sugerman et al. (2002) and Lawrence et al. (2000), the spots marked with letters are newer and has not yet been assigned a sequential number. The positions of radial velocity bumps (green), radial velocity increase (blue) and expansion velocity bumps (red) are marked. The emission in the centre of the ring comes from the debris.

Table 5.1: Summary of bumps derived from sections 5.2 & 5.3. The column 'Method' lists the methods the bumps were derived. The horizontal lines indicate which bumps, that within the errors could originate from the same hot spot.

PA[1]	E_{PA}^1	Method[2]	Which Lines	Values[3]	HST spot
6°	8°	Flux increase	Only from Paβ line	I=170 ±50%/yr	HS A-009
43°	8°	Flux	Paβ, Brγ, HeI, [Fe II]	FARB=2.9-3.4 ±(0.4 − 0.5)	HS 10-040
49°	5°	Flux increase	Paβ, Brγ, HeI, [Fe II]	I=80-120 ±(20 − 40)% /yr	HS 12-050
93°	6°	RV Increase	Paβ, Brγ, HeI	I=12% ± 3% /yr	HS 4-091
121°	5°	RV	Paβ, Brγ, HeI	V_{rad}= 378±2 km s^{-1}	HS 3-126
129°	6°	Flux increase	Brγ, HeI, [Fe II]	I=60-110 ±20% /yr	HS 3-126
137°	9°	Flux	Paβ, Brγ, HeI	FARB=1.7-1.9 ±(0.2 − 0.3)	HS 5-139
149°	10°	Flux increase	Only from Paβ line	I=150 ±60% /yr	-
180°	5°	RV	Paβ, Brγ, HeI	V_{rad}=387±2 km s^{-1}	HS D-176
180°	8°	EV	Paβ, Brγ, HeI	V_{exp}=150±10 km s^{-1}	HS D-176
182°	4°	RV Increase	Paβ, Brγ, HeI	I=14% ± 3% / yr	HS D-176
230°	8°	Flux increase	Brγ & HeI	I=130-160 ±30% /yr	HS 6-229
237°	8°	Flux	Paβ, Brγ, HeI, [Fe II]	FARB=2.6-3 ±0.4	HS H-237
247°	7°	Flux increase	Paβ & [Fe II]	I=130 ±(30 − 50)% /yr	HS 14-249
270°	8°	RV	Paβ, Brγ, HeI	Nodal point − > scatter	HS J-272
307°	9°	EV	Paβ, Brγ, HeI	V_{exp}=150 ±20 km s^{-1}	(HS L-314)
346 °	5°	Flux increase	Brγ, HeI, [Fe II]	I=80-180 ±(20 − 30)% /yr	-
355°	8°	Flux	Paβ, Brγ, HeI, [Fe II]	FARB=3-3.4 ±(0.4 − 0.5)	HS 11-355

[1] PA=Position Angle, with the error E_{PA}

[2] EV=Expansion Velocity, RV=Radial Velocity.

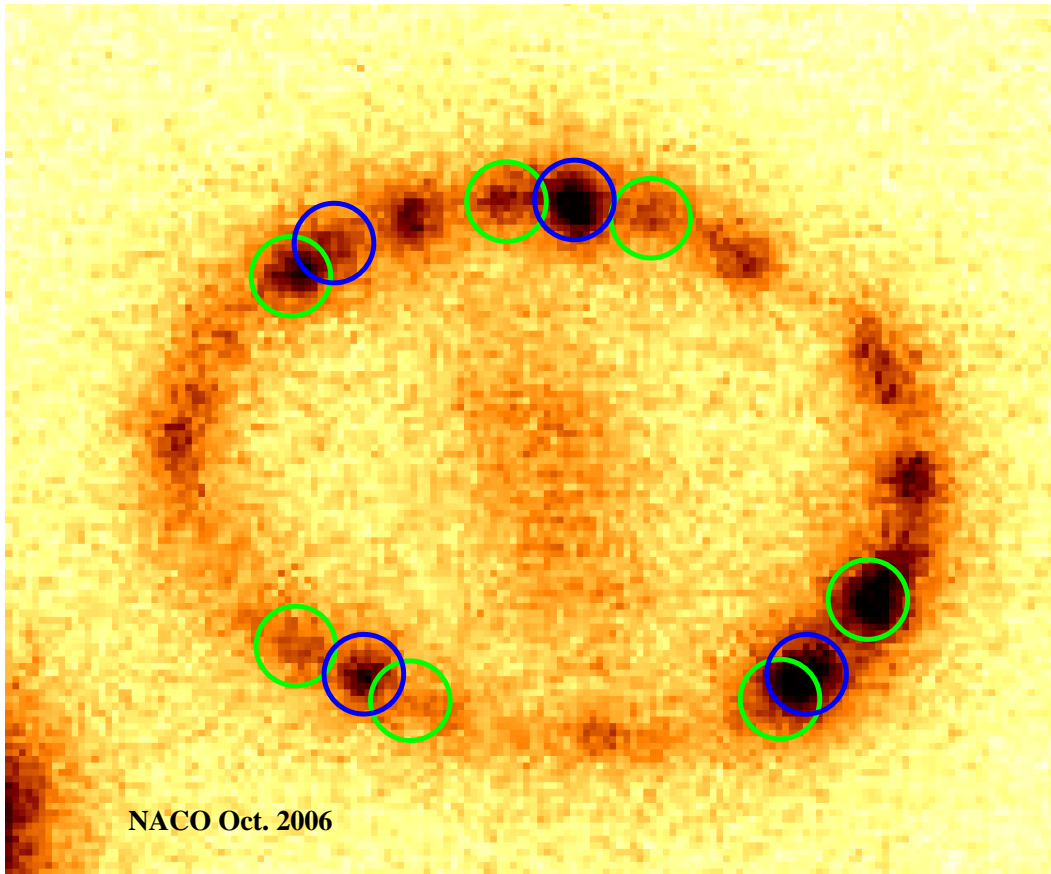[3] I=Increase; FARB=Flux Above Ring Background, see text for details.

Figure 5.13: NACO image from Danziger et al. October 2006 (H band), The hot spots we find in the IR flux are marked with blue rings and the positions where we see and increase in the flux are marked with green rings.

dense protrusions. This scenario can be tested in that the more dense protrusions should result in spots that are luminous for a longer time. However, since the ejecta might be asymmetric (see Chapter 6), it will be difficult to ascertain if a spot was hit earlier or later because of the morphology of the protrusion or because of the possibly non-spherical shape of the ejecta shock expansion.

Sugerman et al. (2002) has looked at the hot spots in detail with HST, however they only cover the first hot spots as the newer ones had not appeared yet. They find that some of the hot spots grow linearly, while others grow exponentially. We did not find any correlation between the two kinds and the spots we pick up with the flux and/or kinematics. Interestingly they also are able to determine the spots' (HS-1, 2, and 3) velocity on the sky as they are pushed radially outwards in the ring. Spot 3, which we pick up in with the radial velocity, was measured to have a velocity of 2460 $\pm$360 km s^{-1} (by Sugerman et al. 2002, de-projected: 2970 $\pm$770 km s^{-1}, assuming a distance to SN 1987A of 50 kpc). This makes spot 3 have a larger outward velocity than spot 1 and 2, which only have de-projected velocities of 2340 $\pm$300 km s^{-1} and 1752 $\pm$600 km s^{-1}, respectively (Sugerman et al. 2002). That could explain why we pick up spot 3 with the radial velocity and not spot 1 and 2.

It could be interesting to compare more with HST, since SN 1987A has been monitored at least in imaging for more than a decade, but most of that data has not been put together in a publication yet. Also integral field spectroscopy in the optical could combine the HST data with the IR data discussed here.

5.5   Results Derived for the Ring

These integral-field observations have revealed the extent of individual emission lines around the ring, and there is emission from the entire ring. Only a few hot spots can be individually identified by their emission, and they are not evenly spaced like the hot spots in the optical. This could indicate that the infrared emission is delayed in time with respect to the optical emission, since the shocked gas material needs to cool down before it can emit in the infrared.

The kinematics for the ring are consistent with a circular ring (as opposed to an ellipse), and by identifying the nodal points for the ring's inclination, the major axis has been found to be at position angle 81° $\pm$ 7° as measured from North through East (which agrees well with the 81° $\pm$ 0.°8 found by Sugerman et al. 2005). Also from the kinematics a radial velocity curve for the ring has been established, which shows significant differences of the velocities around the ring, with the eastern segment showing larger velocities than the western segment. This correlates well with the increase in surface brightness seen in both the radio observations (Manchester et al. 2002), Chandra observations (Park et al. 2006) and the appearance of Spot 1 in the East (Michael et al. 2002; Pun et al. 2002; Sugerman et al. 2002). The differences could be due to one or several of the following causes (i) differences in the densities of the material in the ring slowing the shock front down, (ii) differences in the ejecta outflow (suggested by Lawrence et al. 2000, as the cause for spot 1), (iii) by the supernova not being situated in the

centre of the ring (Sugerman et al. 2002; Plait et al. 1995, found that the ejecta was not situated in the centre of the tilted ring).

The radial velocities have been de-projected into an outward velocity of the shocked gas component in the ring for different position angles. Rather than begin constant for all angles, the expansion velocity of the shocked gas was larger at PA=307°±9° than the immediate gas around it. This position could be identified with a vacant section of the circumstellar ring in the HST images. This suggests that the vacant region has a lower density than the rest of the ring, since the forward shock, and ultimately the shocked gas component then would be decelerated less by the ring. This might reveal the structure of the ring to be not so much a ring, but rather a circular collection of clumps. Whether the ring is a ring or clumps will become obvious the coming years, as the hot spots are expected to merge if it is a ring.

From the velocity shift of the lines I find an average outward velocity of $\sim 100 - 200$ km s^{-1} for the bulk of the H and He emitting shocked gas. This is just the average velocity, and considerably higher velocity shocks are present, as is directly evidenced by UVES observations (Gröningsson et al. 2006, 2007).

Chapter 6

The Ejecta

In the simple supernova case without any circumstellar material the ejecta are freely expanding such that the further away from the supernova we observe the ejected material the larger the outward velocity of the material is (resembling the Hubble flow, v=r/t).

For SN 1987A the ejecta can be seen in two places: (i) in the reverse shock where the ejecta collide with shocked material and are slowed down, and (ii) in the inner ejecta heated by the radioactive decay (see Fig. 6.1, and chapter 1 for details). The inner ejecta will naturally show lower velocities than the ejecta entering the reverse shock, and the velocity difference is one of two ways to distinguish between the two places of emission. With integral field spectroscopy we are also able to distinguish between the two positions by looking at the place of the emission with respect to the ring. Further away from the centre it is more likely that we see the emission in the reverse shock.

Figure 6.1: Illustration of the emission sites from Chandra PR pages.

For epoch 2004 we only managed to observe the ejecta for one line ([Fe II] 1.644 μm). Section 6.1 of this chapter contains all we could derive on the ejecta from the 2004 data set and was published in Kjær et al. (2007b). With the 2005 epoch we were fully able to investigate the inner ejecta emission and its velocity distribution.

6.1   Epoch 2004

Our 2004 epoch observations with the 250 mas spaxels do not have sufficient spatial resolution to resolve the shape of the ejecta, while the J100 does not have enough signal for us to determine the shape of the ejecta. Spectrally we do however see a broad component in the 2004 data set.

The only line, for which we clearly can separate the broad ejecta component from the intermediate-velocity component in the integrated spectrum is the [Fe II] λ1.644 μm line. Figure 6.2 shows
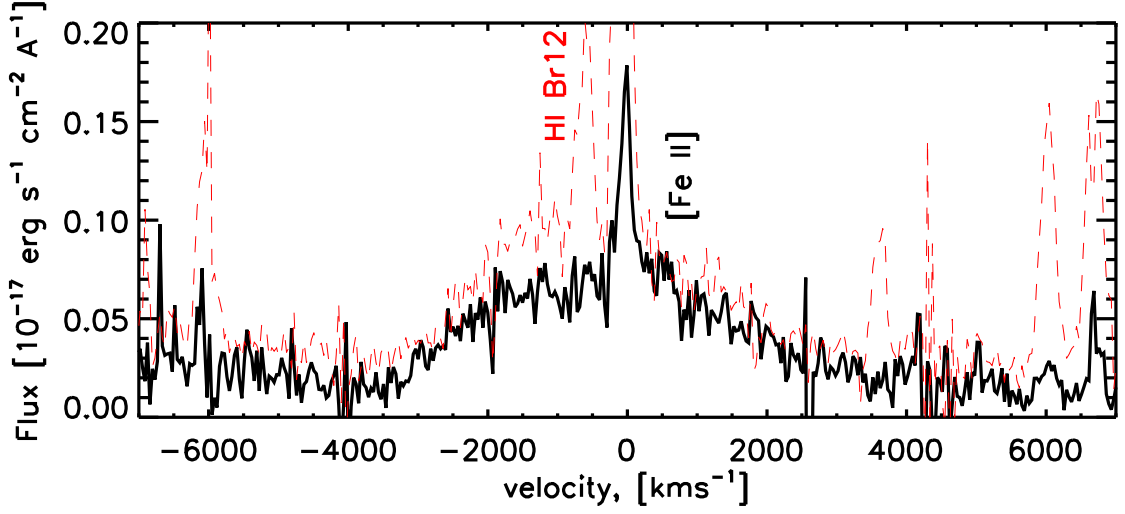
77

Figure 6.2: The [Fe II] $\lambda 1.644\,\mu$m line from a single spaxel centred on the ejecta at the centre of the circumstellar ring (aperture=1 spaxel). The intermediate/narrow line on top is scatter originating in the ring. The red/dashed curve is the extraction at $25°$ (aperture area A=$\pi *$ $(0.375'')^2$) scaled down with a factor of 10.

this line from a single spaxel centred on the ejecta in the centre of the circumstellar ring (full curve), for comparison we have plotted an extraction from Spot 1 (dashed line). The emission from Spot 1 has the intermediate Br12 line which is not present in the ejecta emission, furthermore there seems to be more blue emission in Spot 1 than in the ejecta.

For the integrated spectrum when we fit a Gaussian to both the broad part and the intermediate part of this line we find a small offset in the central wavelength, so that the broad line seems less red-shifted than the intermediate line, with respect to the rest frame of the system (v_{SN} = 286.5 kms^{-1}, Meaburn et al. 1995). The two components are individually listed in Table 4.2. For the broad component we derived a velocity shift of 150 kms^{-1} and a $\sigma_{deconv} \approx 3400$ km s^{-1}. The bluer central wavelength for the ejecta component could indicate that the red part of the line is obscured by dust, as observed in the optical by Lucy et al. (1991).

For the 2004 epoch we observe a broad line in the ring spectrum, which might be originating in the reverse shock. We assigned an azimuthal angle for each position on the ring, defining North as zero degrees, and increasing the angle through East. The top panel of Figure 6.3 shows the size of the extractions and their corresponding positions and azimuthal angles, and the bottom panels show the spectrum of [Fe II]1.644μm for the different extractions. It is clear from this figure that the velocity shift of the [Fe II] 1.644 μm line's narrow component is not changing much for different azimuthal angles (different positions on the ring). Around Spot 1 and on the eastern side in general a broad component of the line emerges ($\sim$ 7000-8000 km s^{-1}, full width zero intensity (FWZI)). The shape of the broad component (BC) changes even on the eastern side, with a slightly more luminous blue wing at 25 degrees, and a slightly more luminous red side at 99 degrees. However the ratio of blue to red flux in the broad component changes with azimuthal direction away from Spot 1 (see Fig. 6.3). Therefore we conclude that
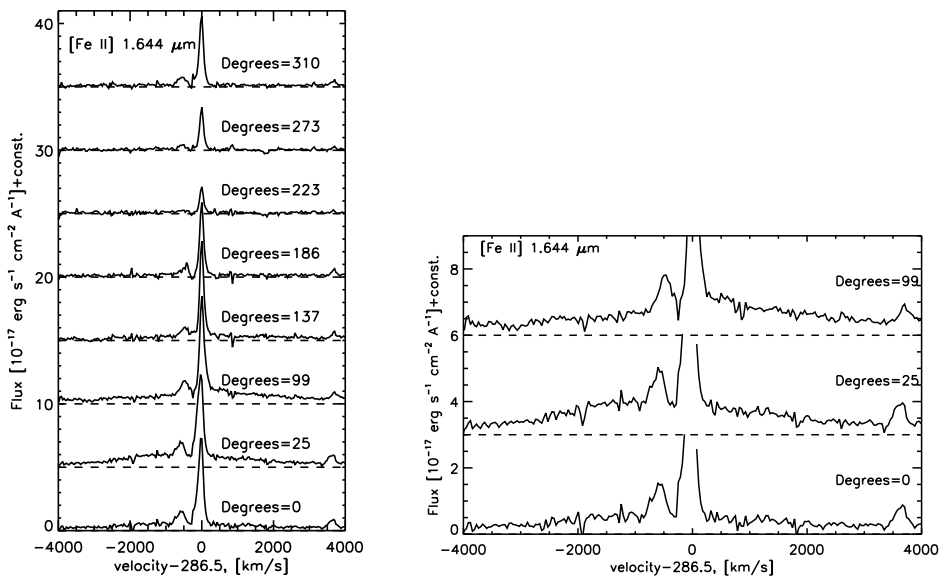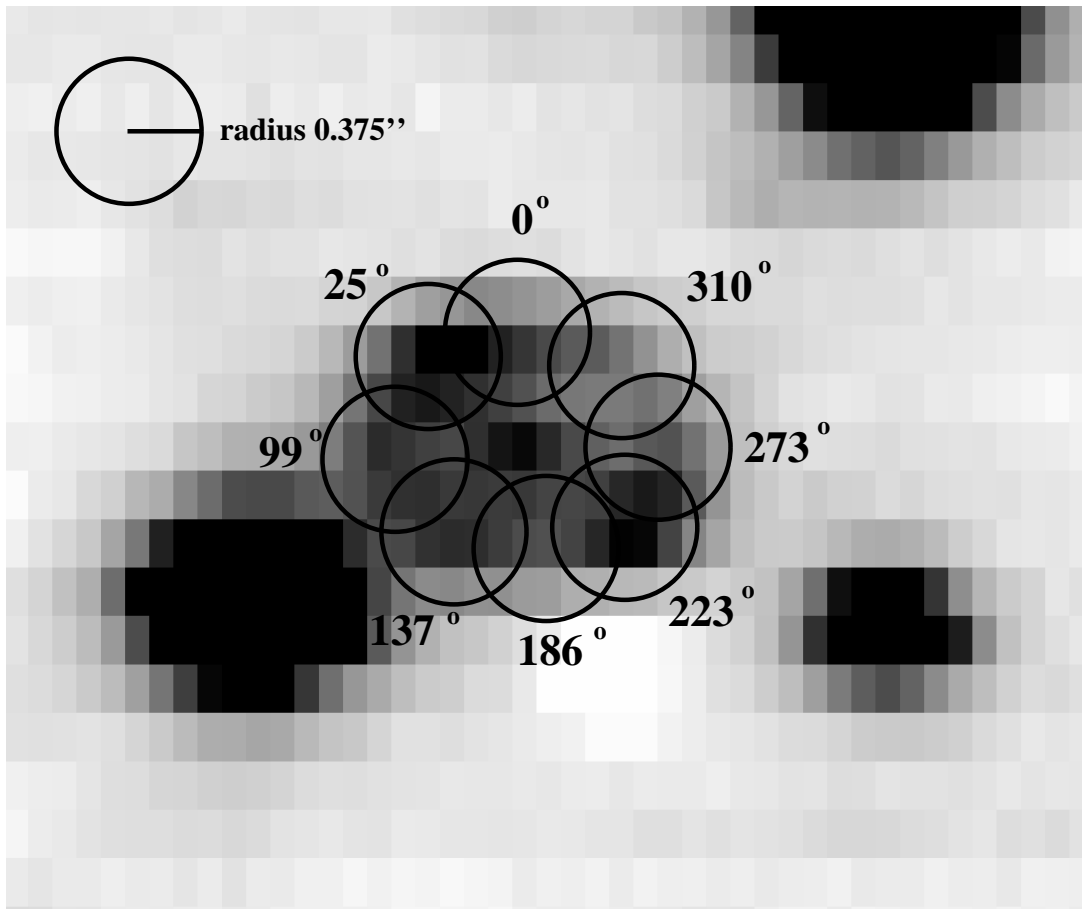
Figure 6.3: Top: The size of the extractions and the corresponding azimuthal positions in the H band. North is up and East is left. Bottom: Extraction of spectra from the reduced data cube in the H band. The spectra are plotted with an offset. The faint emission on the blue side of [Fe II]1.644μm is Br12. The right panel is an enlargement of the left panel.

the emission is not only scattered emission from Spot 1. Given the accuracy of this data set we cannot definitively exclude that the emission is originating from the ejecta. Following the thorough discussion of the shocks in Pun et al. (2002) we think that the broad emission in the ring emerges from the reverse shock, which would be bluer in the North part of the ring due to the inclination of the ring with respect to the line of sight, which is consistent with our observations. However, the reverse shock has previously only been found with much larger velocities (12000-15000 km s^{-1} for Hα Gröningsson et al. 2006). Perhaps the forbidden lines, such as the [Fe II] line, all enter the reverse shock region with generally lower velocities, that would certainly explain why we find a velocity component located in the ring with a width of 7000-8000 km s^{-1}.

The broad line is only pronounced on the Eastern side of the ring. This East-West asymmetry has also been observed in X-rays and radio most recently in Park et al. (2006) and Manchester et al. (2002), respectively. The X-ray and radio emission is thought to emerge from the same region as the IR behind the shock front as the material cools down. We see also an East-West asymmetry with the intermediate lines, in that the Eastern side is brighter than the Western (see Fig. 5.5).

Whether the East-West asymmetry is due to asymmetric ejecta outflow or differences in the density of the circumstellar matter (protrusions) is still an open question, which integral field spectroscopy observations of the reverse shock would shed light on. Since the hot spots primarily first appeared on the Eastern side we could also be witnessing spot evolution.

6.2   Epoch 2005

With the 2005 data-set we can isolate the central ejecta emission much better. This section is divided into the different analysis methods, followed by a section with calculations of the properties and geometry for the ejecta.

6.2.1   The Ejecta Spectrum

In the RGB image (Figure 3.4) we see that the ejecta is dominated by the green colour, indicating that the central emission is strongest in the H band. This is confirmed when we look at the spectra for the central region for all bands in Figure 6.4, where the colour scheme follows that of Figure 3.4. We made circular extractions of the central region with an aperture radius of 0.375" corresponding to the worst image quality in Table 3.4. In the figure we see that the emission is entirely due to individual emission lines and thus not due to some faint continuum caused by thermal radiation. The narrow and intermediate width lines are contamination from the ring, which is why it is only the brightest of them which are present. The different emission lines are listed in Table 6.1 with possible line identifications. These line identifications can only be confirmed via modelling, as the wavelength positions of the lines could be affected by differences in the ejecta outflow and dust.

Table 6.1: Emission lines of the central region (aperture area $A = \pi * (0.375'')^2$). Errors for the values listed in the table are given either in the text or in Table 3.2. The flux is measured in 10^{-16}erg s^{-1} cm^{-2}. v_{rest} is the velocity after correction of the systematic velocity of SN 1987A (286.5 km s^{-1}). The source for the line identification (NIST) is discussed in the text.

| λ_{obs} (μm)	σ_{obs} (km s^{-1})	σ_{deconv} (km s^{-1})	Flux	Identification	λ_{air} (μm)	v_{obs} (km s^{-1})	v_{rest} (km s^{-1})
1.19850	6235	6232	35	Fe I	1.1973	298	11
1.20096	6871	6869	61	N I	1.19983	279	-7
1.28230	1217	1204	5	C I	1.28113	272	-15
				Mg II	1.28102	298	12
1.35462	4031	4027	17	N I	1.35346	254	-33
1.49798	4226	4223	12	N I	1.49666	262	-24
1.53527	3186	3181	12	C I	1.53376	293	7
1.60484	4584	4581	15	C I	1.60217	498	211
				Mg IX	1.60470	24	-262
1.64497	3448	3443	41	[Fe II]	1.64350	266	-20
1.73987	3916	3913	5	N II	1.73761	388	102
				Na VI/ Fe XV	1.73870	200	-86
1.97999	2801	2795	3	[Fe I]	1.98040	-64	-351
				C I	1.98087	-135	-422
				Si IV	1.98003	-8	-295
				Fe I	1.97919	119	-167
				C I	1.97907	137	-149
2.05948	4693	4690	10	O II	2.05701	358	71
				He I	2.05810	199	-88
				N II	2.05899	69	-218
2.12185	3590	3586	4	H$_2$	2.12100	118	-168
				C III	2.12170	19	-267
				Mg I	2.12081	145	-142
				C I	2.11918	376	89
2.41343	5431	5428	11	Mg II	2.41245	120	-167
				CO (6-4)	2.41354	-16	-302
Although a CO line would have a very specific shape							
The elements: H, He, C, N, O, Na, Mg, Si, S, Ca, Fe, Co, Ni have been tested							
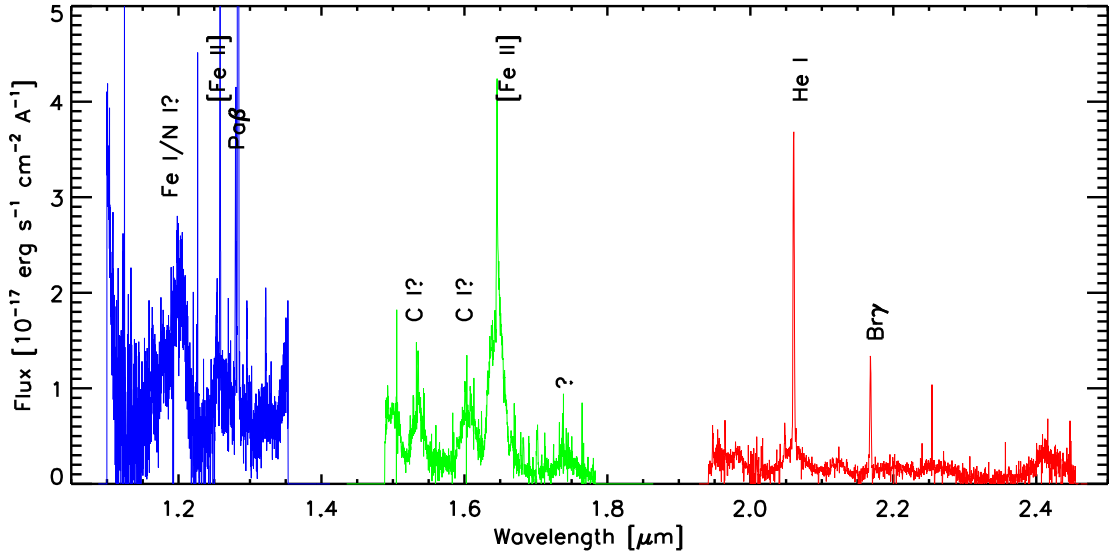
Figure 6.4: The central emission for a circular aperture with radius=0.375" in J, H, and K 2005 (aperture area $A = \pi * (0.375'')^2$). Blue is the J band, green the H band, and red the K band.

6.2.2 Velocity Distribution of the Ejecta

In the 2005 data set we spatially resolve the central emission in the H and K band and this gives us the opportunity to find the velocity distribution across the emission region. To do this we use the lines from Table 6.1, for which we are confident of the line identification. Those lines are the He I line in K (2.0581 μm) and the [Fe II] line in H (1.6435 μm).

For the K band we used an extraction radius of 0.15" (6 pixels), which makes the diameter slightly larger than the image quality (0.175"-0.275"), see Table 3.4. Two extractions are then independent if their centres are separated by 12 pixels. We placed 7 extractions so that the North and South extraction are independent and East and West are independent. The size of the extractions and the seeing are such that we also get emission from the ring. Figure 6.5 shows the extractions and the resulting spectra. In the analysis of the line shapes and positions, we cut out the narrow and intermediate component in order to limit the contamination from the ring. The resulting velocities for the broad component (BC) show a blue shift in the North and a red shift in the South. The majority of the flux is in the South and South-West extractions. The North-East bin has larger flux than the Northern bin, which could be due to contamination of the strong emission from spot 1 (PA=29°). The distribution of the fluxes show that the broad component emission is not symmetric along the North-South and East-West axis for this line. The values are summarised in Table 6.2.

We repeat this velocity investigation in the H band for the dominating [Fe II] line, using the same extraction size and spatial positions, in order to compare the two lines. Figure 6.6 shows the extractions and the resulting spectra. The velocity distribution for the [Fe II] 1.6435 μm line across the central emission region confirms the measurement of He I lines in the K band. North
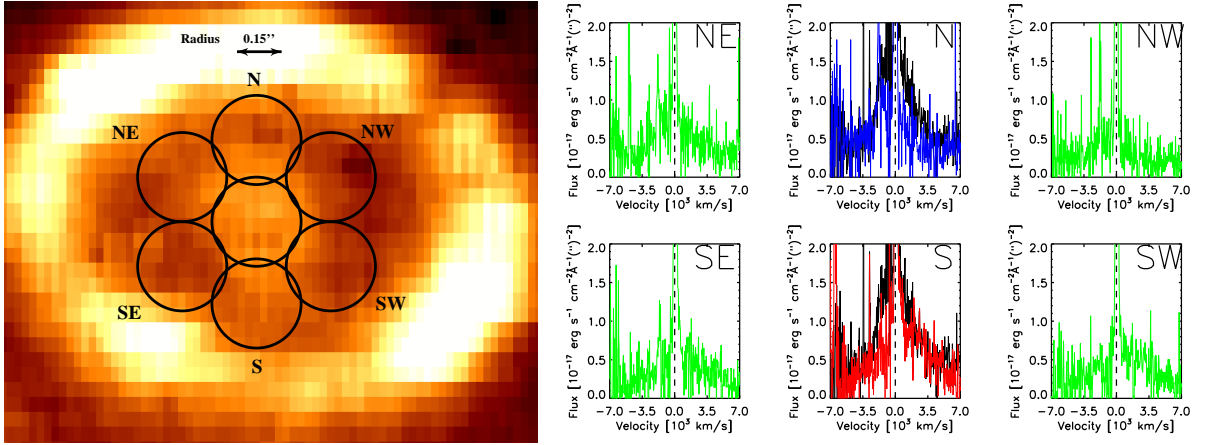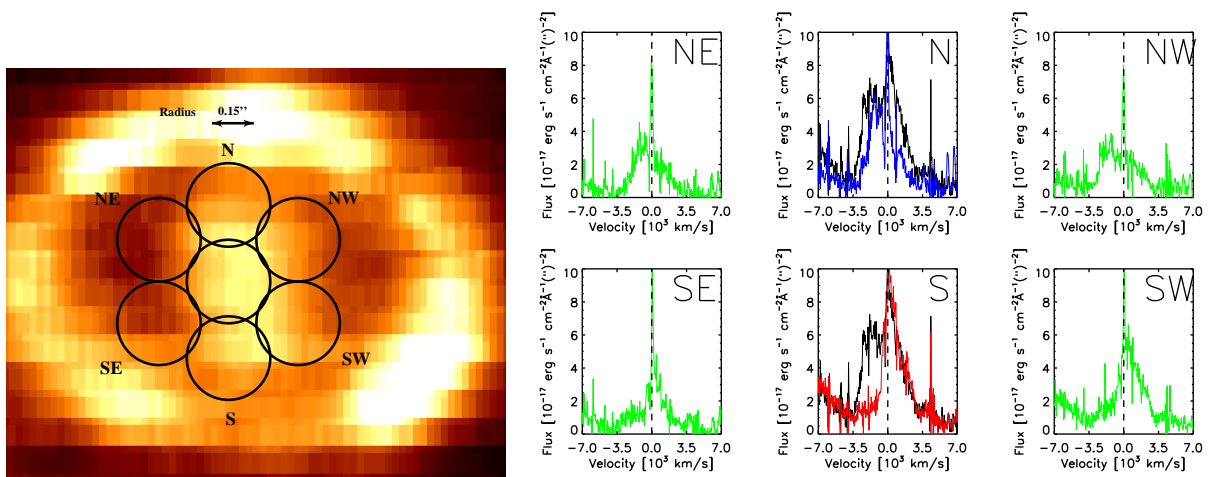
Figure 6.5: Left: K band 2005 image of the central region extractions with radius 0.15" (aperture area A=$\pi * (0.15'')^2$). Right: The spectra of the extractions centred on the He I 2.058 μm line. The black full line is the central extraction in the left panel, the dashed curve is the zero shift for this line.

Table 6.2: Derived values of the He I line (2.058 μm) for the different central region extractions (aperture area A=$\pi * (0.15'')^2$). Errors for the values listed in the table are given either in the text or in Table 3.2. v_{rest} is the velocity after correction of the systematic velocity of SN 1987A (286.5 km s^{-1}).

Position	λ_{obs} (μm)	v_{obs} (km s^{-1})	v_{rest} (km s^{-1})	σ_{deconv} (km s^{-1})	Flux 10^{-16}erg s^{-1} cm^{-2}/$('')^2$
North	2.05957	226	-60	509	5
North-East	2.05547	-371	-657	4133	21
South-East	2.06067	386	100	737	8
South	2.06463	963	677	5810	46
South-West	2.06508	1029	742	7340	27
North-West	2.05577	-327	-614	3813	12
Central	2.05954	222	-65	2937	50

Table 6.3: Derived values of the [Fe II] 1.6435 μm line for the different central region extractions (aperture area A=$\pi * (0.15'')^2$). Errors for the values listed in the table are given either in the text or in Table 3.2. v_{rest} is the velocity after correction of the systematic velocity of SN 1987A (286.5 km s^{-1}).

Position	λ_{obs} (μm)	v_{obs} (km s^{-1})	v_{rest} (km s^{-1})	σ_{deconv} (km s^{-1})	Flux 10^{-16}erg s^{-1} cm^{-2}/$('')^2$
North	1.64109	-441	-728	3041	79
North-East	1.64277	-135	-422	3407	56
South-East	1.64623	496	209	2182	40
South	1.64714	662	375	1871	85
South-West	1.64802	822	536	2932	73
North-West	1.64090	-476	-763	3881	51
Central	1.64294	-104	-390	4046	152

Figure 6.6: Left: H band 2005 image of the central region extractions with radius 0.15" (aperture area $A = \pi * (0.15'')^2$). Right: The spectra of the extractions centred on the [Fe II] 1.6435 μm line. The black full line is the central extraction in the left panel, and the dashed curve is the zero shift for this line.

is blue shifted and South is red shifted following the velocity distribution of the circumstellar ring, see Chapter 5. In this binning we can better determine a symmetry axis of the emission based on the flux, since we see that the emission is not only elongated in the North-South direction, it is also more luminous in the NE bin compared to the NW bin. However, since the SE bin is also more luminous compared with the SW bin, we have a pure East West asymmetry, leading us to believe that the centre of our binning is not placed in the middle but slightly offset to the East.

For the velocities we see a different symmetry axis, in which the NW bin is more blue shifted than the NE bin, and the SW bin is more red shifted than the SE bin. This means that the velocities are more extreme on the western side, and lower on the Eastern side. Again our choice of bin size and position possible hold a large influence in this result.

6.2.3 Velocity Maps of the Ejecta

We applied the Adaptive Voronoi 2D-Binning (see Chapter 2.4, Cappellari & Copin 2003) to the central region setting the desired signal to noise ratio to 10. Using a lower ratio we would get more bins, but already at 5 the program aborts, because it can find individual pixels with that signal to noise ratio without binning. Figure 6.7 shows in the left panel the central region that we applied the binning routine to (marked by a rectangular box) and the resulting bins are displayed in the right panel. We used an image of the [Fe II] 1.644 μm line to establish the signal in the pixels and the noise was found from a map between 1.745-1.760μm, which was devoid of emission lines. The spatial scale in arcseconds is chosen so that the lower left corner is at zero.

The [Fe II] 1.644 μm emission line for the ejecta has a very irregular shape, and at some bins it looks like the line is a composite of two or more lines. Nevertheless we fitted a Gaussian profile to the broad emission line and deduced from that the FWHM and the central wavelength for
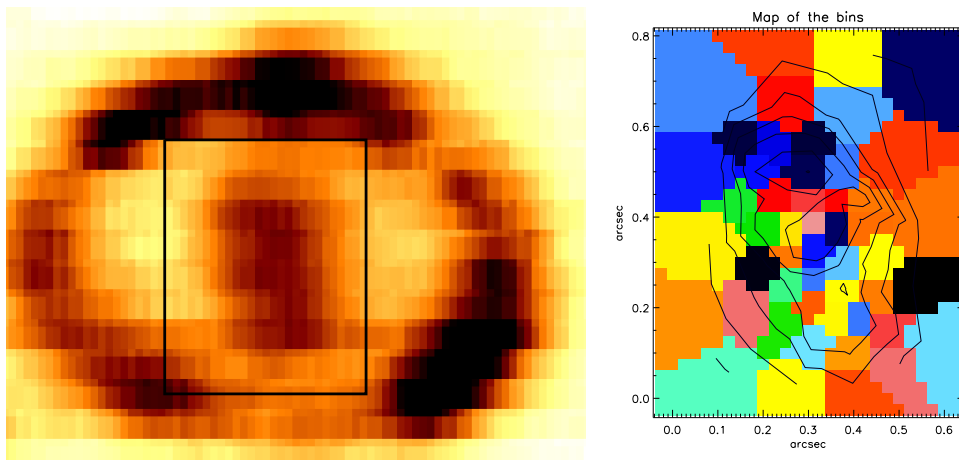
Figure 6.7: Left: the area of the ejecta used in the constructing the velocity map(H-band). Right: the Adaptive Voronoi 2D-Binning applied to the area shown left. The colouring is random to illustrate the individual bins. The contours illustrates the flux levels for the ejecta.
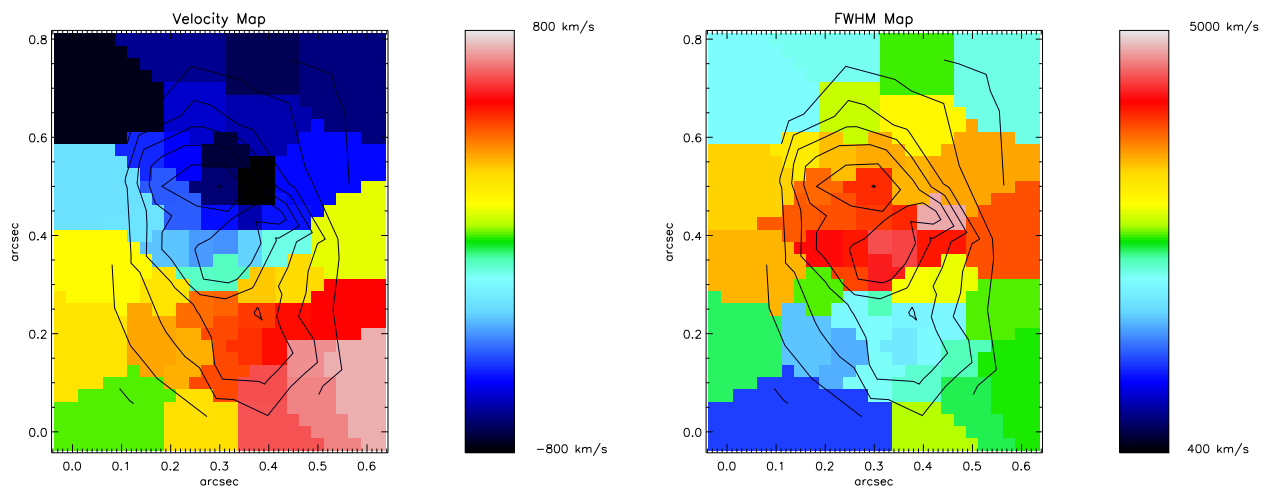

Figure 6.8: Maps from the boxed region in Fig. 6.7. Left: the radial velocity map of the ejecta subtracted the systemic velocity of 286.5 km s^{-1}. The velocity has been derived using a Gaussian fit to the line profile. Right: the FWHM map for the ejecta. The contours are derived from the flux.
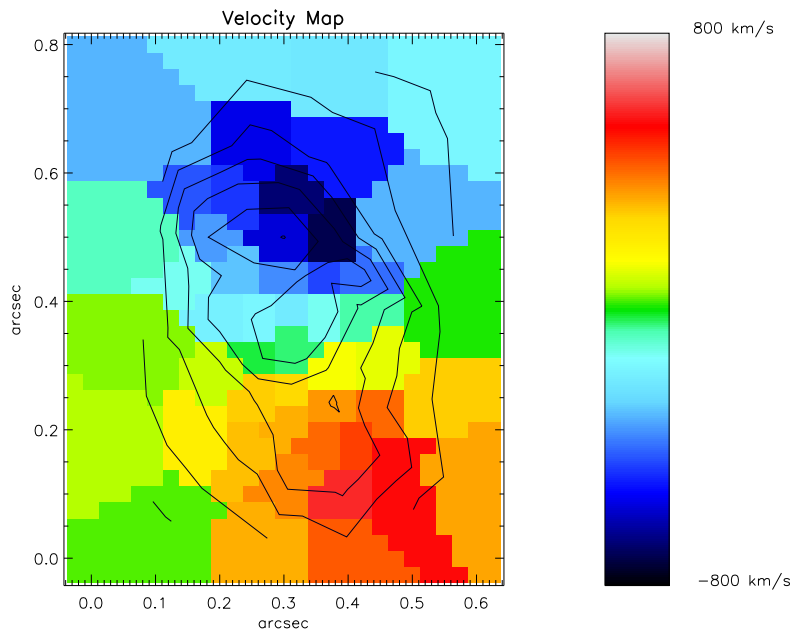
Figure 6.9: The radial velocity map of the boxed region in Fig.6.7 of the ejecta subtracted the systemic velocity of 286.5 km s^{-1}. The velocity has been derived using the 'centre of gravity' to identify the central position of the line, see text for details.

the different bins. The intermediate component was visible in several bins and we chose to cut it away and focus only on the broad component. The resulting velocity and FWHM maps are shown in Figure 6.8.

The shape of the [Fe II] 1.644 μm line is not Gaussian, and in fitting a Gaussian function to the shape and from that derive the velocity is not entirely correct. The wings of the [Fe II] 1.644 μm line determines to a great extent the Gaussian derived central position of the line, which consequently means, that the derived values for FWHM is believable. In order to find the central position of the line, we also applied a different method, in which the wavelength position, that divide the total flux from the line in two equally large parts, is sought. We refer to this method as 'the centre of gravity' and briefly note, that this method flux weights the points on the line profile. The resulting velocity map is shown in Figure 6.9.

There is good agreement between the velocity map in Fig. 6.9 and Fig. 6.8 even though the intermediate component from the ring was discarded in the Gaussian fit and not in the 'centre of gravity' method. For the 'centre of gravity' method we included all flux from the line, which then subsequently resulted in the edge bins closer to the ring to have velocities closer to the rest velocity for the system.

The velocity maps confirms the velocity distribution found from circular apertures, in that the North part is blue shifted and the South part is red-shifted. There is a clear gradient from North to South, and the red and blue shift are of the same order. That implies that there is no dust obscuring the red part of the spectra. Furthermore, the South Western (lower right corner) of the Gaussian velocity map is more red shifted than the South Eastern corner. This is mirrored in

86

the North Eastern corner (upper left corner), which shows a slightly more blue shifted velocity than the North Western corner. This symmetry suggests that the outflow velocities follows the flux density shape, which is not purely North South elongated, but rather tilted slightly in the NE and SW direction. However, the bins at the edge of the velocity map are large because the signal to noise is lower in that region, and the interpretation of the results are thus only tentative for that area.

From the FWHM map we see that the width of the line is larger towards the centre than in the North or South. This is because we really only see just the blue shifted material in the North and just the red shifted material in the South. That bipolar structure will be discussed in the next section.

6.2.4   Geometry and Kinematics of the Ejecta

That the North part of the ejecta is blue shifted and the South part red-shifted is a surprise, and totally opposite with what one would expect.

The symmetry axis for the triple ring system is perpendicular to the ring, and this axis should be the same as the rotation axis of the progenitor. Whenever there is bipolar outflow in supernova explosions it happens along the rotation axis. This is because the rotation of the star has made the polar regions less dense, and the jet can then plunge through more easily. For SN 1987A it has been expected that any bipolar outflow should be along the rotation axis perpendicular to the inner ring. This would cause the Southern part of the ejecta emission to be blue shifted and the Northern part red shifted, -contrary to what we find. See Figure 6.10 for an illustration of the geometry and the expected outflow direction. Before we start explaining this we first attempt to put constraints on the geometrical parameters.

We investigate the FWHM derived from the Voronoi 2D-Binning further and plot the values vs. North-South position for different East-West bins in Figure 6.11 (right panel). We see in this figure that in general the rise in FWHM from South to the middle is steeper than for the North to the middle, which suggests that the South part of the ejecta is more collimated than the North part. It could also be an effect of the light travel time in the system, if the line gets broader with time.

As we could see in the FWHM map of the previous section, the FWHM reaches a maximum in the middle of the emission, corresponding to a central position where both the red and the blue wing of the ejecta are observed. This is reproduced in the right plot of Figure 6.11.

We plot the velocity gradient in a similar way in Figure 6.11 (left panel), with the Gaussian velocity vs. North-South position for different East-West bins. We have omitted points coming from the larger bins close to the edge of the binning region to avoid contamination from the ring. We clearly see the velocity distribution is regular in the the North-South direction, even for different East-West bins. We fitted a line to the velocity gradient (Fig. 6.12) and found the gradient vs. the North South position, $NS_{position}$ to be:

$$V_{grad} = 962 \pm 66 \text{ km s}^{-1} - 2840 \pm 170 \text{ km s}^{-1}('')^{-1} \times NS_{position} \qquad (6.1)$$
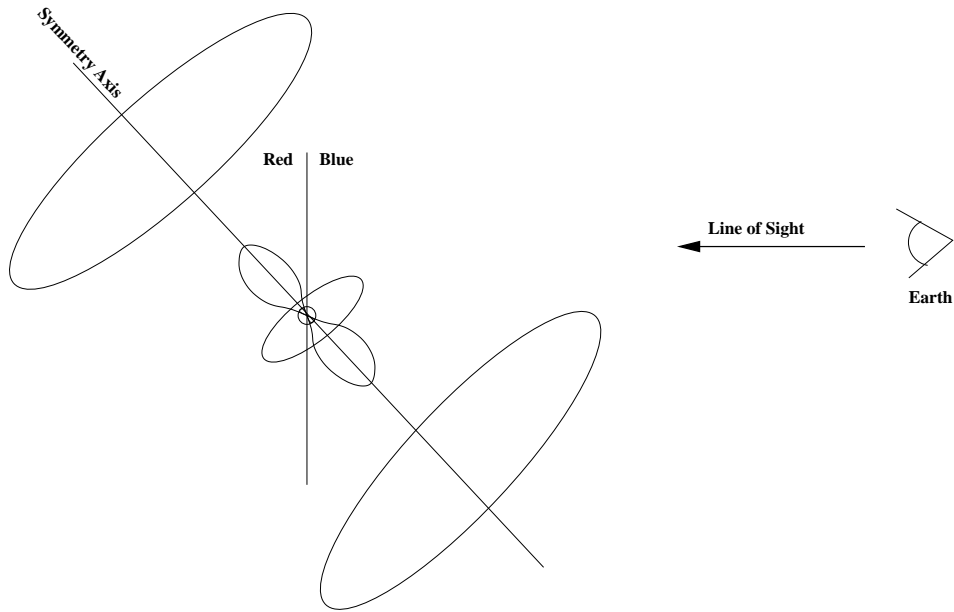
Figure 6.10: SN 1987A rings and symmetry axis. The expected ejected outflow along the axis of symmetry is also drawn.
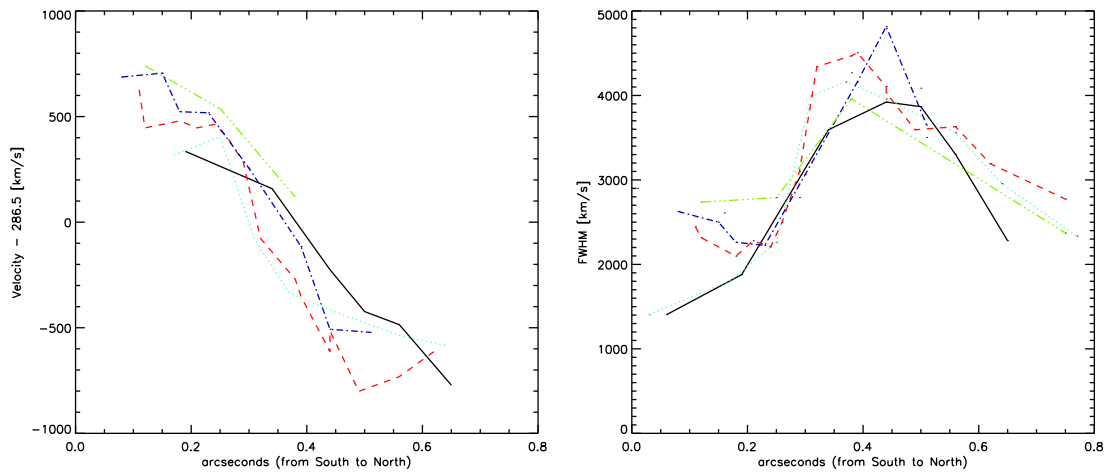

Figure 6.11: Left: The velocities vs. North South positions for different East West bins. Right: The values of FWHM vs. North South positions for different East West bins. Bins: solid line/ black is for the 0.1"-0.2", dotted/light blue = 0.2"-0.3", dashed/red = 0.3"-0.4", dash-dot/blue = 0.4"-0.5", dash-dot-dot/ green= 0.5"-0.6". 5 points originating from large bins at the edge of the binning are omitted.
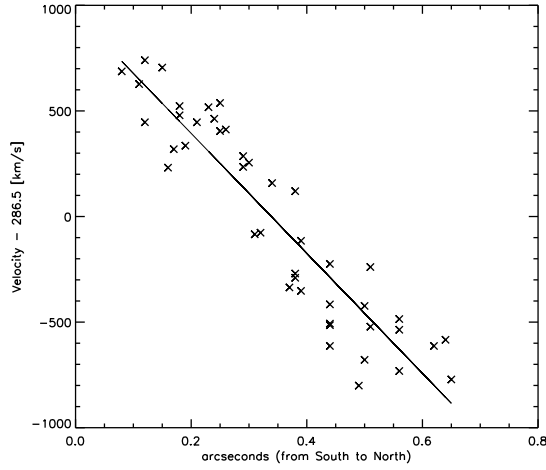
Figure 6.12: The velocities vs. spatial North South positions, the points from very large bins at the edge of the box in Fig. 6.7 has been omitted. The straight line is the result of a linear fit, see text for details

In the left panel of Fig. 6.11 saw that the different East-West bins had almost similar gradients, and thus the above formula yields the average gradient for different East-West bins, since the points are from all of the bins. From the formula we find the position of rest, where the velocity value is zero (i.e. where the observed velocity was 286.5 km s^{-1}) for this line along the North South line, to be: $NS_{pos} = 0.34 \pm 0.03$.

We can calculate the time it took the material to move the projected distance by looking at the most blue shifted and most red-shifted material in the wings of the line profile. Figure 6.13 shows two spectra of the ejecta taken at different positions, which will be used for this analysis. The most blue shifted material furthest North (right panel) has a projected velocity of $V_{blue} = -2750$ km s^{-1} and the most red-shifted material furthest South (left panel) has a projected velocity of $V_{red} = 2750$ km s^{-1}. If all of this material originated in the same position, then the projected distance travelled is d=(68-48)/2 pixels, corresponding to 0.25". Assuming a distance of 50 kpc to the SN the projected distance is d=1.87 $\cdot 10^{12}$ km. The time it takes material travelling at a speed of 2750 km s^{-1} to go the distance d is: 21.6 ±4 years, if we use 0.05" (2 pixels) as the position accuracy. This confirms that the iron was created in the explosion (and in the subsequent radioactive decay).

Geometry

From the contours of the emission (Figs. 6.7-6.9) we find the position angle of the [Fe II] ejecta to be $17° \pm 3°$.

We will in the following attempt to find an inclination angle in the plane of the sky along the North-South axis. From just the velocity map we can tell that the angle is larger than 0°, - because we pick up a difference in velocity, and smaller than 90°, -because the North is blue shifted, and because we spatially can separate the blue shifted material from the red shifted. We try to do this in two different ways, which are built on different assumptions.
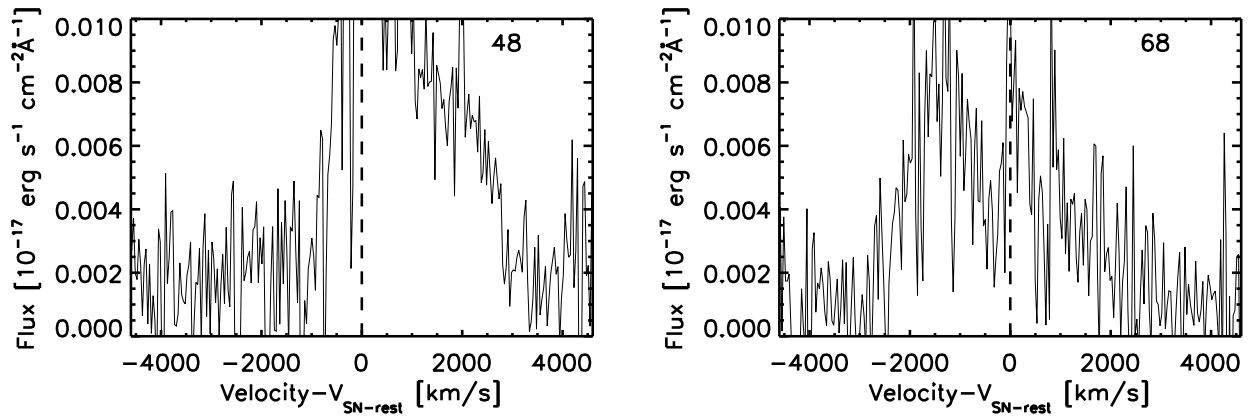
Figure 6.13: The velocity distribution of the central [Fe II] 1.6435 μm emission for spaxel (70,48) and (70,68) respectively. Aperture radius=0.025".
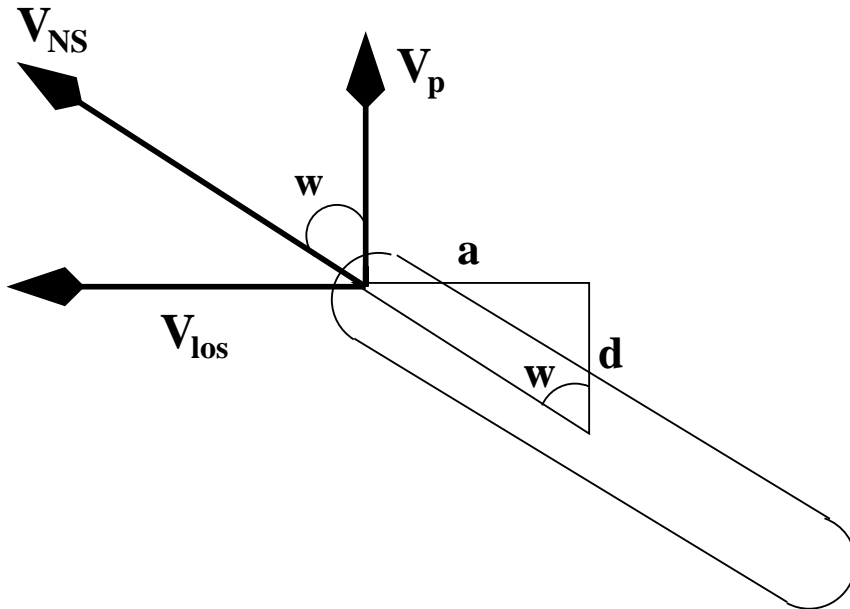

Figure 6.14: The North-South expansion velocity (V_{NS}) decomposed and drawn on top of some illustrations of dimensions in the ejecta. V_{los} is the line of sight velocity and V_p is the perpendicular velocity. w is the sought inclination angle, and d the projected distance.

Method 1: using the maximum velocity

We assume that the ejecta has been freely and symmetrically expanding along the North South axis for t=18 years. We would like to determine the inclination angle of the cigar-shape with respect to the plane of the sky along the North-South axis. Figure 6.14 shows a schematic drawing of the relation between the projected distance, d, the inclination angle, w, and the distance, a, the material has moved towards us in the time t=18 years.

Let v_{NS} be the de-projected expansion velocity of the ejecta in the North-South direction, which can be decomposed into a velocity in the line of sight v_{los} and one perpendicular to the line of sight v_p by: $v_{NS} = \sqrt{v_{los}^2 + v_p^2}$.

We use the spatial separation of V_{blue} and V_{red} and their values found previously from Figure 6.13, which gives us an average $v_{los} = 2750 \pm 180$ km s^{-1} for the travelled projected distance, d=10 px (~ 0.25"). We can find v_p by measuring how much the material has moved in the North-South direction and assuming that the material has moved with a constant velocity in the 18 years since the explosion (the data is from 2005). Using a distance to the system of 50 kpc, we find that the distance d is 0.0606 pc, which yields a perpendicular velocity of $v_p = d/t = 3300 \pm 660$ km s^{-1}, using an uncertainty for the spaxel position of 0.05" (2 pixels). The velocity in the plane spanned by the North-South axis and the line of sight is thus:

$$v_{NS} = \sqrt{v_{los}^2 + v_p^2} = 4300 \pm 1040 \quad \text{km s}^{-1}. \tag{6.2}$$

Which corresponds well with the velocity of the blast wave (3000-4000 km s^{-1}). The inclination of the expansion in this plane (edge on would be 90 degrees) is:

$$tan(w) = \frac{2750 \text{ km s}^{-1}}{3300 \text{ km s}^{-1}}, \qquad \text{and thus} \qquad w = 40.^\circ \pm 10^\circ \tag{6.3}$$

assuming independent and random errors. This places the outflow direction more or less in the plane of the ring.

Method 2: using the ejecta shape and spectra

We can calculate the inclination by assuming that the geometry/shape of the ejecta is an elongated ellipsoid where the two shorter axes (x and y) are the same in size. We then determine the inclination (in North-South direction) of the longer z axis using the spectra and the image of the ejecta. Figure 6.15 illustrates the technique, we see here that the inclination angle w can be described as:

$$cos(90^\circ - w) = \frac{d}{r} \iff sin(w) = \frac{d}{r} \tag{6.4}$$

Where r is the size of the x or y axis in the ellipsoid and can be measured as the width (in East-West) of the ejecta shape. d we can find from the spectra of the spaxels as half the distance between the two spaxels closest to each other (in the North-South direction) who have no red emission for the line and no blue emission for the line.

We measure r to be 16 ± 1px (the half of the full intensity profile (FWZI)). The Southern most spaxel with no red emission is 67 ± 1 px, and the Northern most spaxel with no blue emission
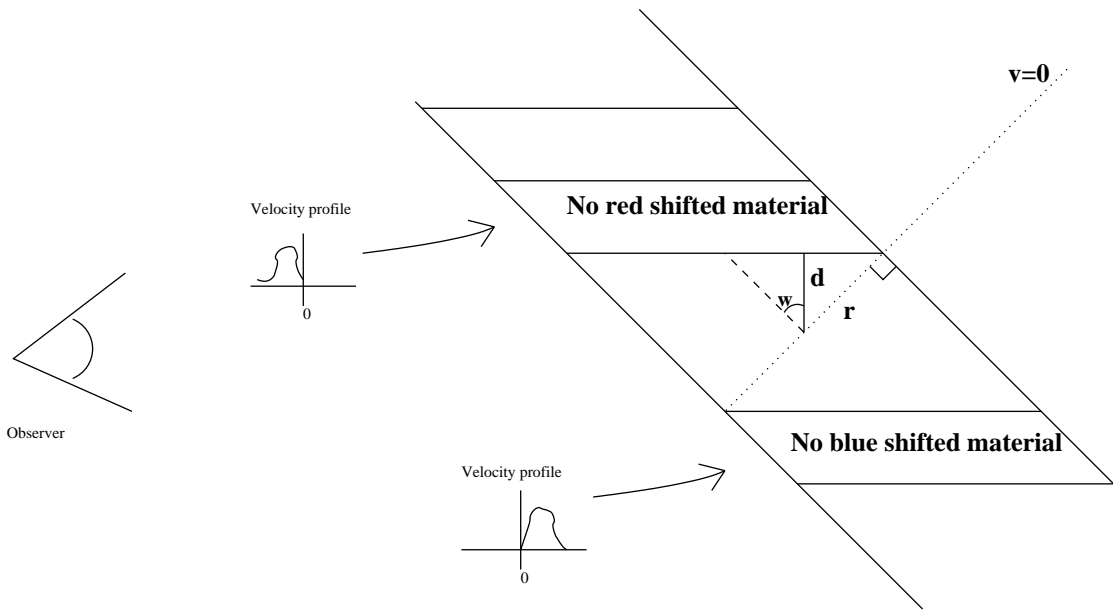
Figure 6.15: Illustration of a cigar-shaped ejecta with its velocity signatures.
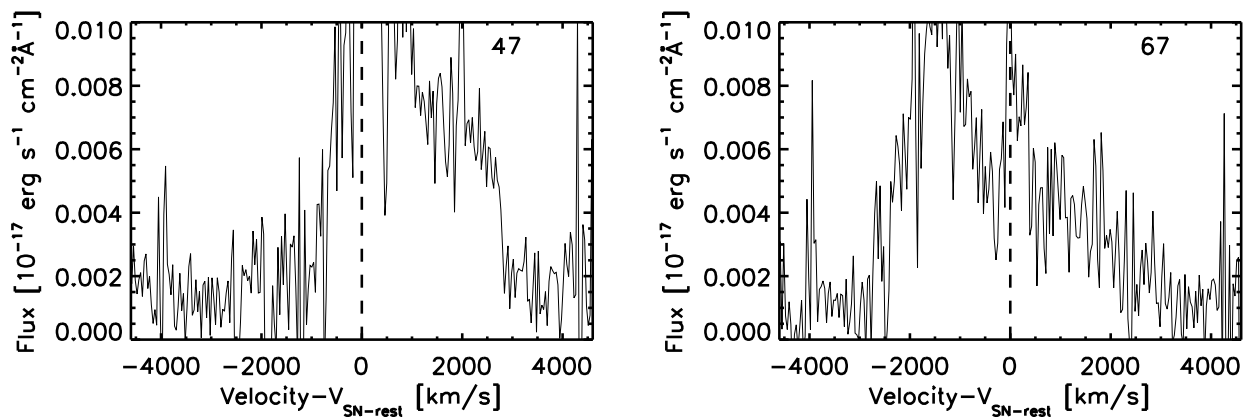

Figure 6.16: The velocity distribution of the central [Fe II] 1.6435 μm emission for spaxel (70,47) and (70,67) respectively.

is spaxel 47 ± 1 px (see Fig. 6.16). Thus d is (67px-47px)/2= 10 px ± 1.4 px. The inclination is thus:

$$sin(w) = \frac{10px}{16px} \iff w = 39° \mp_{10°}^{9°} \tag{6.5}$$

This method faces at least two major problems. One is that contamination from the seeing greatly influences the choice of the pixels in both directions, which most likely causes us to overestimate the distances. The other major problem is the assumption about the geometry, which we from imaging can see is not accurate.

6.3 Ejecta Summary

We found the position angle of the [Fe II] emission to be $17° ± 3°$, which confirms the PA found by Wang et al. (2002) from HST images of Fe I and Fe II from June 2000. We were the first to establish the inclination angle out of the plane of the sky for the ejecta, which we found to be $i = 40.° ± 10°$, and thus in the plane of the inner ring.

So far there has only been a few detailed studies of the late time ejecta of SN 1987A (Wang et al. 1996; Jansen & Jakobsen 2001; Wang et al. 2002). Wang et al. (1996) found that the measured sizes of the ejecta in the UV is two times as big as the size in the optical, also the line profiles are broader in the UV than in the optical. This was also seen by Jansen & Jakobsen (2001) who attributed this larger extend in the UV to scattering of optically thick transitions (predominately magnesium and iron) compared to the optically thin forbidden and semi-forbidden transitions that dominate the visible spectrum.

We also see the width of the forbidden [Fe II] 1.644 μm line, for which we see the ejecta the strongest, to be smaller than the width of the He I 2.058 μm line. This means that 6 years later the forbidden lines are still narrower than the optically thick lines, such as the He I line.

Wang et al. (2002) combined all previous observations of the asymmetries in the ejecta of SN 1987A and found that they all share the same axis of symmetry. This symmetry axis is the 15° position angle and 45° into the plane of the sky, i.e. along the symmetry axis of the rings (see Fig. 6.10). They also observed, with HST in 1999, a total of 7 spectra each from a vertical slice of 0.1". They saw the majority of the ejecta being red-shifted except for the middle part, which was blue shifted. The Northern most bin was red shifted 1270 km s^{-1} less than the Southern most bin, but because the velocity gradient was not monotonic, the kinematics were not securely established. Furthermore, they did not have the spatial resolution necessary to distinguish between the emission coming from the ejecta and the reverse shock closer to the ring. However, ignoring the middle bin in their observations one would get a velocity gradient similar to the one we found.

The FWHM map (Fig. 6.8) supports a bipolar outflow, in that the FWHM is larger in the central region, where both red and blue shifted material contribute to the emission. Further away from the centre the FWHM drops, most notably in the North and South direction. Our observations of the ejecta kinematics is consistent with a bipolar ejecta outflow directed along an axis 15° in the plane of the sky and 40° out of the plane of the sky.

This leaves three possible scenarios: (i) Let the iron be ionised by the radioactive decay of titanium and thus outline the titanium. The iron emission could then outline the inner boundary of a very thick disk that is hollow in the middle and situated in the ring. We would then observe the iron to be red shifted in the South and blue shifted in the North. We should then see a double peaked line profile of the iron. To test this hypothesis modelling of the spectrum is needed. But the scenario is tempting, because the rotation axis of the progenitor star would then be aligned with the symmetry axis of the triple ring system. (ii) An other explanation could be that the explosion was so asymmetric that it did not follow the rotation axis of the progenitor star, which was aligned with that of the triple ring system. (iii) A third scenario is that the rotation axis of the progenitor was not aligned with axis of symmetry for the triple rings. However that contradicts the merger model Podsiadlowski et al. (1990) has proposed for the progenitor and the formation of the rings.

Chapter 7

Summary

I have studied the spectacular supernova 1987A at a stage in its evolution into a supernova remnant, where the ejecta plunges into the inner circumstellar ring. I presented two epochs 17 and 18 years after explosion of data both observed with an integral field spectrograph operating in the IR (SINFONI) mounted on the Very Large Telescope (VLT, in Chile). This makes these the first IR observations to be published since Fassia et al. (2002) published spectra from the supernova at the age of 9 years.

The extended nature of the ring (and by now the ejecta) limits slit spectroscopy to individual regions of the ring. With an integral field unit, it is has been possible for me to measure the ring and the supernova ejecta without losses, to reconstruct the ring emission in individual lines, and to clearly separate the ejecta from the ring.

These observations are the first of their kind for SN 1987A and I have with it established the kinematics for the ring and ejecta separately for the first time. New instrument and new observational techniques have paid off scientifically for SN 1987A.

7.1   The Ring

The supernova shock interaction with the inner circumstellar ring around SN 1987A is in full swing. These integral-field observations have revealed the extent of individual emission lines around the ring. The ring has in the optical been lit up in spots remarkably evenly spaced (Michael et al. 2000; Lawrence et al. 2000; Plait et al. 1995). In the infrared there is emission from the entire ring, but only a few hot spots can be individually identified by their excess in emission as compared to the ring. The position of these hot spots are not evenly spaced like the hot spots in the optical. This could indicate that the infrared emission is delayed in time with respect to the optical emission, since the shocked gas material needs to cool down before it can emit in the infrared.

I have with SINFONI for the first time established the kinematics for the ring, and with that been able to determine parameters for the ring geometry. The kinematics for the ring are consistent with a circular ring (as opposed to an ellipse), and by identifying the nodal points for the ring's inclination, I found the major axis to be at position angle $81° \pm 7°$ as measured from North through East. This result agrees well with that found by Sugerman et al. (2005) ($81° \pm 0.°8$) using

imaging of light echoes and modelling of the entire circumstellar structure around SN 1987A. The recession velocity found at the nodal points, 280±7 km s^{-1} also agrees with other results of 286.5 km s^{-1} for the systemic velocity of the ring around SN 1987A (Gröningsson et al. 2007; Meaburn et al. 1995; Crotts et al. 1995; Cumming & Meikle 1993).

Using the kinematics I have made a radial velocity curve for the ring, which shows significant differences of the velocities around the ring, with the eastern part showing larger velocities than the western segment. This correlates well with the increase in surface brightness seen in both the radio observations (Manchester et al. 2002), Chandra observations (Park et al. 2006) and the appearance of Spot 1 in the East (Michael et al. 2002; Pun et al. 2002; Sugerman et al. 2002). The differences could be due to one or several of the following causes (i) differences in the densities of the material in the ring slowing the shock front down, (ii) differences in the ejecta outflow (suggested by Lawrence et al. 2000, as the cause for spot 1), (iii) by the supernova not being situated in the centre of the ring (Sugerman et al. 2002; Plait et al. 1995, found that the ejecta was not situated in the centre of the tilted ring).

I have de-projected the radial velocities into an outward velocity of the shocked gas component in the ring for different position angles. From this I found the shocked gas at PA=307° ± 9° having a larger expansion velocity than the immediate gas around it. I was able to identify the position with larger expansion velocity with a vacant section of the circumstellar ring in the HST images. This suggests that the vacant region has a lower density than the rest of the ring, since the forward shock, and ultimately the shocked gas component then would be decelerated less by the ring. This might reveal the structure of the ring to be not so much a ring, but rather a circular collection of clumps. Whether the ring is a ring or clumps will become obvious the coming years, as the hot spots are expected to merge if it is a ring.
From the velocity shift of the lines I find an average velocity of $\sim 100 - 200$ km s^{-1} for the bulk of the H and He emitting shocked gas. This is just the average velocity, and considerably higher velocity shocks are present, as is directly evidenced by UVES observations (Gröningsson et al. 2006, 2007).

7.2   The Ejecta

The emission from the supernova itself has faded continuously. Today it is mostly the radioactive decay of ^{44}Ti and reverse shock interaction, which powers the emission from the ejecta.
With the integral-field spectrograph I have been able to spatially isolate the ejecta emission from the ring emission, and I detect several emission lines with widths ranging from 1200-7000 km s^{-1}. This is consistent with the radioactively and reverse shock heated ejecta seen in Hα, Ca II and Mg I (Smith et al. 2005; Gröningsson et al. 2007).
We also see that the width of the forbidden [Fe II] 1.644 μm line, the strongest line observed for the ejecta, is smaller than the width of the He I 2.058 μm line, which is consistent with observations made by Wang et al. (1996) who found the forbidden lines were narrower than the optically thick lines. They also saw a difference in the spatial extend of the emission, where the ejecta was more elongated in the forbidden lines and more spherical in the optically thick lines. I have with the shape of the [Fe II] 1.644 μm line emission seen, 6 years later, that this is still

the case. The shape of the ejecta in the He I emission line was difficult to ascertain, because of its faintness.

After 18 years the ejecta have expanded enough so that they can be observed spatially resolved for the first time. This allowed me to make the first kinematic measurement of the resolved ejecta.

I have from the [Fe II] 1.644 μm line established the kinematics of the ejecta, and found that the North part of the ejecta is blue shifted and the South part red shifted, the same patterns as also observed for the ring. This surprising result is opposite to what one would expect. The symmetry axis for the triple ring system is perpendicular to the inner ring and should be the same as the rotation axis for the progenitor star (as modelled by Podsiadlowski et al. 1990). For SN 1987A it has been expected that any bipolar outflow should be along the rotation axis of the progenitor, and thus perpendicular to the inner ring (see Fig. 6.10 for an illustration of the expected outflow direction). This would cause the Southern part of the ejecta emission to be blue shifted and the Northern part red shifted, -opposite to what we find.

The spatial distribution of the FWHM for the [Fe II] 1.644 μm line indicates that the emitting material is from a bipolar outflow, in that the FWHM is larger in the central region, where both red and blue shifted material contribute to the emission. Further away from the centre the FWHM drops, most notably in the North and South direction.

This leaves three possible scenarios (as explained in chapter 6.3 in more detail): (i) We are seeing the inner boundary of a very thick disk, which is hollow in the middle and situated in the ring, and the rotation axis of the progenitor star was aligned with the symmetry axis of the triple ring system. (ii) The explosion was so asymmetric that it did not follow the rotation axis of the progenitor star, which was aligned with that of the triple ring system. (iii) A third scenario is that the rotation axis of the progenitor was not aligned with axis of symmetry for the triple rings. However that contradicts the merger model Podsiadlowski et al. (1990) has proposed for the progenitor and the formation of the rings.

From the emission structure of the ejecta I find the position angle of the elongated ejecta to be $17° \pm 3°$ which corresponds well with the $14° \pm 5°$ found by Wang et al. (2002). I am the first to estimate the inclination angle out of the plane of the sky for the ejecta, which I found to be $i = 40.° \pm 10°$.

7.3 The Future

Monitoring the transformation of SN 1987A into a supernova remnant is a unique opportunity. It is the only such object in which we can directly observe this event while simultaneously resolving the interaction region. The structure of the circumstellar ring has been a puzzle since its discovery when it was ionised by the supernova soft X-ray flash. For a complete picture we need to monitor this transition at all wavelengths.

Recently a nearby twin of SN 1987A's nebula was discovered around a luminous blue variable (LBV) by Smith (2007), who suggests that the bipolar structure of the nebula originated in an LBV eruption. If the progenitor of SN 1987A suffered an LBV-like eruption and thereby

created the rings, then there is no need for a merger scenario to explain the rings in the nebula. The circumstellar rings of SN 1987A represent only the inner skin of a much greater mass of circumstellar matter, so far only inferred from light echoes of the supernova explosion. The clues to the origin of the circumstellar ring system lie in the distribution and velocity of this matter. The shocks in the hot spots are producing ionising radiation, of which roughly half will propagate ahead of the shock and ionise as of yet not visible material, and we will observe it as a brightening of the narrow emission lines in the vicinity of the hot spots. When the blast wave from the supernova has fully overtaken the inner ring, we will have a chance at seeing more of the circumstellar material and from that deduce its origin. In this way SN 1987A will be illuminating its own past.

Since SN 1987A is the only young SN that can be spatially resolved it can be used to establish a testbed for supernovae with circumstellar interaction. When progenitor stars loose mass in strong stellar winds they leave imprints on the supernova environment. The evolutionary history of a progenitor star can therefore be pieced together by observing late phases of supernovae, where the ejected material is moving through the mass lost by the progenitor. With the integral field observations the geometric effects in the spectral features can be disentangled from physical ones caused by the shock physics in the circumstellar interaction. This gives us an advantage, when we observe supernova further away, where we cannot spatially resolve the circumstellar matter.

With the 3D spectroscopy we are finally in a position, where we can use the insights gained from SN 1987A as a stepping-stone to understanding the behaviour of this class of objects in general.

7.4 The Uniqueness of this Work

I was among the first scientists to obtain raw data from the newly commissioned instrument SINFONI. They posed quite a challenge as the pipeline was far from fully functional. During my PhD I have provided feedback to the pipeline developer (Andrea Modigliani, ESO) and thus helped in improving it through the different versions. Furthermore I was the first to analyse 3D spectroscopy for an emission line object, which meant I had to develop a methodology for the analysis (see chapter 2). This was made more complicated by the fact that SN 1987A has many different emission sites governed by different emission mechanisms (see chapter 1). I am grateful to ESO and my supervisor there, Bruno Leibundgut, that I was given the opportunity to do pioneer work with such an interesting new instrument and on such a fascinating object.

Bibliography

Arnett, W. D., Bahcall, J. N., Kirshner, R. P., & Woosley, S. E. 1989, ARA& A, 27, 629

Bouchet, P., De Buizer, J. M., Suntzeff, N. B., et al. 2004, ApJ, 611, 394

Bouchet, P., Dwek, E., Danziger, J., et al. 2006, ApJ, 650, 212

Burrows, C. J., Krist, J., Hester, J. J., et al. 1995, ApJ, 452, 680

Cappellari, M. & Copin, Y. 2003, MNRAS, 342, 345

Cardelli, J. A., Clayton, G. C., & Mathis, J. S. 1989, ApJ, 345, 245

Chevalier, R. A. 1982, ApJ, 258, 790

Cohen, M., Wheaton, W. A., & Megeath, S. T. 2003, AJ, 126, 1090

Crotts, A. P. S., Kunkel, W. E., & Heathcote, S. R. 1995, ApJ, 438, 724

Cumming, R. J. & Meikle, W. P. S. 1993, MNRAS, 262, 689

Davies, R. 2007, ArXiv Astrophysics e-prints

Fassia, A., Meikle, W. P. S., & Spyromilio, J. 2002, MNRAS, 332, 296

Fitzpatrick, E. L. & Walborn, N. R. 1990, AJ, 99, 1483

Fransson, C., Gilmozzi, R., Groeningsson, P., et al. 2007, The Messenger, 127, 44

Fransson, C. & Kozma, C. 2002, New Astronomy Review, 46, 487

Fransson, C. & Lundqvist, P. 1989, ApJ, 341, L59

Gillessen, S., Davies, R., Kissler-Patig, M., et al. 2005, The Messenger, 120, 26

Glass, I. S. 1999, Cambridge University Press, 1, 200

Graves, G. J. M., Challis, P. M., Chevalier, R. A., et al. 2005, ApJ, 629, 944

Gröningsson, P., Fransson, C., Lundqvist, P., et al. 2007, ArXiv Astrophysics e-prints

Gröningsson, P., Fransson, C., Lundqvist, P., et al. 2006, A& A, 456, 581

Haberl, F., Geppert, U., Aschenbach, B., & Hasinger, G. 2006, A& A, 460, 811

Hanuschik, R. W. 1988, Proceedings of the Astronomical Society of Australia, 7, 446

Hanuschik, R. W. & Dachs, J. 1987, A& A, 182, L29+

Heng, K. 2007, ArXiv e-prints, 704

Heng, K., McCray, R., Zhekov, S. A., et al. 2006, ApJ, 644, 959

Heng, K., van Adelsberg, M., McCray, R., & Raymond, J. C. 2007, ArXiv e-prints, 705

Hillebrandt, W., Hoflich, P., Kafka, P., et al. 1987, A& A, 177, L41+

Jansen, R. A. & Jakobsen, P. 2001, A& A, 370, 1056

Karovska, M., Nisenson, P., Noyes, R., et al. 1987, IAU, 4382, 2

Kissler-Patig, M. & Szeifert, T. 2005, in Very Large Telescope, SINFONI, User Manual, VLT-MAN-ESO-14700-3517 Issue 1.3

Kjær, K., Gröningsson, P., Kotak, R., Fransson, C., & Leibundgut, B. 2007a, in American Institute of Physics Conference Series, Vol. 924, American Institute of Physics Conference Series, 366–372

Kjær, K., Leibundgut, B., Fransson, C., et al. 2007b, A& A, 471, 617

Larson, H. P., Drapatz, S., Mumma, M. J., & Weaver, H. A. 1987, in ESO Workshop on SN 1987 A, ed. I. J. Danziger, 147–151

Lawrence, S. S., Sugerman, B. E., Bouchet, P., et al. 2000, ApJ, 537, L123

Leibundgut, B. & Suntzeff, N. B. 2003, in LNP Vol. 598: Supernovae and Gamma-Ray Bursters, ed. K. Weiler, 77

Loredo, T. J. & Lamb, D. Q. 2002, Physical Review D, 65, 063002

Lucy, L. B., Danziger, I. J., Gouiffes, C., & Bouchet, P. 1991, in Supernovae. The Tenth Santa Cruz Workshop in Astronomy and Astrophysics, held July 9-21, 1989, Lick Observatory. Publisher, Springer-Verlag, New York, 1991., ed. S. E. Woosley, 82

Lundqvist, P. & Fransson, C. 1991, ApJ, 380, 575

Lundqvist, P. & Fransson, C. 1996, ApJ, 464, 924

Manchester, R. N., Gaensler, B. M., Wheaton, V. C., et al. 2002, Publications of the Astronomical Society of Australia, 19, 207

Marcher, S. J., Meikle, W. P. S., Morgan, B. L., & Kepler, S. O. 1987, IAU, 4391, 1

Martin, W. C., Reader, J., & Wiese, W. L. 2003, Atomic Data for X-Ray Astronomy, 25th meeting of the IAU, Joint Discussion 17, 22 July 2003, Sydney, Australia, 17

McCray, R. 1993, ARA& A, 31, 175

Meaburn, J., Bryce, M., & Holloway, A. J. 1995, A& A, 299, L1

Meikle, W. P. S., Spyromilio, J., Allen, D. A., Varani, G.-F., & Cumming, R. J. 1993, MNRAS, 261, 535

Michael, E., McCray, R., Pun, C. S. J., et al. 1998, ApJ, 509, L117

Michael, E., McCray, R., Pun, C. S. J., et al. 2000, ApJ, 542, L53

Michael, E., Zhekov, S., McCray, R., et al. 2002, ApJ, 574, 166

Modigliani, A., Hummel, W., Abuter, R., et al. 2007, ArXiv Astrophysics e-prints

Morris, T. & Podsiadlowski, P. 2007, Science, 315, 1103

Nussbaumer, H. & Storey, P. J. 1988, A& A, 193, 327

Panagia, N., Gilmozzi, R., Macchetto, F., Adorf, H.-M., & Kirshner, R. P. 1991, ApJ, 380, L23

Park, S., Burrows, D. N., Garmire, G. P., et al. 2007, ArXiv e-prints, 704

Park, S., Zhekov, S. A., Burrows, D. N., et al. 2006, ApJ, 646, 1001

Park, S., Zhekov, S. A., Burrows, D. N., & McCray, R. 2005, ApJ, 634, L73

Plait, P. C., Lundqvist, P., Chevalier, R. A., & Kirshner, R. P. 1995, ApJ, 439, 730

Podsiadlowski, P., Joss, P. C., & Rappaport, S. 1990, A& A, 227, L9

Pun, C. S. J., Michael, E., Zhekov, S. A., et al. 2002, ApJ, 572, 906

Rousselot, P., Lidman, C., Cuby, J.-G., Moreels, G., & Monnet, G. 2000, A& A, 354, 1134

Schreiber, J., Thatte, N., Eisenhauer, F., et al. 2004, in ASP Conf. Ser. 314: Astronomical Data Analysis Software and Systems (ADASS) XIII, ed. F. Ochsenbein, M. G. Allen, & D. Egret, 380

Smith, N. 2007, AJ, 133, 1034

Smith, N., Zhekov, S. A., Heng, K., et al. 2005, ApJ, 635, L41

Spyromilio, J. & Graham, J. R. 1992, MNRAS, 255, 671

Staveley-Smith, L., Kim, S., Calabretta, M. R., Haynes, R. F., & Kesteven, M. J. 2003, MNRAS, 339, 87

Sugerman, B. E. K., Crotts, A. P. S., Kunkel, W. E., Heathcote, S. R., & Lawrence, S. S. 2005, ApJS, 159, 60

Sugerman, B. E. K., Lawrence, S. S., Crotts, A. P. S., Bouchet, P., & Heathcote, S. R. 2002, ApJ, 572, 209

Trundle, C., Dufton, P. L., Hunter, I., et al. 2007, A& A, 471, 625

Walborn, N. R., Phillips, M. M., Walker, A. R., & Elias, J. H. 1993, PASP, 105, 1240

Wampler, E. J. & Richichi, A. 1989, A& A, 217, 31

Wampler, E. J., Wang, L., Baade, D., et al. 1990, ApJ, 362, L13

Wang, L., Wheeler, J. C., Höflich, P., et al. 2002, ApJ, 579, 671

Wang, L., Wheeler, J. C., Kirshner, R. P., et al. 1996, ApJ, 466, 998

Zhekov, S. A., McCray, R., Borkowski, K. J., Burrows, D. N., & Park, S. 2005, ApJ, 628, L127

Zhekov, S. A., McCray, R., Borkowski, K. J., Burrows, D. N., & Park, S. 2006, ApJ, 645, 293

Appendix A

Line Identification

There are many emission lines from SN 1987A which come from the same element. We have a large number of forbidden [Fe II] lines and many of the lines in the Brackett series (hydrogen). An emission line photon is emitted when an electron in a higher energy state makes a transition to a lower energy state. The wavelength of the emitted photon reveals the states the electron 'jumped' between. For iron there are many lower states the electron can make its transition to, and this gives us an extra tool in verifying the line identification for the emission lines. The probability for an electron to make a certain transition is given by quantum mechanics, and when we have two or more emission lines from electrons originating in the same upper level, the ratios of the flux for the lines are determined theoretically.

Figure A.1 shows the [Fe II] lines in the J and H band, and the states the electron jumps between. A forbidden line is emitted by atoms undergoing energy transitions not normally allowed by the selection rules of quantum mechanics. However, there is a non-zero probability of their spontaneous occurrence, should an atom or molecule be raised to an excited state. The transition probability is extremely low, and in normal (i.e. dense environments) atoms are collisionally de-excited before the forbidden line emission occur. In low-density gasses atomic collisions are unlikely, and forbidden line transitions occur and may even account for a significant percentage of the photons emitted.

The extra check for the line identification for the Br and [Fe II] lines was made using that the ratio of flux between some of the lines are fixed by nature. Tables A.1-A.4 lists the H and [Fe II] lines with their transition probability from the NIST line catalogue (Martin et al. 2003), and the observed intensities and their ratios.

An Example:

Here is an example for the two [Fe II] lines at 1.257 μm and 1.321 μm. The flux of the 1.257 μm line can be calculated as:

$$F_{1.257} = N_{4_{D_{7/2}}} A_{4_{D_{7/2}} - 6_{D_{9/2}}} h\nu_{1.257}, \tag{A.1}$$

where $N_{4_{D_{7/2}}}$ is the number of electrons in the $4D_{7/2}$ state and $A_{4_{D_{7/2}} - 6_{D_{9/2}}}$ is the Einstein probability for the transition, h is the Planck's constant, ν is the frequency, and F is the flux for the line. Similarly the flux of the 1.321 μm line can be calculated as:

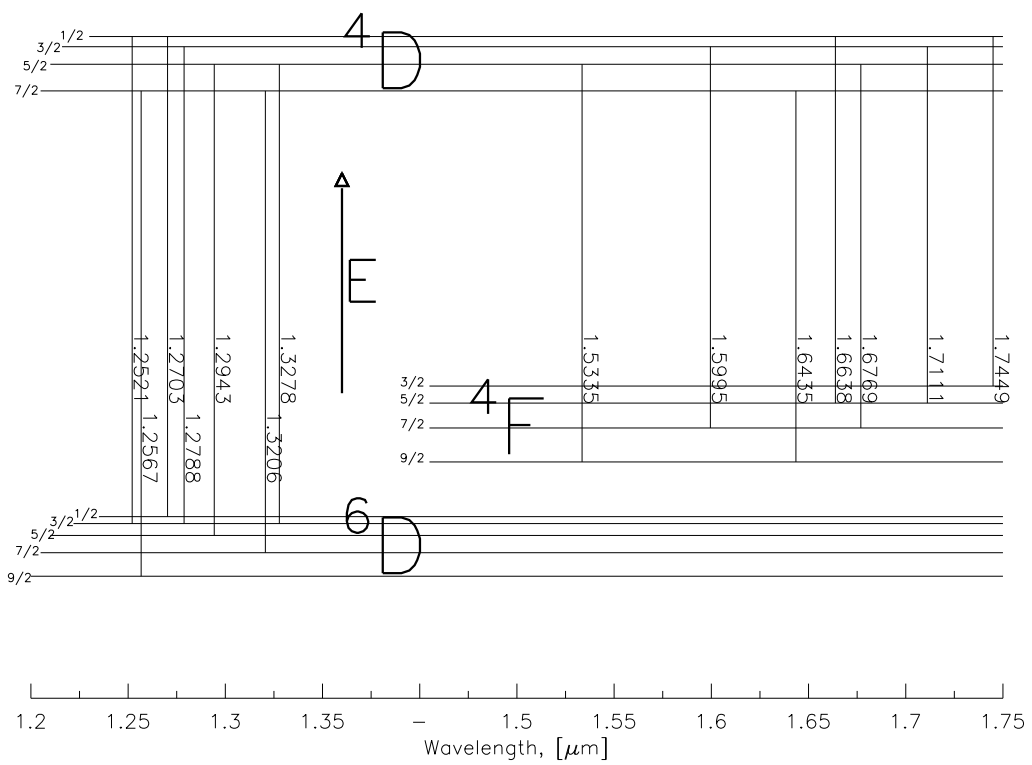$$F_{1.321} = N_{4_{D_{7/2}}} A_{4_{D_{7/2}} - 4_{F_{9/2}}} h\nu_{1.321} \tag{A.2}$$

Figure A.1: The Grotrian diagram of the [Fe II] lines in the J and H band, note that the x-axis is not continuos in its numbering.

The flux ratio between the two lines is then:

$$F_{1.257}/F_{1.321} = \frac{A_{^4D_{7/5}-^6D_{9/2}}\nu_{1.257}}{A_{^4D_{7/5}-^4F_{9/2}}\nu_{1.321}} \tag{A.3}$$

which then only depends on known numbers. If the observed ratio of the fluxes does not correspond to the value calculated using this approach, then (i) the line is a blend between the line and another (un)known line (ii) there is extinction affecting only one of the emission lines (this is unlikely, since the distance in wavelength between the lines are so small, that if extinction (dust, electrons etc.) are affecting one line they would also affect the other line).

This way we have confirmed the identifications of the [Fe II] and Brackett lines. When the calculated ratio did not agree with the observed ratio, then it is noted in the line tables in Chapter 4.

Table A.1: The [Fe II] lines with the transition identification.

λ_{peak}	Velocity	σ_{deconv}	Intensity	Identification	λ_{rest}	A
μm	km/s	km/s	10^{-16}erg/s/cm^2		μm	s^{-1}
1.25385	410	404	23	[Fe II] a^{6}D$_{3/2}$-a^{4}D$_{1/2}$	1.2521381	6.48e-4
1.25787	279	132	71	† [Fe II] a^{6}D$_{9/2}$-a^{4}D$_{7/2}$	1.2567	4.83e-3
1.27169	317	182	9	[Fe II] a^{6}D$_{1/2}$-a^{4}D$_{1/2}$	1.2703465	4.0e-3
1.27983	247	266	39	†[Fe II] a^{6}D$_{3/2}$-a^{4}D$_{3/2}$	1.2787757	2.25e-3
1.29562	313	117	17	†[Fe II] a^{6}D$_{5/2}$-a^{4}D$_{5/2}$	1.2942692	1.94e-3
1.32178	279	71	18	†[Fe II] a^{6}D$_{7/2}$-a^{4}D$_{7/2}$	1.3205539	1.33e-3
1.32901	228	304	12	[Fe II] a^{6}D$_{3/2}$-a^{4}D$_{5/2}$	1.3277772	1.4e-3
1.53494	287	233	19	†[$FeII$] a^{4}F$_{9/5}$-a^{4}D$_{5/2}$	1.5334713	2.44e-3
1.60098	283	202	11	†[Fe II] a^{4}F$_{7/2}$-a^{4}D$_{3/2}$	1.5994716	3.28e-3
1.67851	292	210	12	†[Fe II] a^{4}F$_{7/2}$-a^{4}D$_{5/2}$	1.6768762	1.94e-3
1.64518	298	139	51	†[Fe II] a^{4}F$_{9/2}$-a^{4}D$_{7/2}$	1.6435491	4.65e-3
1.66534	284	212	6	†[Fe II] a^{4}F$_{5/2}$-a^{4}D$_{1/2}$	1.6637663	3.73e-3
1.71289	309	243	3	†[Fe II] a^{4}F$_{5/2}$-a^{4}D$_{3/2}$	1.7111275	9.20e-4
1.74661	288	311	6	†[Fe II] a^{4}F$_{3/2}$-a^{4}D$_{1/2}$	1.7449352	1.95e-3
2.00855	277	227	5	†[Fe II] a^{4}P$_{1/2}$-a^{2}P$_{1/2}$	2.006696	8.1e-2
2.01696	274	318	8	[Fe II] a^{2}G$_{9/2}$-a^{2}H$_{1/2}$	2.01512	X
2.04779	261	283	8	†[Fe II] a^{4}P$_{5/2}$-a^{2}P$_{3/2}$	2.046007	6.3e-2
2.13462	260	256	3	†[Fe II] a^{4}P$_{3/2}$-a^{2}P$_{3/2}$	2.132769	3.2e-2
2.22593	292	231	5	[Fe II] a^{2}G$_{9/2}$-a^{2}H$_{11/2}$	2.22376	X
2.24580	288	529	3	†[Fe II] a^{4}P$_{1/2}$-a^{2}P$_{3/2}$	2.243643	1.4e-02

Table A.2: The [Fe II] line strength ratios and theoretical ratio (based on Einstein coefficients). The 'Method' refers to if the transitions compared are from one level to several levels, or several levels populating the same level (this is assuming that the lines are optically thin).

Line ratio λ_k/λ_j	Flux ratio F_k/F_j	Theory $\lambda_j A_k/(A_j \lambda_k)$	Velocities km/s	σ's km/s	Method	X^2
1.644/1.257	0.7 ±0.1	0.7	298/279	139/132	1 ->3	0
1.257/1.3206	3.9 ±0.6	3.8	279/279	132/71	1 ->3	0.003
1.644/1.3206	2.6 ±0.5	2.8	298/279	139/71	1 ->3	0.01
1.294/1.533	0.89 ±0.1	0.94	313/287	117/233	1 ->4	0.003
1.294/1.677	1.4 ±0.2	1.3	313/292	117/210	1 ->4	0.008
1.533/1.677	1.6 ±0.2	1.4	287/292	233/210	1 ->4	0.03
1.294/1.328	1.4 ±0.1	1.4	313/228	117/304	1 ->4	0
1.533/1.328	1.6 ±0.1	1.5	287/228	233/304	1 ->4	0.01
1.677/1.328	1.0 ±0.1	1.1	292/228	210/304	1 ->4	0.01
1.599/1.711	3.7 ±0.5	3.8	283/309	202/243	1 ->3	0.03
1.711/1.278	0.08 ±0.01	0.3	309/247	243/266	1 ->3	0.16
1.278/1.599	3.5 ±0.6	0.9	247/283	266/202	1 ->3	9
1.664/1.745	1.0 ±0.1	2.5	284/288	212/311	1 ->4	0.90
1.664/1.252	0.26 ±0.05	5.5	284/410	212/404	1 ->4	5
1.745/1.252	0.26 ±0.05	2.2	288/410	311/404	1 ->4	1.71
1.270/1.664	1.5 ±0.2	1.4	317/284	182/212	1 ->4	0.007
1.270/1.252	0.39 ±0.1	6.1	317/410	182/404	1 ->4	5.3
1.745/1.270	0.67 ±0.1	0.35	288/317	311/182	1 ->4	0.29
2.046/2.133	2.7 ±0.3	2.1	261/260	283/256	1 ->3	0.17
2.046/2.244	2.0 ±0.3	4.9	261/288	283/529	1 ->3	1.71
2.244/2.133	1.33 ±0.1	0.42	288/260	529/256	1 ->3	1.97
1.599/1.6769	0.9 ±0.1	1.8	283/292	202/210	2 -> 1	0.45
1.664/1.711	2.0±0.3	5.3	284/309	212/243	2 ->1	2.05
2.007/2.244	1.67 ±0.1	6.5	274/277	529/227	2 ->1	3.6

X^2 is calculated as (Theory-Intensity)^2/Theory. $X^2 \leq 1$ is the limit for a good agreement between the observed ratio and the calculated.

Table A.3: H lines and their transition possibility.

λ_{peak}	Velocity	σ	Intensity	Identification	λ_{rest}	A
μm	km/s	km/s	10^{-16}erg/s/cm^2		μm	s^{-1}
1.49489	224	197	1	*HI* Br26	1.4937727	3.12E+02
1.49825	303	304	2	*HI* Br25	1.4967335	3.81E+02
1.50986	315	259	5	*HI* Br22	1.5082775	7.26E+02
1.51461	255	237	3	*HI* Br21	1.5133221	9.19E+02
1.52037	234	257	3	*HI* Br20	1.5191844	1.18E+03
1.52705	199	319	4	*HI* Br19	1.5260538	1.53E+03
1.53494	149	233	19	*HI* Br18	1.5341790	2.01E+03
1.54512	239	253	5	*HI* Br17	1.5438920	2.69E+03
1.55707	275	251	5	*HI* Br16	1.5556448	3.67E+03
1.57142	259	288	7	*HI* Br15	1.5700662	5.10E+03
1.58947	267	265	10	†*HI* Br14	1.5880541	7.28E+03
1.61232	259	260	12	†*HI* Br13	1.6109313	1.07E+04
1.64236	300	195	12	†*HI* Br12	1.6407192	1.62E+04
1.68227	288	249	15	†*HI* Br11	1.6806520	2.55E+04
1.73769	256	294	21	†*HI* Br10	1.7362108	4.23E+04

Table A.4: The H line strength ratios and theoretical ratio (based on Einstein coefficients). I have assumed that all the Br lines can be compared with each other, since they come from the same level.

Line ratio	Intensity	Theory	Velocities	$\sigma's$	Note	X^2
λ_k/λ_j	F_k/F_j	$\lambda_j A_k/(A_j \lambda_k)$	km/s	km/s		
1.4938/1.5881	0.1 ±0.01	0.05	224/267	197/265		0.05
1.4967/1.5881	0.2 ±0.03	0.06	303/267	304/265		0.33
1.5083/1.5881	0.5 ±0.07	0.11	315/267	259/265		1.38
1.5133/1.5701	0.43 ±0.06	0.19	255/259	237/288		0.30
1.5192/1.5701	0.43 ±0.06	0.24	234/259	257/288		0.15
1.5261/1.5556	0.8 ±0.1	0.42	199/275	309/251		0.34
1.5342/1.5556	3.8 ±0.5	0.56	149/275	233/251		18.7
1.5439/1.5556	1.0 ±0.1	0.74	239/275	253/251		0.09
1.5556/1.5701	0.7 ±0.1	0.73	275/259	251/288		0.001
1.5701/1.5881	0.7 ±0.1	0.71	259/267	288/265		0.0001
1.5881/1.6807	0.67 ±0.1	0.30	267/288	265/249		0.46
1.6109/1.6407	1.0 ±0.1	0.67	259/300	260/195		0.16
1.6407/1.6807	0.8 ±0.1	0.65	300/288	195/249		0.03
1.7362/1.6807	1.4 ±0.2	1.6	256/288	294/249		0.03

X^2 is calculated as (Theory-Intensity)^2/Theory. X^2 ≤ 1 is the limit for a good agreement between the observed ratio and the calculated.

Acknowledgements